INTERFACIAL MECHANICS OF COMPOSITE-COATED SURGICAL NEEDLE IN TISSUES

A Dissertation
Submitted to
the Temple University Graduate Board

In Partial Fulfillment
of the Requirements for the Degree
DOCTOR OF PHILOSOPHY

---

by
Kavi I. Patel
December 2023

Examining Committee Members:

Dr. Parsaoran Hutapea, Advisory Chair, Department of Mechanical Engineering
Dr. Kurosh Darvish, Department of Mechanical Engineering
Dr. Fei Ren, Department of Mechanical Engineering
Dr. Chang Hee Won, External Member, Department of Electrical and Computer Engineering

ABSTRACT

This dissertation presents a study on enhancing surgical needles using a novel composite coating and investigates its impact on needle insertion mechanics. The aim is to create a less invasive needle insertion for a range of surgeries, including biopsy, thermal ablation, brachytherapy, and drug delivery. The composite coating, composed of Polydopamine (PDA), Polytetrafluoroethylene (PTFE), and Activated Carbon (C), overcomes the limitations of conventional needles by providing low friction and non-adhesive properties. As a result, it requires less insertion force and causes less tissue damage during needle insertion. In this research, the composite coating applied to a solid 18-gauge biopsy needle, equipped with a trocar tip, led to a notable reduction in insertion force, ranging from 30% to 49%. Furthermore, it exhibited an average improvement of 39% in minimizing tissue damage in bovine kidney tissues. This improved performance was observed with the composite coated needle as opposed to the bare one, attributable to a 56.9% reduction in the surface roughness RMS due to the coating.

In order to further investigate the mechanics behind the improved performance of the coated needle, an analytical insertion force model was developed, taking into account Coulomb friction and viscoelastic forces, as well as cutting force. The Coulomb friction and viscoelastic forces were modeled by adapting the Karnopp model, and the cutting force model was formulated based on the premise of cutting forces being linear with insertion velocity. The insertion force model was evaluated using experiments performed on bovine kidney tissue. Based on the model prediction, it was determined that the composite coating

performed better due to a reduction in Coulomb friction force. Compared to the experimental data, the accuracy range of the model was determined to be between 6.5% and 17.1% for bovine kidney. A limitation of the model is that it does not replicate forces for each individual layer of tissue, but instead provides an average force estimation for heterogeneous tissue. The model was constructed based on the assumption of needle insertion occurring without any needle deflection.

This dissertation provides critical insights into the field of surgical needles, demonstrating the considerable advantages of a novel composite coating. This innovation significantly lowers the insertion force and reduces tissue damage, opening the door to less invasive techniques for a myriad of surgical procedures. Despite the analytical model limitation, it is useful in surgeries preplanning, simulation, and robotic surgeries. Furthermore, the model has the potential to serve as a valuable tool for medical professionals, as it can furnish information on the location of the needle within the body from the predicted forces, in addition to the detection of variations in tissue stiffness. This information can assist in the accurate performance of medical procedures, leading to improved medical surgeries.

DEDICATION

I would like to express my deepest gratitude to my parents, siblings, and all my relatives for their unwavering support and love throughout all my endeavors, particularly my Ph.D. journey. I dedicate this work to them as a token of my appreciation for their constant encouragement, understanding, and guidance. Their support has been instrumental in enabling me to complete this thesis and reach this significant milestone in my academic journey.

ACKNOWLEDGMENTS

First and foremost, I would like to express my sincere gratitude to my advisor, Dr. Parsaoran Hutapea, for his support and guidance throughout my Ph.D. studies. I had the privilege of working in Dr. Hutapea dynamic research environment, where I was offered unique chances to investigate a broad range of scientific inquiries. I am immensely grateful for his belief and confidence in me with my research ideas and work. Guided by his expertise, I have gained comprehensive knowledge in research, encompassing everything from the initial idea formulation to the design of experiments and the crafting of professional documents. His mentorship has not only contributed significantly to my personal and professional growth but has also instilled in me the skills and knowledge necessary to be an effective mentor in my future endeavors. I am grateful for the valuable lessons and insights I have gained under his tutelage, which will absolutely serve me well in my future career pursuits. My gratitude also extends to the members of my dissertation committee, Dr. Kurosh Darvish, Dr. Fei Ren, and Dr. Chang Hee Won. Their thoughtful input and constructive feedback have been invaluable to my work. Their feedback and guidance were constructive in shaping my research and helping me to develop my ideas further.

I would like to express my gratitude to Dr. Fei Ren and his lab members for their collaboration and support, as well as for allowing me to work in their research lab. I would like to convey unique appreciation to both former and current lab-mates in the Composites Laboratory. Their steadfast encouragement and inspiration have been instrumental in my progress. I would like to thank the National Science Foundation (CMMI Award #1917711), Temple University Graduate School, and the College of Engineering for their financial support and the opportunity to perform my research.

Finally, I must thank my friends and family members for their ongoing backing and motivation. Above all, I owe a profound debt of gratitude to my immediate family. Their boundless affection and confidence in me have served as the fundamental catalysts in both my pursuit and successful conclusion of this significant endeavor.

TABLE OF CONTENTS

LIST OF TABLES

Table Page

LIST OF FIGURES

NOMENCLATURE

F_I	Insertion force
F_c	Cutting force
F_f	Total Friction force
F_T	Tissue force
F_N	Normal force
F_{St}	Static friction force
F_{CO}	Coulomb friction force
F_e	Elastic force
F_v	Viscous force
h	Needle insertion depth
V	Needle insertion relative velocity
C_c	Coefficients of the cutting force
b	Viscous Coefficient
k	Elastic Coefficient
F_{fr}	Dynamic Friction
V_P, V_N	Positive (Insertion) and Negative (Extraction) Velocity
b_P, b_N	Positive (Insertion) and Negative (Extraction) Viscous Coefficients
F_{COP}, F_{CON}	Positive (Insertion) and Negative (Extraction) Coulomb Friction Forces
x_P, x_N	Positive (Insertion) and Negative (Extraction) Tissue deflection Distance
k_P, k_N	Positive (Insertion) and Negative (Extraction) Elastic Coefficients

ABBREVIATIONS

PDA	Polydopamine
PTFE	Polytetrafluoroethylene
C	Activated Carbon
PVC	Polyvinyl Chloride
AFM	Atomic Force Microscope
DLC	Diamond-like Carbon
LFM	Lateral force microscopy
PETG	Polyethylene terephthalate glycol
H&E	Hematoxylin and Eosin
TFMG	Thin-film metallic glass
RMS	Root mean square

CHAPTER 1

INTRODUCTION

Percutaneous procedures such as spectroscopy, internal radiotherapy, chemotherapy thermal ablation, photodynamic therapy, biopsy and drug delivery utilize surgical needles for disease diagnoses and treatments [1-6]. It is widely recognized in surgical procedures that one of the most critical factors is the level of insertion force, which can result in tissue damage and tissue deflection, leading to a potential failure to hit the intended target. Numerous research studies have been conducted to develop innovative surgical needles that minimize tissue damage during medical procedures like biopsy and internal radiotherapy (brachytherapy) in various organs, including the prostate, liver, and kidney [1,2]. In brachytherapy, surgeons position radioactive elements either within or near the tumor growth, administering intensive radiation to the cancerous cells. This method focuses on the targeted area, which helps to reduce any unnecessary exposure to the adjacent healthy tissue. In this procedure, two types of needles are typically used: guide needles and treatment needles. The guide needles create a path for the treatment needles to follow. The treatment needles, which contain the radioactive sources, are then inserted into the tissue along the path created by the guide needles to deliver the radiation dose directly to the target area. The radioactive seeds can be temporarily or permanently implanted in the patient’s body, depending on the type and stage of cancer being treated. Brachytherapy is commonly used to treat prostate, breast, cervical, and skin cancer. Here, the success of this procedure heavily relies on the precise insertion of the needle and its ability to reach the intended target [2]. Achieving target accuracy during needle insertion is the foremost critical step for successful medical procedures involving needles. The level of accuracy depends on the force used for needle insertion, which, in turn, affects tissue damage, deformation, and deflection. Studies have shown that a reduction in the insertion force can significantly enhance the needle insertion procedure by mitigating discomfort and trauma, as well as reducing the healing time post-procedure [7,12]. The process of inserting the needle begins with puncturing the top surface layer (skin) of the tissue. After this initial puncture, the tip and shaft of the needle comes in contact with the tissue [9,12]. Throughout the insertion procedure, the needle tip undergoes a cutting force (F_c) [12], while the shaft experiences a friction force (F_f). The friction force is produced as a result of the tissue force (F_T) [4], which is the force exerted by the tissue on the needle. The force required for insertion, denoted as (F_I), is defined by adding together the friction force (F_f) and the cutting force (F_c). In contrast, the force needed for extraction relies solely on the friction force, as depicted in Figure 1.1. With an increase in the depth of insertion, the friction force tends to take on a more dominant role in comparison to the cutting force [13,14].

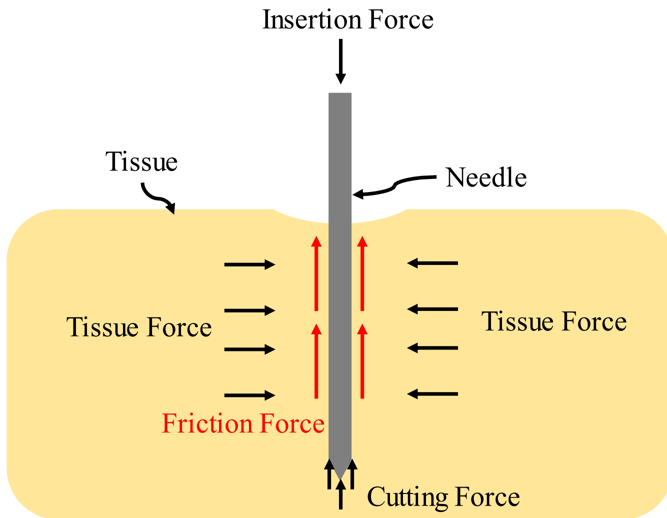

Figure 1.1 Interaction forces of needle moving inside the tissue: Friction force (F_f), Cutting force (F_c), and Tissue force (F_T).

1.1 Interaction Mechanism between Needle and Tissue

In any surgical procedure involving a needle, the needle-tissue interaction is divided into three phases [4]. Figure 1.2 illustrates the needle-tissue interaction forces in the bovine kidney, depicting three phases: insertion, relaxation, and extraction. The first insertion phase, where the needle first pushes into the tissue layer (creating a conical indentation, as shown in Figure 1.1) and then punctures the tissue. After that, the needle advances inside the tissue, with the tip and shaft in contact with the tissue. In the insertion phase, friction and cutting forces are exerted between the needle and tissue interface. The friction force is applied between the needle shaft and the tissue, while the cutting force is applied between the needle tip and the tissue. The second phase of the needle-tissue interaction is known as the relaxation phase, which takes place between the insertion and extraction phases. During this phase, the conical indentation returns to its original shape, and the direction of needle movement begins to change towards the opposite direction. This transitional process marks the shift from insertion to extraction. Finally, the third phase is the extraction phase, in which the needle is pulled out of the tissue. During the extraction phase, the needle tip does not contact the tissue; only the needle shaft stays in contact with the tissue. The extraction phase only involves the extraction force, including only the needle shaft friction force. The more complex the tissue structure, the greater the inaccuracies in reaching the target inside the tissue. When encountering tissues with higher stiffness, such as muscles and livers, the needle is more likely to undergo greater deflection, resulting in increased deformation of the tissue. This, in turn, could potentially lead to more tissue damage and inaccuracies in hitting the intended target [15,16].

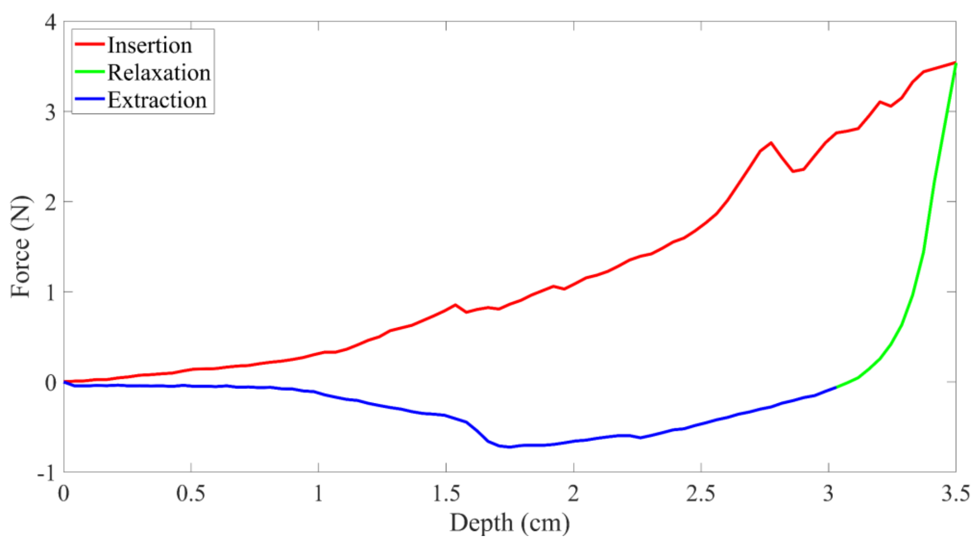

Figure 1.2 The phases of needle interaction forces with the bovine kidney tissue, i) Insertion (red), ii) Relaxation (green), and iii) Extraction (blue).

The needle-tissue interaction process highly depends on several factors, such as the needle design and material properties [16-24], insertion velocities [25,26], insertion techniques [12,27], and tissue properties [3,4]. Complicated medical surgeries such as biopsy and brachytherapy require the needle to be inserted deep inside the organ to reach the target, causing maximum force between the needle-tissue interface. As the needle is inserted deeply into the tissue, the shaft surface contact area increases, which also increases the friction force. Since the tip has a constant contact area with the tissue, the cutting force remains marginally constant throughout the insertion-extraction procedure. In the case of deep insertion within the organ, the friction force becomes the prevailing factor compared to the cutting force influencing the overall insertion force.

1.1.1 Design and Shape of Needles

Previous research has shown that needle insertion target accuracy is affected by the maximum insertion force, and reducing this force can also reduce tissue damage. Since the friction force is the dominant parameter for the insertion force, it is important to reduce the friction force. Figure 1.3 shows a few examples of needle designs with tip and shaft. Numerous studies have shown that the needle design and surface properties can significantly impact the insertion force. For example, Sahlabadi and Gidde et al. [9] studied honeybee-inspired needles where the needle shaft was designed based on the honeybee stinger. The honeybee stinger features barb carvings (Figure 1.3 (c)), which were transferred to their 3D-printed needle design and needle prototypes. This innovative design has shown a reduction in insertion force by 25% to 45% across various tissues.

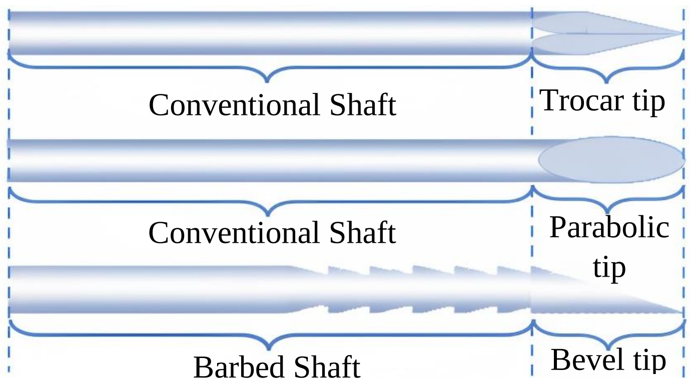

Figure 1.3 (a) Trocar tip needle **(b)** Parabolic tip needle **(c)** Bevel tip needle with barbed shaft.

The hypodermic needle, which was studied by Stellman [28], was shown to reduce the insertion force by 70%. In another study, Aneissha et al. [29] found that the needle tip geometry significantly affects cutting force. The parabolic tip needle (Figure 1.3 (b)), for instance, has less cutting force compared to the conventional bevel tip needle. However, it causes more needle deflection than the bevel-tip needle. Moreover, changes in needle diameter and shape can also result in a 25% reduction in insertion force, as demonstrated in Okamura et al. [30] research paper.

1.1.2 Mechanical Characteristics

The surface properties of a needle play a vital role in influencing its friction force during needle insertion inside a tissue. As the surface roughness decreases, the friction force also reduces, thereby reducing the insertion force and tissue damage. The coating on the needle surface can help to reduce surface friction and roughness, resulting in lower insertion and friction forces. Medical application coatings can be divided into two main categories: liquid lubricant coatings and dry lubricant coatings. Liquid lubricants, such as silicone oil [31,32], hydrogel [33], glycerin [34], hyaluronic acid [35], and mineral oil [36], are most commonly used in medical applications. These liquid lubricant coatings can enhance the properties of medical devices, especially surgical needles, by reducing surface friction. However, the reliability of liquid coatings is generally lower compared to that of dry lubricant coatings. Disadvantages of liquid lubricant coatings, when compared to dry lubricant coatings, include lower durability, the potential for contamination, inconsistency, and limited shelf life [31-35].

While dry lubricant coatings usually have high durability, coating thickness consistency, and shelf life, they also have a low potential for contamination. Dry lubricant coatings, such as silicone, diamond-like carbon coatings, and metallic glass coatings, have been commonly used on surgical equipment, catheters, and syringe needles [17-21].

Silicone coatings have been utilized in various biomedical areas because of their properties, such as transparency, colorlessness, and excellent miscibility with water. One study has shown that silicone coatings on disposable hypodermic needles increase their sharpness and durability. However, the dislodgement of the coating and its residue left inside the tissue can be hazardous [17].

Diamond-like Carbon (DLC) has been considered a favorable option for biomedical applications because of its valuable properties such as corrosion resistance, biocompatibility, and hemocompatibility. DLC coated needles, which were used in ophthalmic surgery, have reduced the friction involved in penetrating the pig eye cornea by around 30%. Nevertheless, the high residual compressive stress of the DLC coating can cause it to delaminate from the surface if the adhesion is not adequate, which may not only nullify the coating effect but also degrade the surface of medical devices. This issue is especially significant in medical surgeries such as orthopedic and cardiovascular. The spallation, delamination, and corrosion of the coating during its long-term use in medical devices must be thoroughly considered for its future biomedical applications [18].

Doerzbacher et al. [37] investigated the use of Diamond-like Carbon (DLC) and Parylene coatings to improve lumbar drain procedures. A configuration was designed to simulate the process of lumbar catheter insertion. This involved employing a pneumatic cylinder to grip and advance the catheter in segments of 15 mm, at a consistent speed of 3 mm/s. A force sensor was attached to the cylinder clamp to measure forces. The researchers found that the DLC and Parylene coatings reduced the friction force between the needle and catheter by 24.2% and 34.9%, respectively, compared to a bare catheter [37].

Thin-film metallic glass (TFMG) exhibits high strength, good corrosion resistance, and wear resistance due to its lack of long atomic periodicity. Recent research has also shown that TFMG exhibits excellent biodegradability and biocompatibility. When applied to surgical needles, the TFMG film provides significant antibacterial properties, sharpness, and durability. The TFMG film is grown onto the needle using the radio-frequency magnetron sputtering technique [19].

Polytetrafluoroethylene (PTFE) is a coating polymer often used in the field of biomedical research. Its popularity stems from a range of helpful characteristics, including reduced friction, resistance to microbes, water-repellent nature, compatibility with biological systems, and resilience to chemicals or medications. To achieve adhesion between PTFE and a surface, researchers typically employ surface roughening techniques and/or primer coatings. Several primers have been studied and utilized, including polyamide acid [38] and blends of fluorinated ethylene propylene/PTFE [39]. However, this method is typically costly and results in thick films, rendering it unsuitable for applications that require thin coatings.

Additionally, needle stiffness becomes a vital factor when it comes to the process of inserting it into soft tissues. Conventional stainless-steel needles have a higher impact on the insertion force and deflection than polymer needles. Polymer needles are typically used as prototype needles to study different needle shaft and tip geometries. For instance, Gidde et al. [23,27] studied a mosquito-inspired polymer needle to reduce the total interaction forces between the needle and tissue interface. Utilizing a needle designed after the mosquito anatomy led to a 60% decrease in the force required for insertion, and a 48% reduction in tissue deformation, in comparison to traditionally designed polymer needles. A similar mosquito-inspired needle design was also used in Kim et al. research paper [40], where the researchers were able to reduce the insertion force by mimicking the vibration (i.e., 1 to 1000 Hz) at the needle surface, similar to the mosquito stinger vibration.

The polymer needle is typically used as a prototype needle because it is easier to manufacture with complicated needle designs and is also cost-effective compared to conventional stainless-steel needles [22,27,41]. Some polymer needles offer a variety of advantages over conventional needles, such as transparency and biodegradability. Many polymer needles can be easily manufactured using a 3D printer, making it easier to fabricate complicated needle designs. In contrast to the advantages mentioned above, polymer needles also have downsides, such as shear-driven breakage due to the polymer viscoelasticity. For this reason, polymer needles have to be scaled up 2X compared to conventional stainless-steel needles. For example, Gidde et al. [23,27] used a polymer mosquito-inspired needle with a diameter of 3 mm instead of the conventional 1.27 mm stainless steel needle. The polymer used in their study was made of isononyl acrylate (25%), phenol (15%), acrylic monomer (35%), and a modest percentage of various polymers. When it comes to the deflection of needles, the needle tip is the most significant influencer in directing and bending the needle. For example, trocar and conical tip needles usually experience very small to negligible bending compared to bevel tip needles [14,21].

Additionally, various bevel angles also change the cutting force and bending of the needle [22,29,42-44]. Barnett et al. [43] examined a distinct tip geometry for the needle, characterized by slit shapes at the tip. This design facilitated the transformation of longitudinal cutting into transverse cutting, consequently lowering the cutting force required. Van de Berg et al. [44] studied the influence of various shapes and designs of the tip, such as bevel, conical, beveled with pre-bend, bevel with pre-curve, conical with pre-bend, and conical with pre-curve. From various studies, it can be determined that changing the needle tip not only changes the needle steering and bending but also changes the cutting forces [22,29,42-44].

Tissue mechanical properties, such as tissue stiffness, influence the insertion forces. Most complex structured tissues comprise several layers, including skin, muscle, fatty layers, and soft connective tissues, which typically have different stiffness [3,4]. This variability in stiffness influences needle insertion and bending during the insertion and extraction. The bovine kidney serves as an example of tissue with a complex structure. In this thesis, a bovine kidney was utilized for conducting tests on biological tissues. The cross-section of the bovine kidney is depicted in Figure 1.4, highlighting its distinct components, such as the fibrous capsule, cortex, medulla, and pyramids. Each of these components exhibits varying levels of stiffness properties.

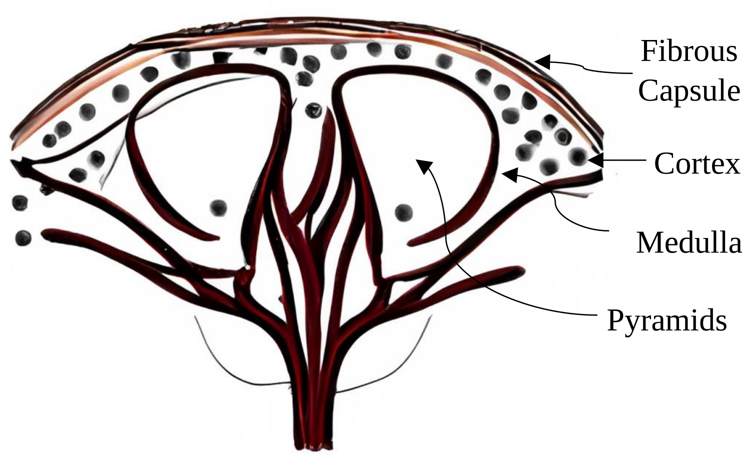

Figure 1.4 Cross-section of bovine kidney tissue with labeled parts i) Fibrous Capsule, ii) Cortex, iii) Medulla, and iv) Pyramids.

Another example of biological tissue is the prostate, which consists of four main layers: skin, subcutaneous fat, muscle, and the prostate gland. Each layer exhibits different heterogeneous properties that can impact surgical procedures, such as brachytherapy [45-

47]. Most researchers utilize artificial tissues, such as Polyvinyl chloride gel (PVC), gelatin, silicone, plastisol, and other similar materials that mimic biological tissues to study the effects of tissue mechanical properties. Therefore, most of the initial experiments were conducted on artificial tissues. If necessary, further experiments are performed on biological tissues to validate the results obtained from the initial experiments based on the hypothesis. Ideally, artificial tissues have homogeneous mechanical properties, whereas biological tissues have heterogeneous properties. Insertion forces have a direct relation to tissue stiffness. For example, the insertion force for a 5 kPa tissue will always be lower than that of a 10 kPa tissue because the stiffness of the tissue individually affects cutting and friction forces, which in turn affects the insertion force [4,43,47]. If the needle stiffness is lower than the tissue, the needle will likely bend more, making it necessary to use a higher stiffness needle than the tissue to avoid the bending [46-52].

1.1.3 Speed and Technique of Inserting Needle

Various needle insertion speeds produce different friction and cutting forces inside viscoelastic tissues during needle insertion and extraction. Several researchers have investigated the effect of speed on needle insertion and extraction forces and tissue deflection [11,15,53-55]. Mahvash et al. [53] conducted a study to investigate the impact of insertion speed on puncture force and tissue damage. They examined a range of speeds from 1 mm/s to 100 mm/s and consistently observed a reduction in puncture force, increased friction force, and tissue damage. Heverly et al. [55] also studied the insertion speed impact on the needle puncture force. They studied the insertion speed of 5 mm/s to

20 mm/s and found that the puncture force decreases as the insertion speed increases. Furthermore, as the insertion force increases, cutting force, tissue deflection, and deformation also increase, as demonstrated in Casanova et al. research article [54]. They conducted the study using insertion speeds ranging from 0.2 mm/s to 10 mm/s. In short, increasing insertion speed may help to reduce the puncture force, but it increases friction and cutting force, ultimately increasing insertion force and causing tissue damage [4,5,54].

The insertion technique is another significant factor influencing the insertion force. Various techniques have been explored, including rotating needle insertion [12,56] and applied vibration method [57]. Gidde et al. [27] employed a needle influenced by the mosquito structure, along with a vibrational insertion method. Their research found a 60% decrease in the force needed for insertion and a 48% reduction in tissue deformation when compared to needles of traditional design. They conducted a study on vibrational frequencies ranging from 0 Hz to 500 Hz and found that the insertion force and tissue damage decreased from 0 Hz to 200 Hz. However, they observed an increase in insertion force and tissue damage when the frequency exceeded 200 Hz, up to 500 Hz. Barnett et al. [43] conducted a study on the insertion force of hypodermic needles, investigating the effect of varying vibration frequencies. They examined frequencies ranging from 100 Hz to 20 kHz and observed that the insertion force decreased as the vibration increased. The advantage of utilizing vibration is a reduction in friction and cutting force [27,56,57], consequently aiding in reducing the overall insertion force and tissue damage.

1.2 Histological Analysis for Tissue Damage

Histological analysis is often used to comprehend the structural composition and detect any abnormal changes in tissues [9,23,58]. There are very few available studies that have specifically examined the effect of needle coating on tissue damage. Most researchers who have studied different coatings have focused on insertion force and needle properties [18,19,36,37,59]. Therefore, it is crucial to conduct further research to investigate the impact of needle coatings on tissue damage. In this paper, the focus is solely on studying the tissue damage area or cracks induced by needle insertion. This choice is made because tissue damage is linked to mechanical trauma, inflammatory response, and hemorrhage [54,58,60-64]. In order to conduct a histological study on tissue damage caused by needle insertion, several sequential steps are typically followed: sample collection, fixation, processing, staining, and microscopic examination. Reducing insertion force is crucial, even for small-diameter surgical needles. A relevant example of this necessity is evident in the research conducted by Casanova et al. [60], where they utilized a 32-gauge (0.235 mm) needle in ex-vivo experiments with living rat brain tissue. Their findings revealed that higher insertion speeds correlated with elevated insertion forces, leading to more tissue damage and a subsequent increase in hemorrhage. These observations raise greater concerns when considering larger-diameter needles or needle-like structures, further emphasizing the importance of minimizing both insertion force and tissue damage to enhance clinical outcomes and patient safety.

1.3 Needle-Tissue Insertion Force Model

Insertion force models play a crucial role in the use of medical devices, particularly needles, as they enable the measurement of the force needed to insert these needles into tissue. Insertion force models hold significant value in comprehending the mechanics involved in reducing the insertion force. By employing an insertion force model, it becomes possible to estimate needle insertion force parameters such as viscous and elastic forces of the viscoelastic tissue, as well as Coulomb friction force and cutting force, without the requirement of bulky haptic sensors [26,29,30,65-68].

The force model explained in this thesis is developed to fully understand the mechanics behind the decrease in insertion forces because of the composite coating. The friction force model is inspired by the modified Karnopp model [65] and has been augmented with an elastic force component. Additionally, this model can be utilized in real-time during the insertion to predict force parameters and improve surgical procedures and robot-assisted medical interventions.

The insertion force model incorporates various force constraints, for example Coulomb friction, viscous, elastic, and cutting forces. During needle insertion, once the needle insertion force surpasses the static friction force, the tissue ceases to move downward with the needle. Static friction is identified as friction that resists the initial needle sliding within the tissue. Once the insertion force overcomes the static friction force, the relative velocity between the needle and tissue becomes non-zero, and the force between the needle shaft and tissue is influenced by Coulomb friction, elastic, and viscous forces.

The Coulomb friction force is dependent on the surface roughness and normal force between the needle and tissue [26], while the viscous force depends on the needle insertion speed, time, and tissue stiffness [26,30]. Elastic force is contingent on tissue contact area deflection and tissue stiffness [67,68]. In the cutting force model, the cutting force acting between the needle tip and tissue ideally remains constant with a constant velocity [30]. The cutting force primarily depends on the needle insertion velocity and tissue stiffness.

In order to account for the viscous and elastic forces exerted by the tissue, this thesis utilizes the Kelvin-Voigt model as a means to characterize the viscoelastic properties. The Kelvin-Voigt model is made up of a spring and dashpot in parallel and is an appropriate choice due to the tissue stress-strain behavior, which is comparable to that of viscoelastic materials. This research first tested the proposed analytical model on PVC gel tissue and then advanced to bovine kidney tissue, which has similar mechanical properties and structure to human kidney tissue, to evaluate the model applicability to biological tissue [67]. The following paragraphs will further elaborate on the advantages and uses of these analytical insertion force models.

Researchers can use these models to compare the performance of different types of needle and insertion techniques to study the effects of various factors on insertion force. In addition, when researchers comprehend the forces associated with needle insertion, they can create designs that simplify the insertion process and minimize tissue damage which leads to minimizing patient discomfort. This might involve modifying the design and needle insertion techniques to lessen the necessary insertion force. In addition, healthcare professionals must have a solid understanding of the correct methods for inserting needles to reduce discomfort for patients and avoid causing injuries. Training materials, guided by an insertion force model, can help these professionals grasp the dynamics of the forces they will deal with during insertion and provide them with effective strategies for reducing the insertion force [29,30,66-68].

1.4 Research Motivation and Related Work

This research is inspired by the limitations of existing needle insertion techniques and the variety of needle designs that have been developed to reduce insertion force and tissue damage [14,17-19,21,27,37,59,69]. Due to certain procedural and manufacturing constraints, many needle insertion techniques and designs may only be universally applied to some medical interventions. For instance, the vibrational needle insertion technique may not be applicable in scenarios where the additional external equipment that produces vibrations hinders a surgeon ability to perform critical medical procedures proficiently [27,40,41]. Moreover, innovative bio-inspired needle designs, such as the mosquito-inspired needle developed by Gidde et al. [27] and the honeybee-inspired needle by Sahlabadi et al. [22], might not be feasible for manufacturing smaller-scale metal needles intended for clinical use. In response to these limitations, the application of a thin, biocompatible, low-friction composite coating on the existing conventional needle presents itself as a potential solution. This thin coating not only enhances the needle surface by reducing friction, but also helps maintain the original needle geometry and shape, which is crucial for many medical applications. Another advantage is that the utilization of the coated needle allows for the continued use of conventional insertion techniques that medical professionals are already trained in.

In addition, most existing needle insertion force models were developed with conventional bare needles in mind [3,10,15,30,65,68,70]. The mechanics behind the reduction of needle insertion force cannot be adequately explained using many conventional insertions force models, as they do not consider coating-affected parameters such as friction and viscoelastic properties of the tissue. This underscores the necessity for further research to address this gap and enhance the understanding of how coatings influence the force parameters during needle insertion with the insertion force model. By developing an insertion force model that incorporates coating-affected parameters such as Coulomb friction, viscous and elastic forces, and cutting force, it aids in understanding the coating mechanics and predicting these parameters. For example, if the analytical insertion force model predicts the Coulomb friction force for both the coated and bare needles, and it is observed that the coated needle has a lower Coulomb friction force, it indicates that the coating aided in reducing the Coulomb friction force. In this case, it can be interpreted that the coating helped to reduce the surface roughness, which in turn resulted in a reduction of the Coulomb friction force. This is because the Coulomb friction force is dependent on the surface roughness [71]. The understanding of these force parameters eventually leads to an improvement in the ability to optimize needle design and effectively minimize tissue damage.

In short, this thesis is motivated by the limitations of current needle insertion techniques and designs, which can be solved with the application of a thin, biocompatible, low-friction coating on the needle as a solution while also developing an analytical insertion force model that incorporates coating-affected parameters to understand the insertion force reduction mechanics.

1.4.1 Materials Selections for Biocompatible and Low-Friction Coating

Surface modifications to the needle, which can be achieved without altering the needle design or mechanical properties, entail the application of a thin, low-friction material coating to the needle surface [14,17-19,21,59,72,73]. For instance, Fraguas et al. [73] demonstrated that an atmospheric-pressure plasma-polymerized film coating on a conventional needle could significantly reduce the insertion force by 50% to 75%. However, the chemicals used in this coating, such as 3-aminopropyltriethoxysilane and ethylenediamine, are not biocompatible.

Another example of needle coating involves diamond-like carbon (DLC), where researchers have managed to reduce insertion forces by 30% [72]. Despite its benefits, the drawback of DLC coating is its low adhesion to needle surfaces, attributed to the high compressive residual stress at the atomic level. Foust [59] studied the coating of PDA and lowest friction PTFE without any filler materials and found irregularities and uneven coating during their experiments. This suggests the need to either adopt other coating methods, which could increase the cost and time of coating, or add a filler material to compensate for PTFE irregularities [59,74]. Beckford et al. [74] examined the composite coating of PDA and PTFE using copper as the filler material. Copper was added to compensate for the irregularities in PTFE. While this composite coating effectively reduces surface friction, it presents a potential risk of copper toxicity due to the leakage of toxic ions. So, it can be determined that the PTFE, which has the lowest friction coefficient, requires a bio-compatible adhesion medium and a bio-compatible filler material to avoid uneven and irregular coating. PTFE (Polytetrafluoroethylene), is recognized for its extremely low coefficient of friction, facilitating a minimal resistance when two surfaces slide over each other. The interposition of coating like PTFE between two surfaces reduces the adhesion or stickiness between those surfaces, resulting in decreased friction [14,21,38,59,74,75].

1.4.2 Insertion Force Model

Previous studies have introduced various methods to analyze needle-tissue insertion mechanics and measure force parameters for bare conventional needles. DiMaio [68] used a computer vision model to estimate force distribution on the needle shaft during insertion, with bulky haptic sensors attached to the needle. Abolhassani et al. [3,7,15] undertook a comprehensive review of the needle-tissue interaction force model, considering forces related to tissue deformation, deflection, trajectory planning, and applications. Kataoka et al. [76] designed a model to distinguish shaft forces from tip forces during needle insertion and found that friction forces were linear, leading to a consistently distributed clamping force. Gerwen et al. [4] examined the correlation between insertion force and its determinants through experimental data classification and employed a force model with force feedback to control needle insertion. Okamura et al. [30] broke down the insertion force model into three components: shaft friction force, cutting force, and pre-puncture force-stiffness force, considering the tissue to have viscous properties. Jiang et al. [66] modeled friction forces using a modified Winkler foundation model, assuming tissue elasticity and cantilever beam properties of the needle. However, to date, no model has considered the effect of needle coating on insertion force or incorporated the coating-affected parameters into their models. Therefore, it is difficult to individually measure and calculate these coating-affected parameters, such as Coulomb friction, and viscous and elastic forces, which are necessary for understanding the mechanics of insertion force reduction.

1.5 Problem Statement

1.5.1 Composite Coating of Polydopamine, Polytetrafluoroethylene, and Activated Carbon

The initial phase of the needle insertion process involves puncturing the top layer of tissue before progressing deeper. After the puncture, as the needle enters the tissue, both the needle tip and shaft come into contact with the tissue [3,10,12,21,22]. As the needle advances, the contact area between the shaft and the tissue gradually increases while the tip contact area remains constant. Throughout the insertion, the needle encounters a friction force between the needle shaft and the tissue and a cutting force that arises between the needle tip and the tissue [3,9,11,12,77]. As a result, the insertion force is defined as the sum of these friction force and cutting force. On the other hand, during needle extraction, the extraction force depends solely on the friction force. These insertion and extraction forces cause tissue damage and deformation due to the friction between the needle and the tissue. Therefore, reducing these insertion and extraction forces is crucial to minimize tissue damage and deformation, making surgeries less invasive.

To address these challenges, this thesis proposed a biocompatible and low-friction coating comprised of Polydopamine (PDA), Polytetrafluoroethylene (PTFE), and Activated Carbon (C). Among other biocompatible and low-friction materials, PTFE was selected in this research due to its lowest coefficient of friction and other beneficial properties, such as antimicrobial activity, hydrophobicity, non-stick nature, and resistance to chemicals or drugs. However, PTFE coating is not durable without using scratch coating techniques or applying a thick layer of the coating [21]. Thus, PDA was employed as an adhesive material between the PTFE and the needle surface in this study. Numerous researchers also suggest that using PDA as an adhesion medium significantly increases the durability of the coating [14,20,21]. Prior research indicated that a filler for PTFE is necessary to prevent irregularities and unevenness during its curing process [38,39,74]. Therefore, this thesis proposed using activated carbon as a filler material for PTFE, which prevents cracks and uneven surfaces during the PTFE sintering process. In addition, activated carbon filler possesses inherent lubricating and biocompatible properties. These properties of activated carbon further reduce the friction of the coating. In comparison to existing coatings, such as silicone, diamond-like carbon, and thin-film metallic glass, these might not be suitable for biological use if they become dislodged due to poor adhesion and errors in the complex, costly and time-consuming coating procedure [17-21,37]. In summary, this part of the thesis proposes to solve the tissue damaging needle insertion-extraction force challenge by applying the biocompatible and low friction composite coating of PDA, PTFE, and C on the needle surface.

1.5.2 Insertion Force Model of the Coated Needles

Parameters at the needle and tissue interface during insertion, such as Coulomb friction, viscous forces, and elastic forces, are influenced by low-friction needle coatings. Understanding the mechanics of the coating effect requires the measurement of these force parameters. However, it is impossible to measure these parameters during needle insertion into the tissue without adding bulky haptic sensors on the needle surface. The only parameter that can be easily measured externally is the insertion force. Therefore, this thesis addressed these challenges through the analytical insertion force model. This model is designed to distribute the measured insertion force into the coating-affected parameters. Furthermore, it calculates the cutting force using the cutting coefficient and insertion velocity [77].

The proposed analytical model consists of two main components: the friction force model and the cutting force model. The friction force model is based on the modified Karnopp model [71]. To distribute the friction force in their study, the model incorporated a least square regression method that divided the friction force into Coulomb friction and viscous forces. In this thesis, an addition has been made to include the elastic force, which represents the elastic properties of the tissue. Therefore, the proposed friction force model in this thesis considers Coulomb friction, viscous, and elastic forces acting on the needle shaft. On the other hand, the cutting force model is represented using a cutting force, constant cutting coefficient and needle insertion velocity. Here, the cutting force depends solely on the tissue stiffness and insertion velocity [77]. The application of this model in pre-planning and force prediction, in conjunction with data collection, can offer valuable insights during surgical procedures. Various insertion force models, primarily developed for conventional, bare needles, often oversimplify tissue properties by categorizing them as either elastic or viscous [29,30,65,66,68,71,76]. These models do not adequately capture the viscoelastic behavior of tissues during coated needle insertion, nor do they account for the impact of various force parameters associated with different coatings. In summary, this thesis tackles the understanding of insertion force reduction by developing an analytical insertion force model for coated needles. This analytical insertion force model incorporates various parameters, including Coulomb friction force, viscous force, elastic force, and cutting force.

CHAPTER 2

MATERIALS AND METHODOLOGY

This thesis is divided into two main sections. The first section investigates the effects of needle coating on needle surface properties, needle-tissue insertion and extraction forces, and tissue damage. These effects were evaluated through a series of experiments conducted on PVC tissue and bovine kidney samples. The second section focuses on the development of an insertion force model, which comprises two sub-models: the friction force model and the cutting force model. The friction force model incorporates both Coulomb friction forces and the viscoelastic forces of the tissue, encompassing both viscous and elastic forces. The cutting force model, on the other hand, considers cutting force coefficients and insertion velocities as its key parameters.

2.1 Effect of Needle Coating on Forces, Surface Properties, and Tissue Damage

This section encompasses the fabrication of various experimental apparatus and setups, needle coating procedures, experiments focused on analyzing the insertion-extraction forces of both bare and coated needles, investigations into the surface properties of both coated and bare needles, as well as the assessment of tissue damage caused by both coated and bare needles.

2.1.1 Needle Coating Process

A dip coater is a device utilized to apply a thin coating on the surface of a solid object. A dip-coating machine was utilized for the coating of the needles throughout this research. It works by immersing the object in a liquid coating material and then lifting it out at a controlled rate to create a uniform coating. The dip coater (Custom-fabricated using the Velmex UniSlide® MA40, Velmex, INC, Bloomfield, NY, USA) used in this research can coat needles up to 15 cm in length. Several fixtures were re-designed before moving toward the coating procedure of the needles. First, the dip coater fixture was designed in SolidWorks (Dassault Systems SOLIDWORKS Corp., Waltham, Massachusetts, USA) and then 3D printed with ABS plastic in a 3D printer. This fixture can accommodate eight needles at a time for the coating (Figure 2.1). Next, the fixture was attached to the arm of the dip-coating machine. This fixture can hold biopsy needles and suturing needles for the dip coating. Another fixture was designed to attach the needle to the force sensor. This fixture can be directly screwed to the force sensor, and then the needle can be attached to its opposite end.

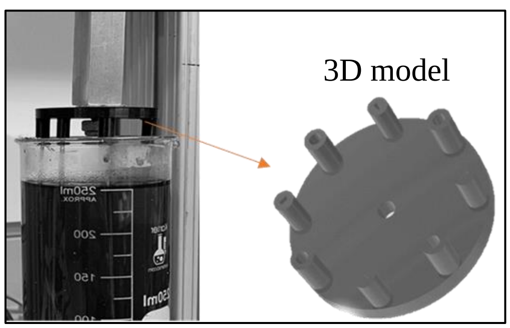

Figure 2.1 3D printed fixture for the dip coating machine.

In this thesis, the fabrication of a composite coating for surgical needles is detailed, combining PDA for its robust adhesive qualities with PTFE and C to form a coating that exhibits low friction [78,79]. In this study, activated Carbon powder with a grain size of

250 microns was utilized as a filler to reinforce PTFE cracks and uneven surfaces [20,74]. Throughout this research, stainless-steel biopsy needles (Vita Needle Company, Boston, MA, USA) with a diameter of eighteen-gauge, equivalent to 1.27 mm, and featured a sharp trocar tip with a length of 0.2 cm were utilized. The PDA solution used in the study was prepared by combining dopamine hydrochloride ($(HO)_2C_6H_3CH_2CH_2NH_2.HCL$) (H8502, Sigma Aldrich, St. Louis, MO, USA) and tris (hydroxymethyl) aminomethane $NH_2C(CH_2OH)_3$ (T1503, Sigma Aldrich, St. Louis, MO, USA). To prepare the trisma (tris) base solution, 1.5 g of trisma powder tris (hydroxymethyl) aminomethane $NH_2C(CH_2OH)_3$ was added to 200 ml of deionized water to create a 50 mM trisma base solution. The pH of the solution was subsequently modified to 8.5, a process conducted with the assistance of a pH meter (Fisherbrand™ accumet™ AE150 Benchtop pH Meter, Hampton, NH, USA). Next, 2mg/ml dopamine hydrochloride was added to the trisma base solution and mixed using a magnetic stirrer machine (VWR Dyla-Dual Hot Plate/Stirrer, Model 942009, Radnor, PA, USA) (Figure 2.2 (a)) [20,21,74,75]. Prior to depositing the polydopamine coating on the needles surface, they were cleaned in order to eliminate impurities using deionized water. The stainless-steel needles were submerged with a clamping laboratory stand in the PDA solution for 24 hours to allow for the growth of a thin coating of PDA on the needle surface. After the coating process, also referred to as polymerization in this context, the needles were removed from the solution and rinsed with deionized water prior to the deposition of the PTFE and PTFE-C topcoat [80,81]. The ready-made PTFE solution (Disp 30 DuPont, Fuel Cell Earth, LLC, Woburn, MA, USA) and PTFE mixed with

activated carbon (Aldon Corporation, Avon, Y, USA) were placed in the dip-coating machine to further coat the PDA-coated needles (Figure 2.2 (b) and (c)). The activated carbon was added to the PTFE solution at a concentration of 2.5% w/v.

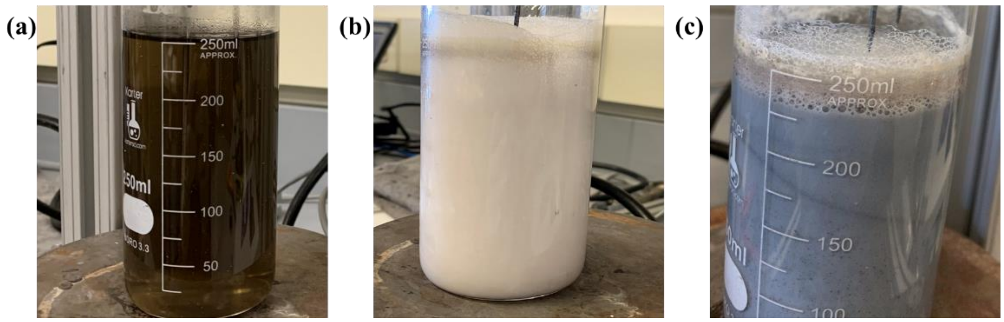

Figure 2.2 (a) Chemical solution of PDA, **(b)** Chemical solution of PTFE, and **(c)** Chemical Solution of PTFE+C.

The PDA-coated needles were then dipped into the PTFE and PTFE-C solution at a speed of 10 mm/min and kept for 3 minutes to form a thin PTFE and PTFE-C layer on the surface of the needles. Subsequently, the needles were extracted at a speed of 10 mm/min. The PDA-PTFE and PDA-PTFE-C coated needles were then placed in an oven and dried at 120ºC. Afterward, the needles were transferred to a furnace and heated up to 373ºC to remove water particles and the coating wetting agent, a process known as sintering [20,21,74]. After cooling naturally to room temperature, the needles were ready to be used for further experiments. The structure of PDA-PTFE-C coating and the coating process flow chart is shown in Figure 2.3 and Figure 2.4, respectively.

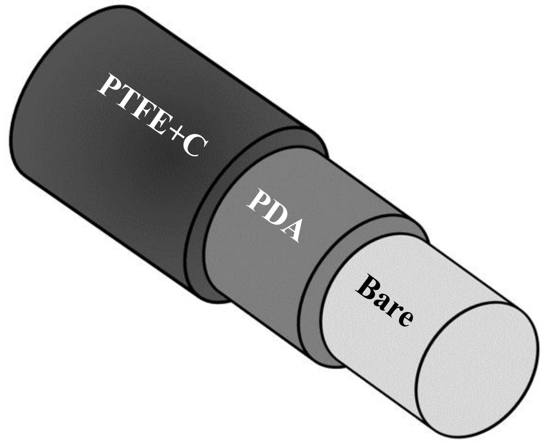

Figure 2.3 Structure of PDA-PTFE and C layers.

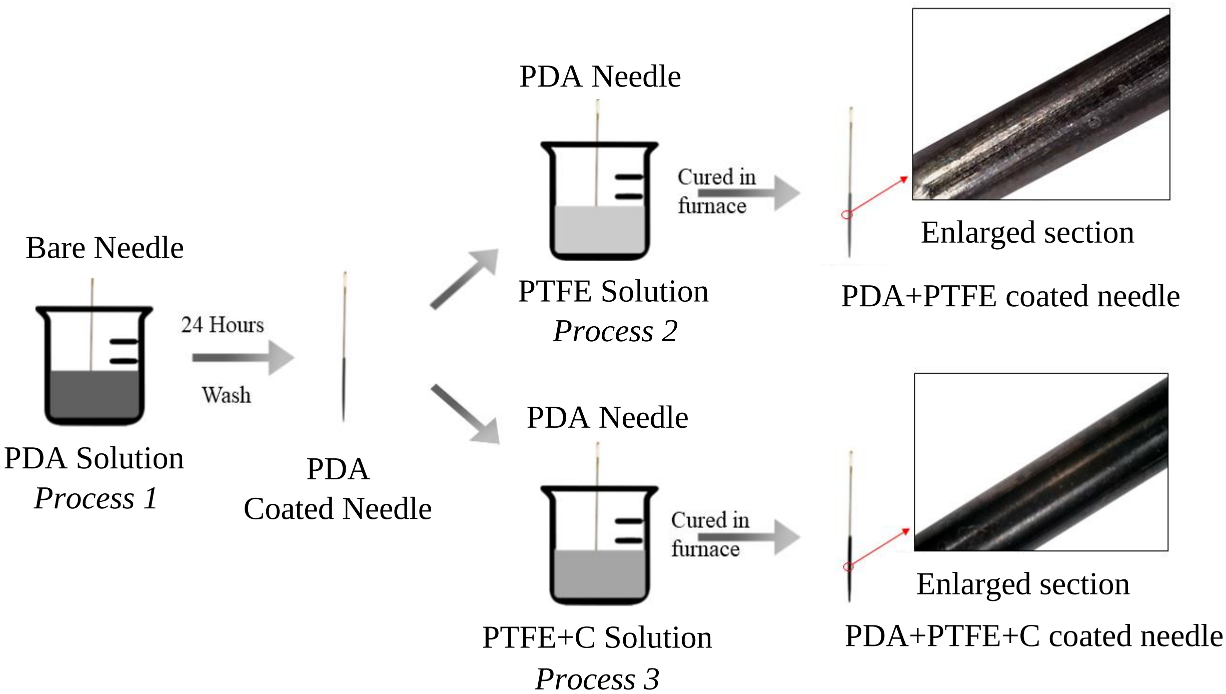

Figure 2.4 Process 1- Coating of the Bare needle with the Polydopamine; **Process 2 –** Coating of PDA coated needle with the PTFE; **Process 3 –** Coating of PDA coated needle with the PTFE and Activated Carbon.

Subsequent Section 2.1.2 delves into the comprehensive analysis of the measured insertion and extraction forces. The detailed measurements and methodologies presented in this section aim to provide valuable insights into the effects of the coated needle during both the insertion and extraction processes.

2.1.2 Measurement of Needle Insertion-Extraction Forces

The primary experiment of needle insertion force measurements was performed on the PVC tissue with custom tissue fixture. To create a PVC tissue phantom, a blend of PVC polymer hardener (M-F Manufacturing Co, Fort Worth, TX, USA) and diethyl hexyl softener (M-F Manufacturing Co, Fort Worth, TX, USA) was heated to 150°C, transforming it into a thick, transparent solution [49,82]. The stiffness characteristics of the PVC phantom can be varied from 2 kPa to 40 kPa by modifying the elements within the diethyl hexyl materials. It is crucial not to overheat the solution, as this may alter the tissue properties. When the solution attains the necessary consistency, it is transferred into an aluminum mold and allowed to cool down to ambient temperature. To solidify the solution, the mold is then placed in a freezer, resulting in a white, semi-opaque PVC tissue phantom that closely emulates the viscoelastic properties of biological tissues (Figure 2.5(a)) [48,82]. The phantom tissue used in this experiment had two different stiffness layers. The bottom layer of the phantom tissue has a dimension of 15×15×1.5 cm^3 with a stiffness of 5 Kpa, and the top layer has a dimension of 15×15×2 cm^3 with stiffness of 2 Kpa. After curing the bottom layer in the fridge, the top layer was directly poured on top of it and cured for 24 H in the fridge. It was extremely challenging to imitate different tissues and veins of the bovine kidney; therefore, only two tissue cortex (2 kPa) and medulla (5 kPa) stiffness were manufactured for the experiments [46].

The tissue holding fixture was designed using the 3D modeling software Solidworks (Dassault Systems SOLIDWORKS Corp., Waltham, Massachusetts, USA) and fabricated it with polyethylene terephthalate glycol (PETG) material using a 3D printer (Figure 2.5 (b)). The fixture consists of top-bottom parts, designed in a way that minimizes tissue movement due to needle-tissue sticking. Both parts have circular holes for the needle to pass through the tissue completely, from one side to the other.

(a) (b)

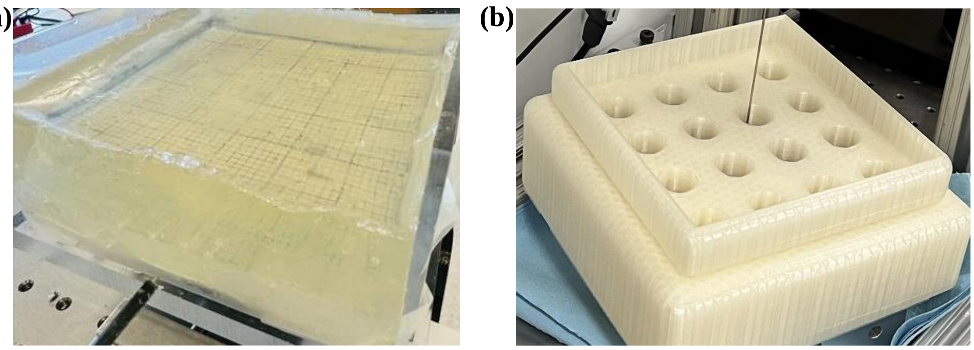

Figure 2.5 (a) PVC gel tissue sample and **(b)** 3D printed tissue fixture.

The setup used for testing needle insertion and extraction forces in this study includes a linear motor actuator (Velmex Unislide® MA40, Velmex, INC, Bloomfield, NY, USA) with an attached three-axis force sensor Nano17® (ATI Industrial Automation, Apex, NC, USA, resolution: 1/160 N, maximum range: 17 N), a needle fixture connected to a force sensor, a data acquisition system (DAQ) (National Instruments Corporation, Austin, TX, USA), and a tissue holding fixture. During the experiment, the force sensor measured the forces of insertion and extraction along the z-axis. The data were acquired using a programmable data acquisition system that utilized LabVIEW software on the computer. To ensure data accuracy, the experimental setup involved conducting experiments in an airspace without any tissue, and then subtracting this air-measured data (referred to as dead-force) from the experimental data obtained from tissues. Figure 2.6 illustrates the needle insertion test setup, where the experiments were conducted on phantom tissues (PVC tissues) and biological tissues (bovine kidneys).

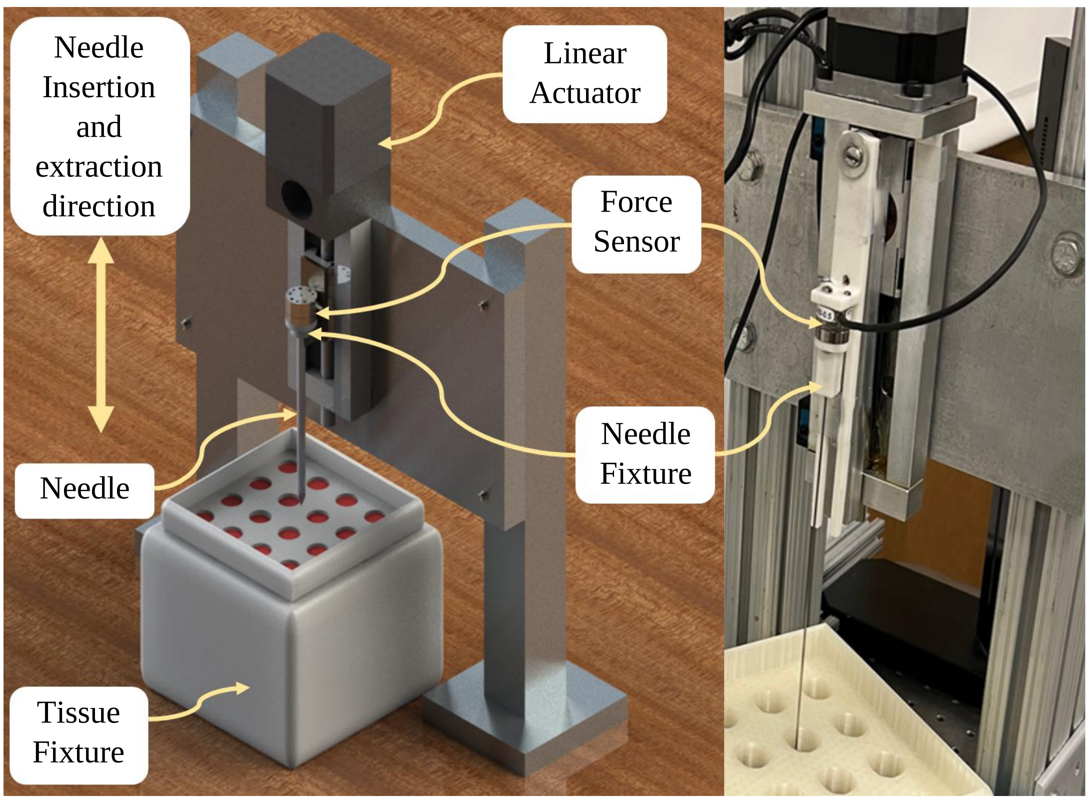

Figure 2.6 Experimental test setup to measure the insertion-extraction forces.

During the experiments, five insertions and extractions were performed with each of the three sets of bare and coated needles to gather a comprehensive set of data. The test setup was designed to control and monitor the insertion and extraction procedures at a uniform insertion velocity of 5 mm/sec. This ensured that the needles were inserted and extracted at a constant speed, eliminating any potential bias in the results due to variations in insertion and extraction speed. The experiments for measuring insertion and extraction forces were conducted at room temperature (20ºC).

The maximum insertion depth was set at 35 mm to ensure the needles reached sufficient depth into the tissue. So, the needle took approximately 14 seconds to finish the one insertion and extraction procedure at 5 mm/s constant speed. The force sensor was programmed to start recording the force as soon as the needle touched the tissue, ensuring that the force measurements were precise and consistent. After each insertion and extraction procedure, the tissue holder was relocated to a minimum distance of 2 cm from the previous insertion site in preparation for the subsequent insertion and extraction. This helped to ensure that the measurements were taken at different locations and that the tissue did not become overly damaged or distorted in any particular area. The sets of data were recorded using programmable LabVIEW data acquisition software (National Instruments Corporation, Austin, TX, USA), which facilitated the easy collection and organization of data. The force sensor was a critical component of the experiment as it provided precise measurements of the forces applied during the insertion and extraction procedures.

2.1.3 AFM Study of Coated and Bare Needle Surface

An atomic force microscope (AFM) was used to analyze the surface texture and friction profile of the needles. The surface roughness of coated and bare needles was measured using the contact mode method in the AFM. In AFMs with a laser and photodiode setup, a laser beam is focused onto the cantilever AFM probe tip, while a photodiode detects the reflected laser beam. When the cantilever AFM probe tip interacts with the sample surface, it deflects, causing a change in the position of the laser spot on the photodiode. This change in light intensity is converted into an electrical signal by the photodiode. The signal is processed, amplified, and filtered to extract deflection information. The processed signal is then used in a feedback loop to control the cantilever position, maintaining a constant deflection. As the cantilever is scanned across the sample surface, the deflection data is recorded and used to reconstruct an image of the surface [83]. This setup enhances sensitivity and accuracy in detecting cantilever deflections, enabling high-resolution imaging and precise measurement of sample properties.

The scan size was set at 30 microns, and at least five random areas were measured for each sample. To ensure accuracy, the roughness data were averaged. To measure the surface friction force, the lateral force microscopy (LFM) method in the AFM was employed [84]. Experiments were performed with a scan angle of 90° and a scan area of 30 microns. During the LFM measurement, one line was reciprocally scanned in the direction perpendicular to the cantilever beam (right direction), and one image was obtained by sequentially moving this measurement line in another direction (left direction).

The right and left scanning directions of the images were referred to as trace and retrace, respectively. The friction force profiles were processed by subtracting the trace scan image from the retrace scan images to enhance the friction force data. The tracking force during the scan was kept constants for all samples. The friction force (f_f) can be calculated as $f_f = Vt.k.DS$, where Vt is the measured voltage, k is the spring constant, and DS is the calibrated deflection sensitivity [85].

After analyzing the impact of the coating on the insertion-extraction forces of the needle and analyzing the factors contributing changes between the coated and bare needles surface, it is essential to explore another hypothesis. This hypothesis seeks to investigate whether using a coated needle can effectively reduce tissue damage compared to a bare needle. To address this hypothesis, a comprehensive histology study was conducted. The upcoming section provides a detailed description of the histology study, including the methodology, experimental procedures, and imaging technique employed.

2.1.4 Histological Study

Numerous research studies have demonstrated that there is a direct relationship between the force required to insert a needle and the extent of tissue damage that can occur [9,23,54,61-64,86,87]. A histological study is conducted to understand the structure, composition, and any abnormal changes in tissues. Needle insertion into the tissue can cause various types of damage, which depends on factors such as needle size, needle surface properties, insertion technique, tissue type, and penetration depth.

Damage caused by needle insertion includes mechanical trauma, inflammatory response, hemorrhage, and foreign body reaction [61-64,86,87]. When conducting a histological study on tissue damage caused by needle insertion, one typically follows these steps: sample collection, fixation, sectioning, staining, and microscopic examination [9,23,61-64,86-88]. Histological studies are essential in understanding the nature and severity of tissue damage caused by needle insertion. The findings can help medical professionals to improve needle insertion techniques, evaluate medical device safety, and develop tissue repair and regeneration strategies.

To gain a better understanding of this relationship, a histological study was conducted using two heterogeneous biological bovine kidneys. The study compared the use of composite-coated PDA-PTFE-C needles with that of bare needles during insertion and extraction from the kidney. The modified cassettes shown in Figure 2.7 were used to collect tissue samples. These cassettes were designed with holes at the top and bottom, and the dissected tissues were placed inside them. Subsequently, the needle insertion-extraction was performed through the rectangular hole where the tissue samples were. Typically, many researchers conduct the needle insertion-extraction experiment first, then dissect the tissue and place it into the cassette. This approach may lead to a disruption in the original needle insertion-extraction hole, so in this research, dissection was performed first, followed by the insertion-extraction experiments.

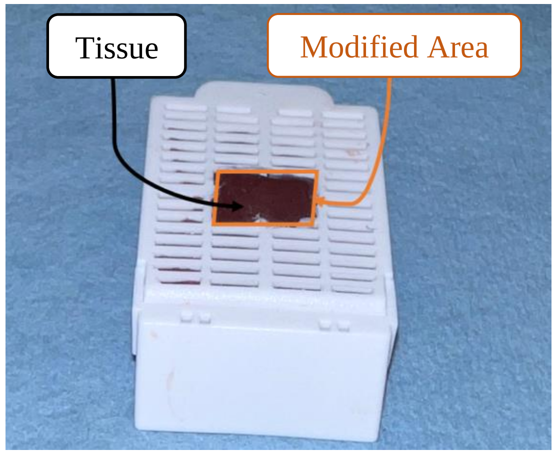

Figure 2.7 Modified cassette with the tissue sample.

After extraction, the tissue samples were placed in a plastic container with 10% formalin to fix them (Figure 2.8 (a)). The cassettes were soaked in the formalin solution for 48 hours before being transferred to 70% isopropyl alcohol to remove any remaining water. After dehydration and clearing, the tissue is embedded in paraffin wax for proper infiltration (Figure 2.8 (b)) [9,23,61-64,86-88].

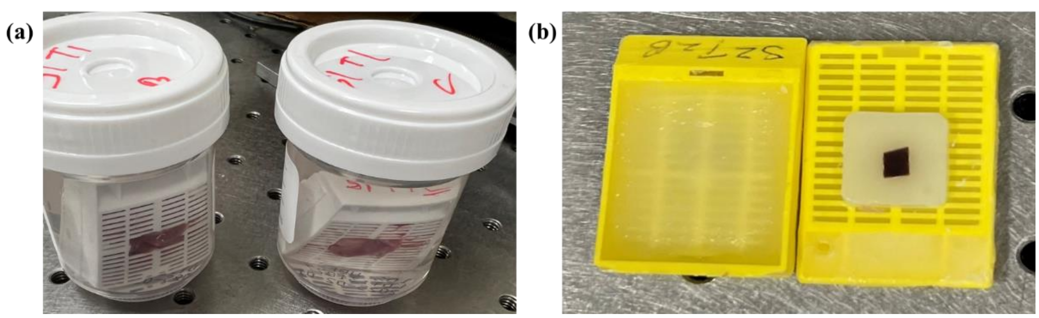

Figure 2.8 (a) Tissue fixation in 10% formalin solution and **(b)** Paraffin-embedded tissue samples.

Next, a microtome was used to section the tissue, with sections trimmed to a size of 0.5 cm x 0.5 cm and thin sections of 0.5 μm cut. The 0.5 μm sections were placed on glass slides and treated with hematoxylin and eosin (H&E) stains to prepare them for histological analysis. For the histological evaluation of the bovine kidney tissue sample, various solutions were mixed, including hematoxylin, eosin Y, dimethylbenzene, and ethyl alcohol. These were subsequently placed into tissue-tek station dishes. To achieve the desired hematoxylin and eosin (H & E) stain, a range of ethyl alcohol concentrations were obtained by diluting 100% ethyl alcohol with deionized water. Slides underwent a dehydration process, being submerged first in 100% xylene and then in a 50:50 mixture of xylene and ethyl alcohol, with each immersion lasting 5 minutes. Subsequently, the slides were immersed in various concentrations (70-100%) of alcohol for five minutes each. They were then immersed in a solution containing 1% hematoxylin by volume for five minutes and washed twice with deionized water. The slide samples were next dipped in an eosin Y solution with a concentration of 1% by volume for a duration of twenty seconds, followed by a double rinse with deionized water. The procedure was then executed in descending order, as the samples were submerged in graded alcohols, in descending concentrations from 100-70%, for five minutes at each stage to rehydrate the slides. To finalize the staining method, the samples were submerged in 100% xylene for 5 minutes. Upon concluding the staining, the slides were set aside to air dry for a ten-minute period. Afterward, each slide containing the sectioned and stained material had 100 μL of permount applied. Uniformity in the physical attributes of the tissue sections was maintained by adhering to all previously described protocols during the preparation stage prior to staining [9,23,61-64,86-88]. Both groups of samples underwent an identical process. Following this, coverslips were positioned on the stained slides, accompanied by drops of permount solution. Manual pressure was exerted to eliminate any surplus permount and air bubbles within the slide and coverslip. Subsequently, they were set aside to air dry for a whole day prior to examination. The final prepared slides are depicted in Figure 2.9.

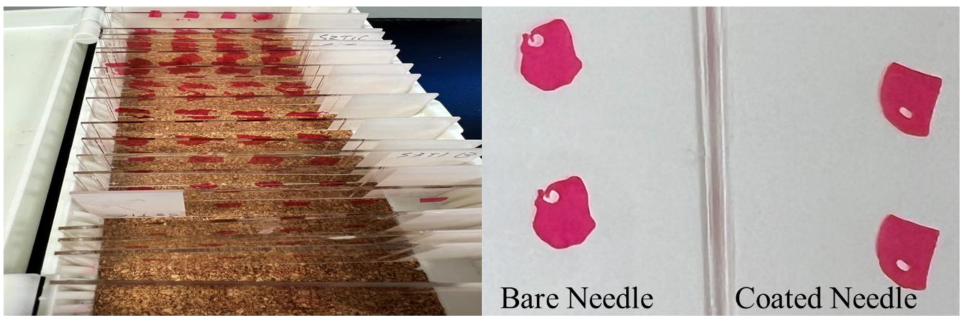

Figure 2.9 H&E-stained tissue samples on slides.

An Olympus GX-71 Inverted Microscope (Olympus Corporation, Shinjuku City, Tokyo, Japan), equipped with an Olympus U-TVO.5XC-2 color camera (Olympus Corporation, Shinjuku City, Tokyo, Japan), was utilized to examine and capture images of the stained slides. The magnification ranged from 5X to 10X, depending on the quality of the microscopic picture, and the exposure time and brightness were maintained throughout the imaging process. The analysis of the insertion hole area for both coated and bare needles were conducted utilizing the ImageJ software (National Institutes of Health, Bethesda, MD, USA). To make selecting the insertion hole area easier, the images were converted to grayscale (8-bit) and calibrated the software with a reference line of 250 µm. Then, using the wand tool, the irregular insertion hole was selected to measure the area. The procedures used to calculate the cross-sectional area of the damage are consistent with standard practices [9,23]. In the sectioned sample with a thickness of 0.5 µm, the damage area remained relatively stable following H&E staining. This consistency allowed for a comparison of the results with those derived from using bare needles. In short, the histological procedure can be summarized in the following flow chart (Figure 2.10).

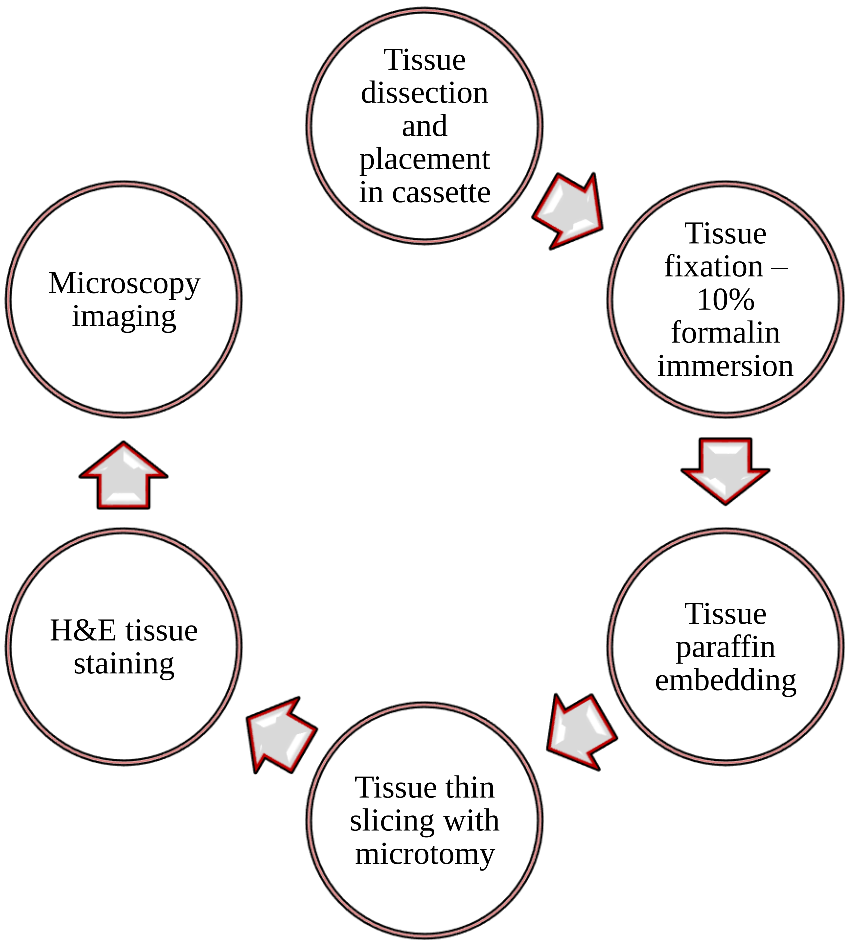

Figure 2.10 Histological procedure flow chart.

The previous sections discussed the needle coating procedures, including their surface properties, and examined their effects on tissue damage. In addition, it is essential to study all force parameters that come into play during the interaction between the needle and tissue, including viscous and elastic forces. Given the impracticality of separately measuring the Coulomb friction force, viscous forces, and elastic forces during the insertion of a needle into the tissue, the second half of the thesis focuses on explaining the development of a comprehensive analytical insertion force model. This detailed model is presented and explained in the subsequent sections, aiming to provide a more understanding of the forces involved in the needle-tissue interaction.

2.2 Analytical Insertion Force Modeling and Related Experiments

In a journal article I previously authored [89], I explored the details of the mechanics involved in needle insertion into viscoelastic tissue, particularly emphasizing the parameters of insertion force influenced by the coating. Several factors play a crucial role in determining the mechanics of needle insertion, including needle design, material, geometry, and tissue properties. One of the important forces involved in needle insertion is friction force, which is affected by various factors such as the properties of the surfaces in contact, the geometry and topology of the contact area, and the level of lubrication between the surfaces. The needle friction force is the force that opposes motion between the surfaces in contact, and thus, as the insertion depth increases, friction force increases. In contrast, the cutting force is influenced by the needle insertion speed and the tissue stiffness properties. Cutting force is the force that is required to cut the tissue during the insertion process. The cutting force remains constant throughout the insertion process. The insertion force is the resultant force acting on the needle during the insertion process. It is a combination of both friction force and cutting force. Understanding these forces is crucial to optimize the design and performance of needles in medical applications. Therefore, the following paragraphs describe the friction force, cutting force, and insertion force models in more detail.

2.2.1 Friction Force Modeling: Modified Karnopp Model

In this segment, a detailed explanation of a friction force model is provided. Friction is a tangential force that occurs between two bodies that are in contact with each other and sliding against each other [90]. The Coulomb friction model is the most commonly used friction model, which accounts for dynamic friction [89,90]. This Coulomb friction model is based on the idea that the friction force is proportional to the normal force and is independent of the velocity of the sliding surfaces.

However, it has been demonstrated by Karnopp that in addition to dynamic friction, the sliding surface also experiences static friction [65]. Static friction is a force that acts to resist the initial motion of an object that is in contact with another object. To account for both dynamic and static friction, Richard developed a modified Karnopp model in 1999 to identify the friction of real-time devices for haptic display [71]. The modified Karnopp model combines the Karnopp and linear viscous models. The linear viscous model assumes that the friction force is proportional to the velocity of the sliding bodies. By combining these models, the modified Karnopp model is able to accurately capture both static and dynamic friction forces. Overall, the development and explanation of this friction force model is important for understanding the behavior of sliding bodies in contact with each other. In addition, it highlights the importance of accounting for both static and dynamic friction when modeling friction forces, which can be useful in a variety of applications, including haptic displays and robotics.

This dissertation presents a modified friction force model that takes into account the elastic properties of tissue in addition to static and Coulomb friction forces and viscous forces. The modified model is based on the Karnopp model, which is commonly used to describe friction forces, and extends it to include the effects of tissue deflection. To accurately model the behavior of tissue, it is necessary to consider its viscoelastic properties, which are similar to those of viscoelastic materials. The modified model, therefore, incorporates viscous and elastic forces resulting from tissue deflection. It is essential to note that static and Coulomb friction forces are independent of contact area and velocity, according to Amontons Second Law and Coulomb Law of Friction [91].

In this paragraph, the viscoelastic forces shown in the model are explained regarding when and how they act between the needle and tissue interface. After a needle punctures tissue and enters it, the tissue deflects, creating a temporary conical indentation. This deflection is mimicked by the spring damper in the model, as shown in Figure 2.11. The spring-damper forces have two components, a vertical component that impacts the insertion force and a horizontal component that affects the Coulomb friction force. The vertical components of spring-damper forces are in the same direction as the friction force and therefore are added directly to the friction force in Equation 7. The horizontal component of spring-damper forces affects only the Coulomb friction force, and thus only the Coulomb friction force is included in Equation 1.

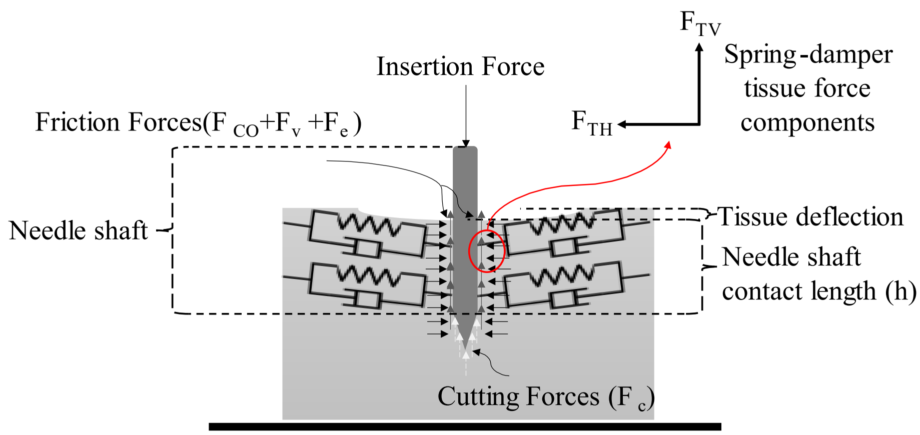

Figure 2.11 Tissue after needle insertion and deflection: Force distribution with spring damper model (Kelvin-Voigt).

The friction force model is written as follows:

$$F_f(h,V) = \begin{cases} F_{St}(h,V) & 0 \leq V \leq 0.002\, m/s \\ F_{CO}(h), F_v(h,V), F_e(h) & 0.002\, m/s \leq V \leq V_{max} \end{cases} \tag{1}$$

The friction forces acting on the needle-tissue interface are described with detail in Figure 2.11. The total friction force, F_f, is the sum of the static friction force, F_{St}, the Coulomb friction force, F_{CO}, the viscous force, F_v, and the elastic force, F_e. The needle insertion depth and velocity are represented by *h* and *V*, respectively.

In the study of friction forces involving needles, there are specific observations concerning static friction force, symbolized as F_{St}. This force is evident when the needle velocity falls between 0 and ± 0.002 m/s. For the purposes of creating a friction force model in this research, the velocity was expanded to a range of 0 to ± 0.005 m/s. Static friction reached its maximum at a velocity close to ± 0.002 m/s, as illustrated in Figures 3.5 and 3.6. Given this finding, velocities within the range of 0 to ± 0.002 m/s were excluded from the calculations for the Coulomb friction force (F_{CO}), vertical viscous force (F_v), and vertical elastic force (F_e). This exclusion is a result of the lack of relative movement between the needle and the tissue within this specific velocity range, a condition attributable to static friction. Once the needle begins to slide in relation to the tissue, dynamic friction forces, including Coulomb friction (F_{CO}), viscous (F_v), and elastic (F_e) forces, become relevant. In this context, these forces are considered as components of dynamic friction.

To sum up, this section presents a modified friction force model that takes into account static and dynamic friction, as well as tissue viscoelastic forces. It extends the widely used Karnopp model to include the viscoelastic properties of tissue. The model has various applications in fields such as haptic displays and robotics and is crucial for understanding the behavior of sliding bodies (needle and tissue) in contact with each other. This work emphasizes the importance of considering both static and dynamic friction forces and tissue deflection when modeling the friction force acting between the needle and tissue. The cutting force model, which is a part of the insertion force model, is explained in detail in the subsequent paragraphs.

2.2.2 Cutting Force Modeling

In this paragraph, the concept of the cutting force model, where the cutting force is a linear function of velocity, is explained in detail. The cutting force is the force required to pierce the tissue using a needle tip. Under ideal conditions, the cutting force remains constant throughout the insertion process, assuming that the insertion velocity and tissue properties (i.e. stiffness) remain constant [21,30]. This is because the contact area of the needle tip with the tissue stays constant, and the cutting angle of the needle can maintain a consistent angle. However, the cutting force may vary due to changes in tissue properties, such as variations in tissue stiffness [3,4,30,46]. Furthermore, if the insertion velocity is altered, the cutting force is also affected. A slower insertion velocity will result in a lower cutting force, while a higher insertion velocity will result in a higher cutting force. It is also important to note that the cutting force is independent of the depth of the insertion. Instead, it is determined by the cutting edge of the needle tip and the tissue properties. The cutting force is a linear function of needle insertion velocity, which is inspired by the research published by Y. Fukushima et al. [70] and M. Heverly et al. [77]. The mathematical expression for the cutting force is demonstrated in Equation 2.

$$F_C = C_c V \tag{2}$$

F_C is the cutting force, and C_c and V are the coefficients of the cutting force and insertion velocity. The cutting force acts in the same vertical direction as the insertion force.

In summary, the presented cutting force model highlights the complexities in accurately predicting the cutting forces required for needle-tissue interactions. Here, understanding the cutting force is crucial for the development of more efficient and effective medical procedures, and the model provided can aid in the design of new medical devices and procedures.

2.2.3 Insertion Force model – Combination of Friction and Cutting Force Models

To gain a complete understanding of the mechanical aspects of needle insertion, the insertion force model integrates the friction force model and the cutting force model, which have been discussed earlier. By combining Equations 1 and 2, the following equation describes the insertion force:

$$F_I = \begin{cases} F_{St}(h, V), & 0 \le V \le 0.002\ m/s \\ F_{CO}(h), F_v(h, V), F_e(h), F_C(h, V) & 0.002\ m/s \le V \le V_{max} \end{cases} \tag{3}$$

Here, F_I is the needle insertion force.

Here, the needle insertion force model F_I is examined using the insertion-extraction experiments. The purpose of this experiment is to determine the force parameters that affect the insertion force, particularly the dynamic forces that occur during the post-puncture phase when the needle is inserted into the tissue. To accomplish this, the least square regression method is utilized. The focus is solely on dynamic forces, including Coulomb friction, viscous, elastic, and cutting force, while the static friction force is ignored [3,30,65,71]. The resulting insertion force equation, excluding the static friction force, can be expressed as follows:

$$F_I = [\,F_{CO} + F_v + F_e]\,h + C_c\,V, \quad 0.002\ m/s \le V \le V_{max} \tag{4}$$

The viscous force is written as Vb, and the elastic force can be represented using kX.

$$F_I = [\ F_{CO} + Vb + kX\ ]\ h + C_c V \tag{5}$$

k and C_c are elastic coefficient and the cutting coefficient, and b and X are the viscous coefficient and tissue deflection vertical distance. Given the specific mass of the needle and the velocities associated with insertion and extraction, the role of acceleration was minimal. The inertia force, which is the result of multiplying the mass by acceleration, was negligible due to the needle low mass, amounting to 8×10^{-3} kg, and a peak acceleration measuring 5.6×10^{-3} m/s^2. Consequently, the maximum inertia force can be calculated as 4.4×10^{-5} N, a value that can be ignored. Furthermore, the peak acceleration, recorded at zero velocity (which coincides with the needle reversing its direction), was found to be 5.6×10^{-3} m/s^2.

2.2.4 Measurement of Friction Force with a Linear Square Regression Method

To quantify the Coulomb friction, viscous, and elastic forces involved in needle insertion and extraction, a sinusoidal experiment was conducted using the least square regression analysis method. The experiment was designed to eliminate the influence of cutting forces, which can often complicate the measurement of these forces. To achieve this, the same experimental setup as used in the previous section was employed, which included a linear actuator, force sensor, needle holder, and tissue holder, as shown in Figure 2.6.

This experimental setup was carefully designed to ensure accurate and precise measurements of the forces involved in needle-tissue interactions. The linear actuator was used to move the needle in a sinusoidal pattern, while the force sensor measured the friction forces acting on the needle shaft during the insertion and extraction phases. In addition, the needle fixture and tissue fixture were designed to keep the needle and tissue in a fixed position during the experiment, eliminating any unwanted movement that could interfere with the measurements. Overall, the use of the specialized experimental setup, along with the least square regression method, enabled accurate and reliable quantification of the different forces involved in needle-tissue interactions, which is critical for understanding the mechanics of needle insertion and developing new medical devices.

The needle was set to move in a sinusoidal pattern with a frequency of 0.02 Hz and an amplitude of 5 mm/s. Needle was inserted through a tissue sample that was 3.5 cm thick while ensuring that the surface area of the tissue in contact with the needle remained constant during the insertion and extraction phases. It is noteworthy that the needle was first inserted through the top end of the tissue, with the tip exposed outside from the bottom, ensuring that only the needle shaft makes contact with the tissue. The recorded velocities during the needle movement were analyzed in two parts, as demonstrated in Figure 2.12. The first part, from position 0 to position 2, indicated positive velocities, whereas the second part, from position 2 to position 4, indicated negative velocities.

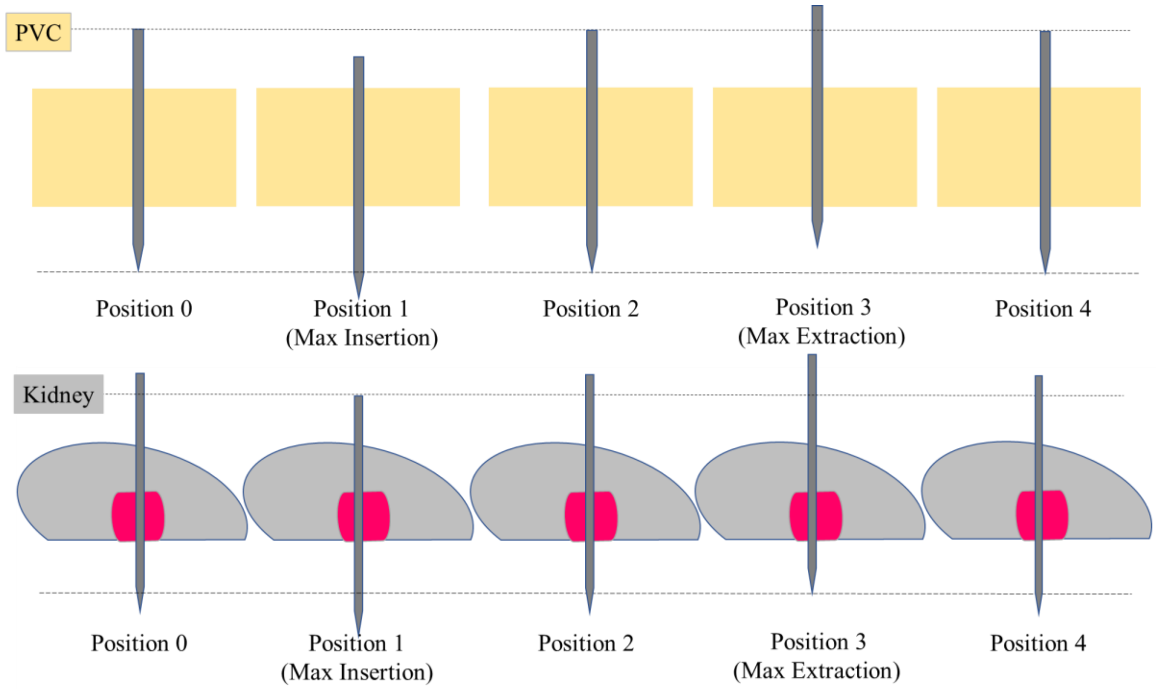

Figure 2.12 Needle positions for sinusoidal insertion and extraction inside PVC tissue and bovine kidney (No tip contact with the tissue).

Equation (6) was derived by simplifying Equation (3) to estimate the force parameters at non-zero velocities.

$$F_{fr} = [F_{COP}\left(\frac{(sgn(V)+1)}{2}\right) + b_P V_P + F_{CON}\left(\frac{(sgn(V)-1)}{2}\right) + b_N V_N + k_P x_P + k_N x_N]h \qquad (6)$$

The variables V_P, b_P, F_{COP}, x_P *and* k_P refer to positive velocities, viscous coefficient, Coulomb friction force, deflection distance, and elastic coefficient, respectively. On the other hand, V_N, b_N, F_{CON}, x_N *and* k_N represent negative velocities, viscous coefficient, normal force, Coulomb friction force, deflection distance, and elastic coefficient, respectively. The measured dynamic friction force during insertion and extraction is denoted by F_{fr}. Equation 6 was expressed in matrix form, and the resulting equation is given by Equation 7.

$$\begin{bmatrix} F_{fr_1} \\ F_{fr_2} \\ \vdots \\ F_{fr_N} \end{bmatrix} = \begin{bmatrix} \frac{(sgn(V_1)+1)}{2} & V_{P1} & \frac{(sgn(V_1)-1)}{2} & V_{N1} & x_{P1} & x_{N1} \\ \frac{(sgn(V_2)+1)}{2} & V_{P2} & \frac{(sgn(V_2)-1)}{2} & V_{N2} & x_{P2} & x_{N2} \\ \vdots & \vdots & \vdots & \vdots & \vdots & \vdots \\ \frac{(sgn(V_N)+1)}{2} & V_{PN} & \frac{(sgn(V_N)-1)}{2} & V_{NN} & x_{PN} & x_{NN} \end{bmatrix} \begin{bmatrix} F_{COP} \\ b_P \\ F_{CON} \\ b_N \\ k_P \\ k_N \end{bmatrix} h \quad (7)$$

$$or$$

$$F_{fr} = A\ B \quad (8)$$

Here,

$$\text{B} = \begin{bmatrix} F_{COP} \\ b_P \\ F_{CON} \\ b_N \\ k_P \\ k_N \end{bmatrix} \quad (9)$$

$$A = \begin{bmatrix} \frac{(sgn(V_1)+1)}{2} & V_{P1} & \frac{(sgn(V_1)-1)}{2} & V_{N1} & x_{P1} & x_{N1} \\ \frac{(sgn(V_2)+1)}{2} & V_{P2} & \frac{(sgn(V_2)-1)}{2} & V_{N2} & x_{P2} & x_{N2} \\ \vdots & \vdots & \vdots & \vdots & \vdots & \vdots \\ \frac{(sgn(V_N)+1)}{2} & V_{PN} & \frac{(sgn(V_N)-1)}{2} & V_{NN} & x_{PN} & x_{NN} \end{bmatrix} h \quad (10)$$

$$B = (A^T A)^{-1}(A)^T F_{fr} \quad (11)$$

Equation 16 represents the least square regression form of B, which was used in the analysis. The parameters obtained from this least square regression analysis are presented in the results and discussion section.

2.2.5 Measurement of Cutting Force for the Cutting Force Model

The experiment aimed to validate the cutting force model by measuring the cutting force exerted by the needle tip during needle insertion inside the tissue. Five insertion tests were conducted using bare and coated needles at varying velocities to achieve this. The cutting force was determined by utilizing the cutting coefficient, which was obtained by attaching a collet to the linear actuator to ensure only the needle tip remained exposed to the tissue. A force sensor was then mounted at the end of the needle to measure the cutting force. The force sensor can only measure the cutting force since the needle shaft was covered with the collet. The experimental setup is illustrated in Figure 2.13.

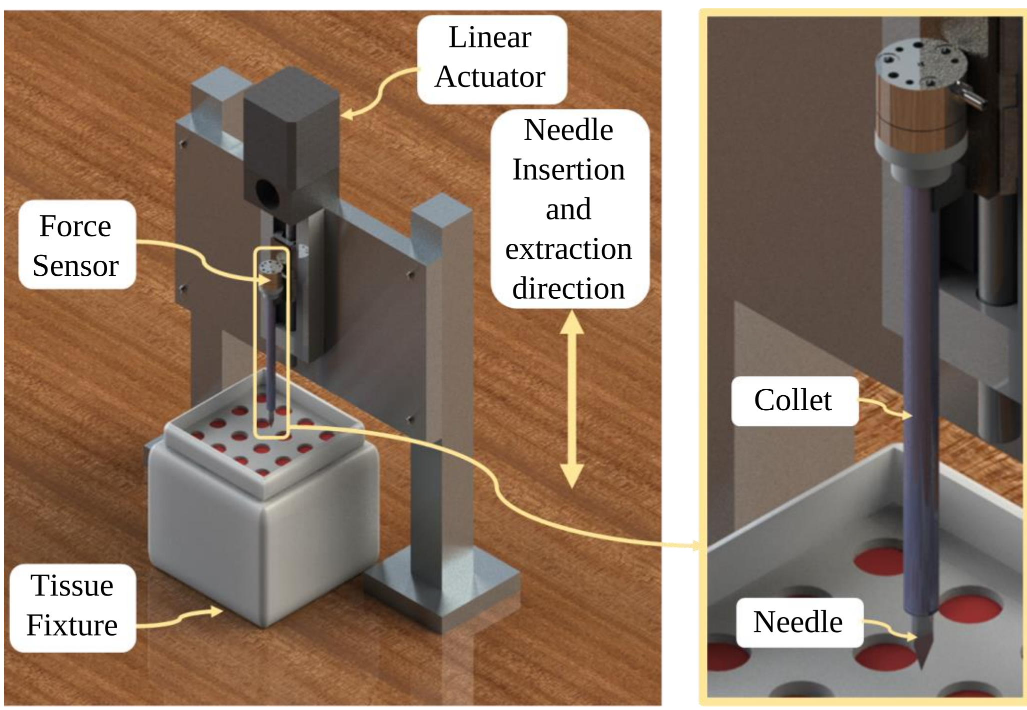

Figure 2.13 Cutting force measurement test setup.

To ensure accuracy, the experiment was conducted at four different insertion speeds ranging from 0.8 mm/s to 1.4 mm/s. It was observed that the collet would crack the tissue faster than the needle tip could cut the tissue when the insertion speed exceeded 1.4 mm/s. As a result, the maximum insertion speed was limited to 1.4 mm/s. Finally, the average cutting force was calculated using Equation 8. This experimental setup provided a reliable method for measuring the cutting force and verifying the model's accuracy.

In Chapter 3, titled "Results and Discussion," a comprehensive analysis of the experiments outlined in Chapter 2 is presented. This chapter incorporates graphs, tables, and statistical analysis to provide a thorough examination and interpretation of the obtained results.

CHAPTER 3

RESULTS AND DISCUSSION

This chapter presents a detailed analysis of the various experiments conducted to investigate the insertion-extraction force measurement, AFM analysis, coefficient of friction measurement, histological analysis, and the experiment conducted to study and verify the insertion force model. The purpose of these experiments was to gain a better understanding of the behavior of the forces and tissue damage with composite needle coating and to validate the proposed model.

The first experiment was the insertion-extraction force measurement, which involved measuring the force required to insert and extract the needle inside the phantom tissue and bovine kidney. The results of this experiments were presented in the form of graphs and tables to show the variation of the force with respect to different parameters such as the insertion force, extraction force, maximum insertion and extraction forces, and the depth of insertion and extraction.

The AFM analysis was also conducted to study the surface properties of the coated and bare needles. The results of this experiment provided a detailed insight into the topography and roughness of the materials. The findings were presented in the form of images and graphs to facilitate a better understanding of the results. In addition, the LFM study was also carried out to measure the friction between the needle surface and the AFM tip.

The histological analysis was performed using the standard paraffin embedding procedure with H&E staining. The results of this experiment provided valuable information about the reduction in tissue damage with the coated needle. The findings were presented in the form of images and table.

Lastly, an experiment was conducted to study and verify the insertion force model proposed in this thesis. In addition, the needle coating affected parameters were analyzed to understand the insertion force reduction mechanics. The results of this experiment were compared with the data obtained from the model, and a good agreement was observed. The findings were presented in the form of graphs and tables to show the comparison between the experimental and predicted values.

3.1 Insertion-Extraction Forces of Coated and Bare Needles

The insertion and extraction of needles are common medical procedures used in various diagnostic and therapeutic applications. To evaluate the performance of coated needles, it is essential to measure the insertion-extraction force required for their operation. In this regard, the present study aimed to conduct insertion-extraction force measurements of coated and bare needles to investigate their comparative performance. The results of this study can provide valuable insights into the performance of coated needles and their potential use in various medical procedures.

In Figure 3.1, the average insertion and extraction forces generated during the insertion of coated and bare needles in the PVC tissue phantom are shown. The upper region of the data displays the insertion force, while the lower region shows the extraction force. The insertion force follows a curvilinear trend because the two-layer PVC tissue phantom has isotropic properties, with two different layers mimicking the bovine kidney. During the extraction phase, the needle tends to stick to the PVC tissue phantom due to its partial adherent property. The pressure of the tissue phantom and the partial adherent property cause the tissue to be dragged in an upward direction with the needle until the adherent bond is broken, resulting in valleys during the extraction process.

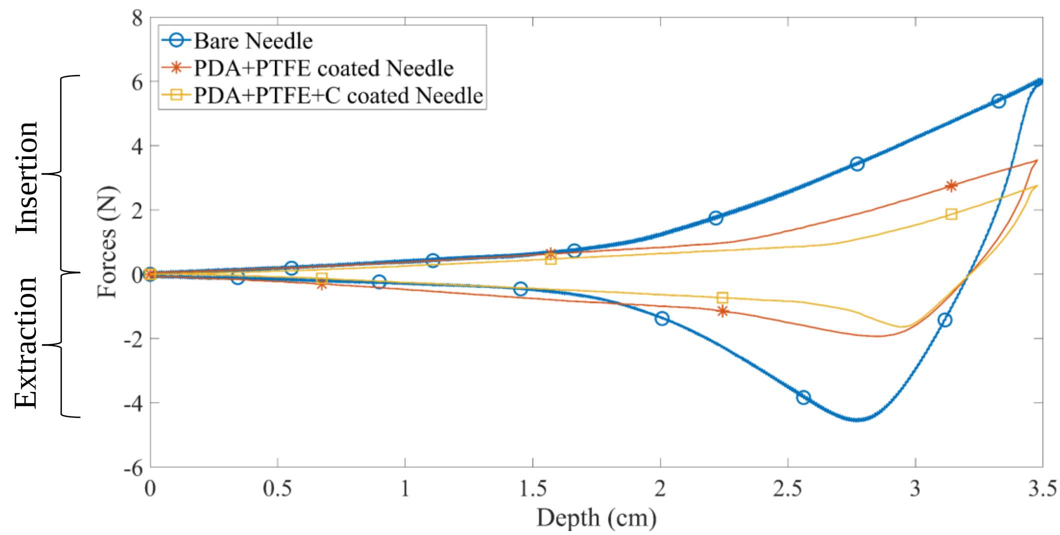

Figure 3.1 Force profiles for bare needle, PDA-PTFE coated needle, and PDA-PTFE-C coated needle in PVC tissue; Standard deviation 0.041N for the bare needle, 0.080N for PDA-PTFE coated needles, and 0.12N for PDA-PTFE-C.

It can be observed from Figure 3.1 that the valleys are located at the absolute maximum point of the average extraction force. The results show that the average insertion and extraction forces for PDA-PTFE-C coated needles are 62% and 64% lower than those of the bare needles. Figure 3.2 shows the average maximum insertion-extraction forces and standard deviations of bare and coated needles in PVC tissue. From Figure 3.2, the results were found to be repeatable, with an average standard deviation of 0.041 for the bare needle, 0.080 for PDA-PTFE coated needles, and 0.12 for PDA-PTFE-C coated needles upon insertion in the PVC tissue phantom.

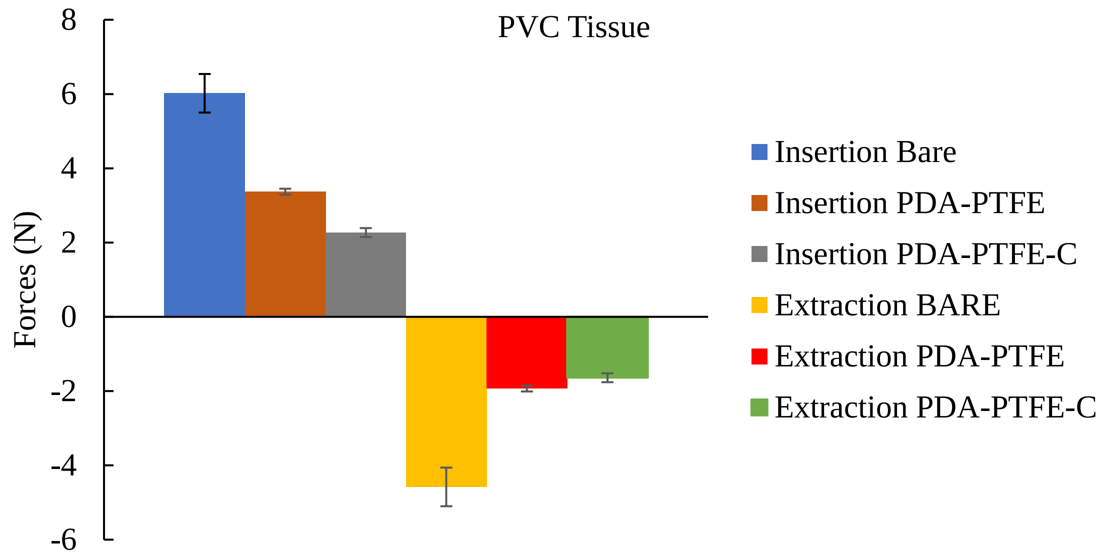

Figure 3.2 Average maximum forces and standard deviations of bare and coated needles in PVC tissue.

Figure 3.3 displays the result of the polymer-coated needle force data versus depth for the experiment conducted using bovine kidney. The forces exhibit a nonlinear trend because the bovine kidney is heterogeneous, with tissue layers such as the cortex, medulla, and non-homogeneous fiber distribution. The average insertion and extraction forces for PDA-PTFE-C coated needles were found to be approximately 49% and 30% lower than those of the bare needles, respectively. Furthermore, the average insertion and extraction forces for the PDA-PTFE-C needles were lower than those of the other coated needles. In addition, Figure 3.3 also shows valley at the maximum extraction forces of each needle extraction forces.

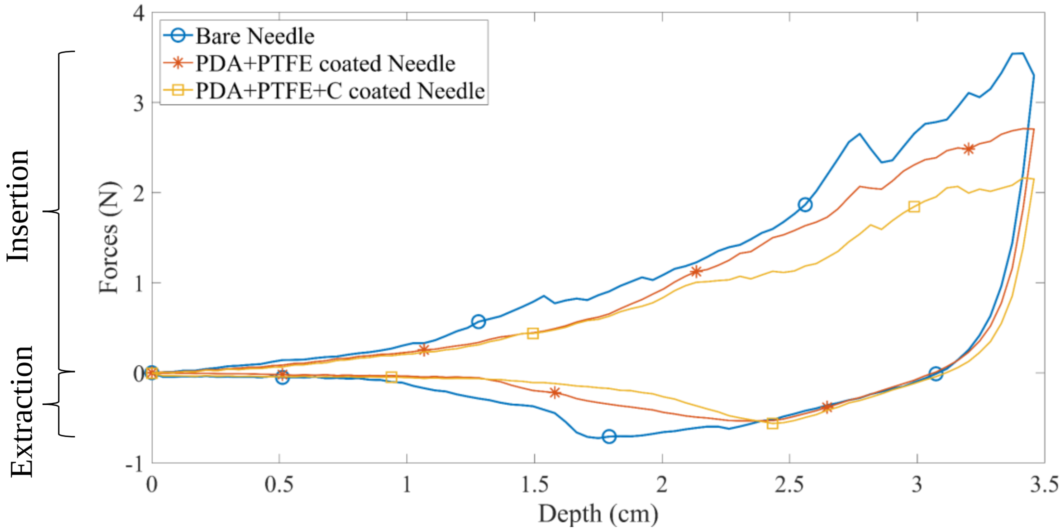

Figure 3.3 Force profiles for bare needle, PDA-PTFE coated needle, and PDA-PTFE-C coated needle in bovine kidney; average maximum forces standard deviation for the bare needle is 0.052N, for PDA-PTFE coated needle is 0.048N, and for PDA-PTFE-C coated needle is 0.023N.

The reproducibility of the results can be inferred from the low average standard deviations obtained during the experiment. Figure 3.4 shows the average maximum insertion-extraction forces and standard deviations of bare and coated needles in bovine kidney. The average standard deviation for the bare needle is 0.052, for PDA-PTFE coated needle, it is 0.048, and for PDA-PTFE-C coated needle is 0.023 during the insertion in the bovine kidney depicted with a column bar chart. The p-values for each maximum insertion and extraction force of the bare and coated needle comparison are less than $\alpha = 0.05$, which proves that each dataset has a significant difference between them.

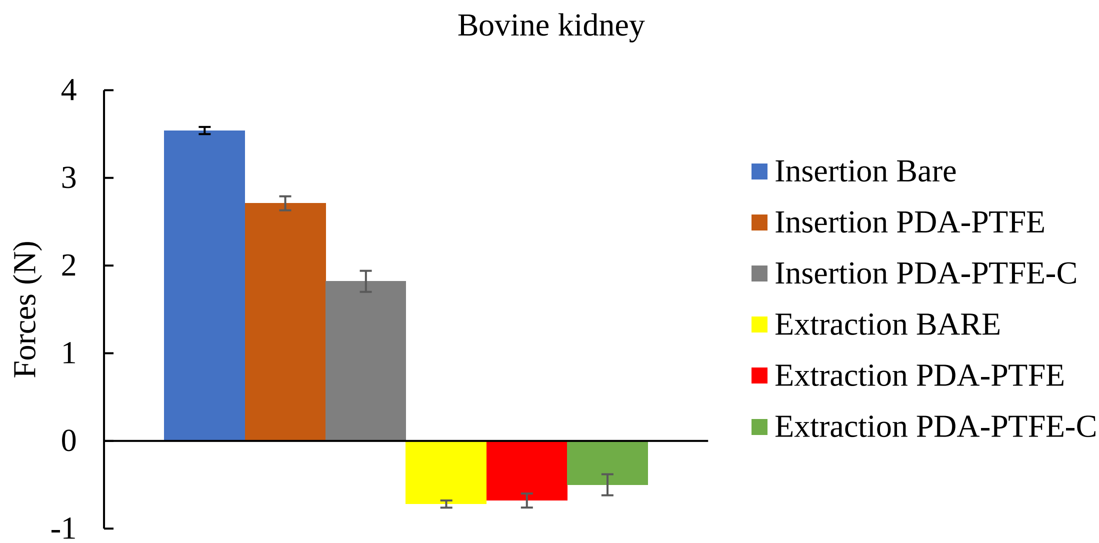

Figure 3.4 Average maximum forces and standard deviations of bare and coated needles in the bovine kidney.

The results presented in Figure 3.1 and Figure 3.3 are significant as they highlight the effectiveness of PDA-PTFE-C coated needles in reducing the insertion and extraction forces required during medical procedures. This is particularly important as tissue damage and patient discomfort are often associated with high insertion and extraction forces. The results also demonstrate that the partial adherent property of the PVC tissue phantom affects the insertion and extraction forces during the needle insertion process. The repeatable results obtained from this study, as indicated by the low standard deviation values, further support the effectiveness of PDA-PTFE-C coated needles in reducing insertion and extraction forces. The findings from this study have important implications for the development of medical devices, as they suggest that the use of coated needles can reduce tissue damage and patient discomfort during medical procedures. The observation of valleys in Figures 3.1 and 3.3 is noteworthy, as it suggests temporary adhesion of the needle to the tissue due to the needle's stickiness [19,60]. The valley becomes visible during the extraction phase because the needle achieves maximum contact length with the tissue before it is extracted. Conversely, during insertion, the needle's contact surface length with the tissue progressively increases, preventing the formation of a discernible valley. The valley observed in the PDA-PTFE-C coated needle during extraction is smaller than that in the bare needle, suggesting that the coating lessens the temporary adhesion of the needle to the tissue, effectively reducing its stickiness.

As the needle penetrated deeper into the tissue, the contact area between them grew, causing friction to steadily overshadow the cutting force. Consequently, at the maximum depth of 3.5 cm, the cutting force was minimal in comparison to the friction force. The cutting force magnitude is influenced by the needle geometry, staying constant during the insertion in isotropic tissues, but showing slight variations in heterogeneous tissues.

Although making a direct comparison between PDA-PTFE and C coating with other coatings like DLC [18] and TFMG [92] may not be entirely fair due to the use of different needle types and tissues in their studies. But if the reduction percentage is considered of insertion force, the DLC-coated needle demonstrated a 30% reduction in insertion force in pig eyes, while the TFMG-coated needle showed a 47% reduction in insertion force in pork muscle. In our studies involving bovine kidneys, the insertion force reduction was 49%, which surpasses the reduction achieved by both DLC and TFMG-coated needles in biological tissue.

Overall, the results of the experiment clearly indicate that the use of coated needles results in significantly lower insertion and extraction forces as compared to bare needles. The coated needles were found to have an average reduction of 49% and 30% in insertion and extraction forces, respectively, in bovine kidneys. These findings are of significant importance as they have important implications for reducing tissue damage and pain during needle insertion procedures. Additionally, the use of coated needles is also expected to reduce healing time after surgical procedures. Overall, the experiment provides evidence that the use of coated needles could be a promising approach to improve patient comfort and outcomes during needle-based medical interventions.

3.2 AFM Analysis Findings

The surface roughness of needles is essential for the effectiveness and safety of needle insertion procedures. Various coatings have been developed to reduce tissue damage and pain during needle insertion. Among these coatings, PDA-PTFE-C has shown promising results. However, the effect of this coating on the surface roughness of needles has not been studied extensively. In this context, Atomic Force Microscopy (AFM) has been used to analyze the surface roughness of PDA-PTFE-C coated and bare needles. The results of the AFM analysis show that the surface roughness of the PDA-PTFE-C coated needle is lower than that of the bare needle, as indicated by the root mean square (RMS) values. Furthermore, the AFM images show that the surface profile of the coated needle is different from that of the bare needle. This information is crucial for understanding the behavior of the coated needle during insertion and extraction and for optimizing the design of the coating to minimize tissue damage and pain.

The analysis results revealed that the root mean square (RMS) value of the surface roughness for the PDA-PTFE-C coated needle was approximately 94.00 nm, while it was 218.12 nm for the bare needle. Furthermore, the AFM images of the bare needle and the-PDA-PTFE coated needle showed a random surface texture profile, as presented in Figures 3.5 (a) and 3.5 (b). On the other hand, the PDA-PTFE-C coated needle exhibited a unidirectional surface profile with some waviness in it, as shown in Figure 3.5 (c). These findings provide insight into the surface characteristics of the needles and suggest that the surface roughness of a needle can be significantly improved by coating it with PDA-PTFE-C, which may help in reducing tissue damage and pain during needle insertion procedures.

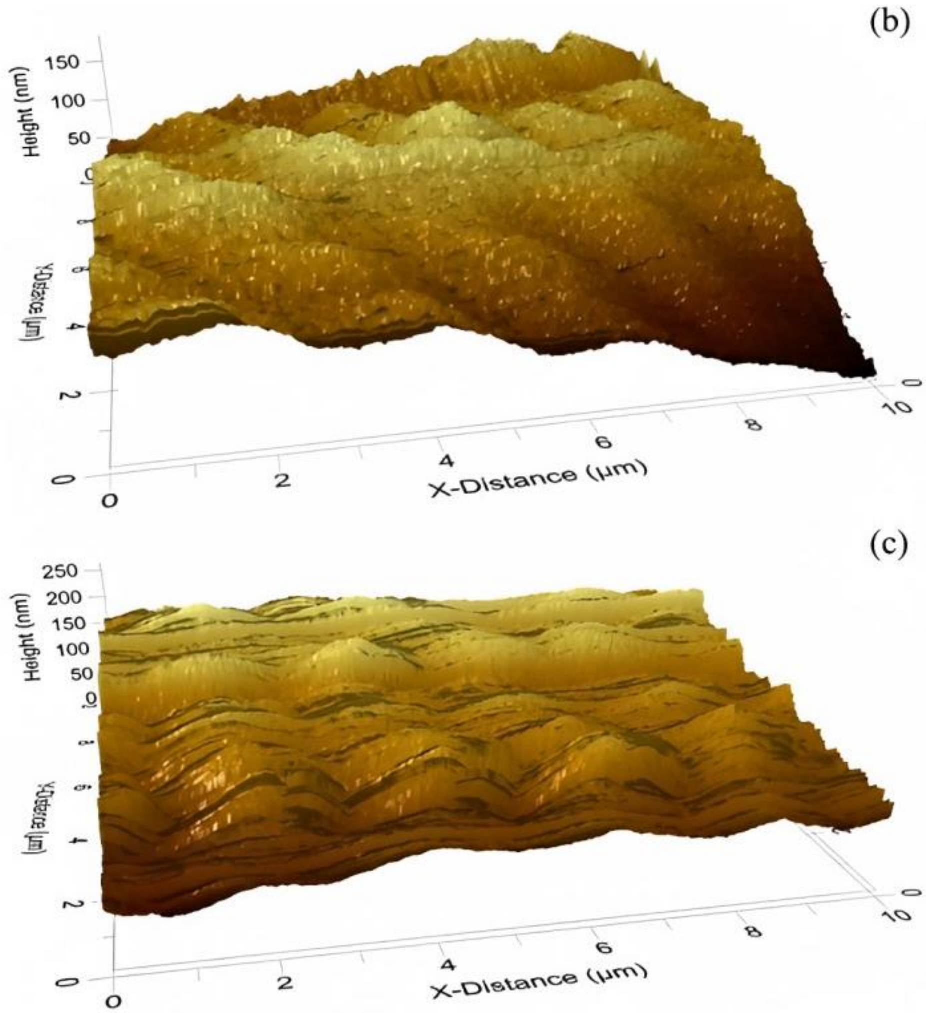

Figure 3.5 (a) AFM topography of bare needle **(b)** AFM topography of PDA-PTFE coated needle **(c)** AFM topography of PDA-PTFE-C coated needle.

To determine the effect of the coating on the friction force between the needle surface and the AFM probe tip, the LFM technique was used to measure the friction force between the AFM tip and needles. The scan angle and area were set at 90° and 30 micros, respectively, and the friction force image profiles were obtained by subtracting the trace scan image from the retrace scan images. The obtained LFM friction profile and line profile of the needles are presented in Figure 3.6.

The results showed that the maximum average friction force between the needle and AFM tip of the PDA-PTFE-C coated needle was 23.9 nN, whereas the bare needle friction force was 69.7 nN. These results indicate a significant reduction in the friction force between the needle surface and the AFM probe tip due to the PDA-PTFE-C coating. The surface roughness values and the friction force between the needle surface and the AFM tip for both the bare and coated needles are presented in Table 3.1. It is evident that the maximum friction force of the PDA-PTFE-C coated needle was decreased by 65.7% compared to the bare needle. These findings suggest that the PDA-PTFE-C coating can reduce the friction force between the needle and tissue interface during insertion and extraction, which can minimize tissue damage and pain and ultimately lead to improved healing outcomes.

In the preceding section, it was established that the average insertion and extraction forces decreased in PDA-PTFE-C coated needles compared to bare needles and PDA-PTFE coated needles. The friction force was identified as the primary contributor to insertion and extraction forces. However, it was challenging to measure the friction force on the needle and tissue interface using existing sensor technologies. Therefore, AFM was utilized to investigate the coating effect on the friction force between the needle surface and the AFM probe tip. It is reasonable to assume that if the friction force is reduced as in this case, it should also be reduced when the needle is inserted into tissues. The friction force measured with the AFM test for the PDA-PTFE-C coated needle was 65.7% lower than those of the bare and PDA-PTFE coated needles.

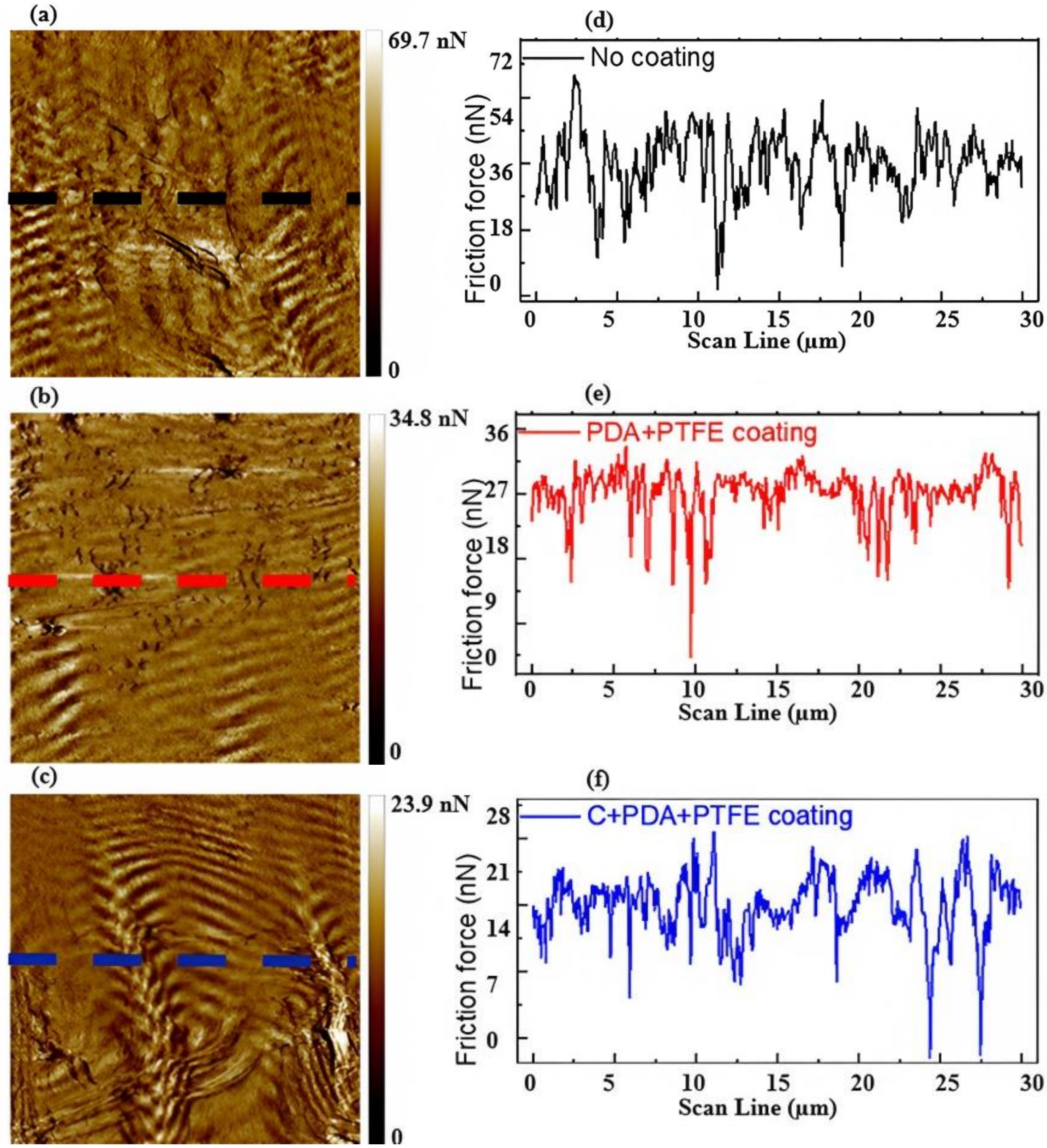

Figure 3.6 LFM friction profile of **(a)** bare needle **(b)** PDA-PTFE coated needle **(c)** PDA-PTFE-C coated needle; Cross-sectional friction line profile of **(d)** the bare needle **(e)** PDA-PTFE coated needle **(f)** PDA-PTFE-C coated needle. Scan size: 30μm×30 μm.

Table 3.1 reveals that the PDA-PTFE-C coated needles had lower surface roughness RMS, and lower friction than the bare needle. The PDA-PTFE-C coating demonstrated significant reductions in the insertion and extraction forces due to PTFE non-stick properties, activated carbon filler and PTFE self-lubrication properties, and unidirectional surface texture. Therefore, the results of the AFM analysis support the conclusion that the coated needles have lower friction forces, making them more suitable for medical procedures requiring needle insertion, reducing tissue damage and pain, and improving recovery times.

Table 3.1 Surface roughness RMS (nm) and friction force between AFM tip and needles recorded by the AFM.

	Surface roughness RMS (nm)	**Maximum average friction force (nN)**
Bare	218.12	69.7
PDA- PTFE	160.48	34.8
PDA- PTFE-C	94.0	23.9

3.3 Tissue Damage Study

This section delves into the outcomes of a histological analysis that examined the damage caused by coated and bare needles in bovine kidney tissue. The research involved examining two bovine kidney tissue samples that were stained with H&E and examined under an Olympus GX-71 microscope with 5X to 10X magnification. The microscope was accurately calibrated using a micrometer calibration slide to ensure precise measurements. Figure 3.8 and Figure 3.9 show the damaged area caused by both needles for twelve tissue samples of two bovine kidneys. From the microscopic images of Figure 3.8 and Figure 3.9, it was clear that the tissues underwent damage in the region of needle insertion. These images showcased an evident white region, visually indicating the extent of tissue damage resulting from needle insertion and extraction. A difference was observed when comparing the damage caused by bare and coated needles. Due to their higher exerted force, the bare needles inflicted a larger damaged area than the coated needles. Notably, the tissue damage incurred by the coated needle was considerably less than that of the bare needle.

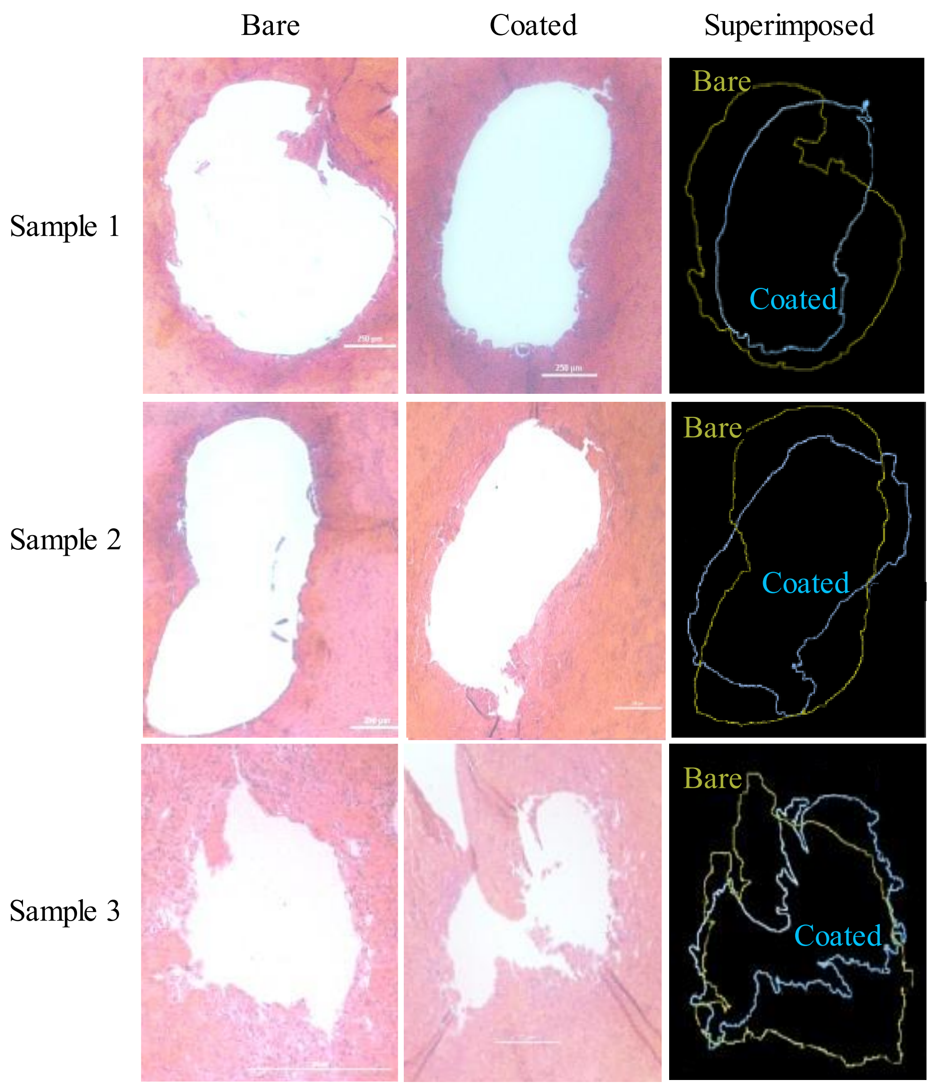

Figure 3.7 Microscopic images of damaged tissue area of bare and coated needle for bovine kidney tissue A.

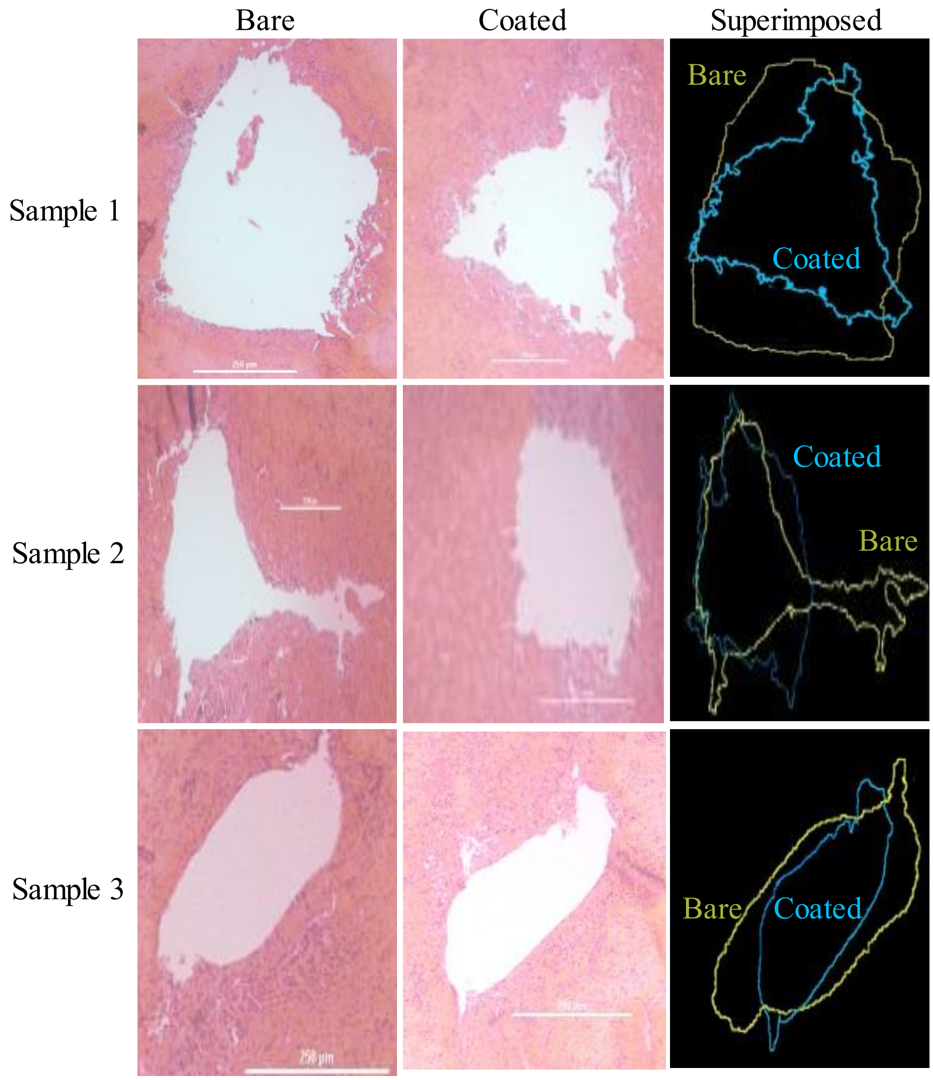

Figure 3.8 Microscopic images of damaged tissue area of bare and coated needle for bovine kidney tissue B.

The insertion hole area was analyzed using the ImageJ software to compare the extent of tissue damage caused by the coated and bare needles. First, the images were converted to grayscale (8-bit) and calibrated with a reference line of 250 μm to make selecting the insertion hole area easier. Then, using the wand tool, the irregular insertion hole was selected to measure the area. The results of tissue damage are shown in Table 3.2, and the average damaged tissue area and its standard deviation are shown in Figure 3.7.

Table 3.2 Damaged area of tissue samples with the standard deviation.

Samples		Damaged Area (mm^2)	
		Bare Needle	**Coated Needle**
	Sample 1	1.051	0.674
Kidney A	**Sample 2**	0.972	0.615
	Sample 3	0.844	0.448
	Sample 1	0.288	0.217
Kidney B	**Sample 2**	0.176	0.079
	Sample 3	0.139	0.069

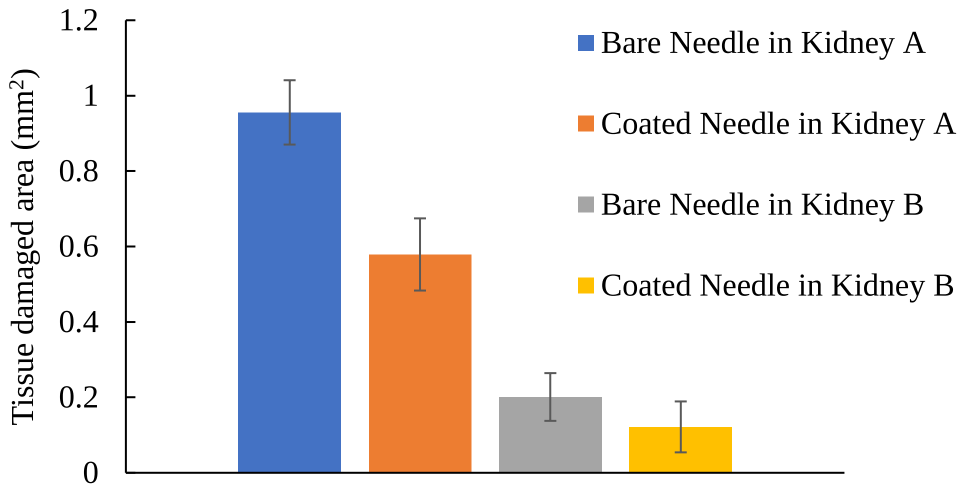

Figure 3.9 Average Damaged area with standard deviations for kidneys A and B.

Table 3.2 and Figure 3.7 show the tissue-damaged area for each sample separately and an average of it with the standard deviation. The average damaged area in Tissue A caused by the bare needle was 0.956 ± 0.085 mm^2, whereas the coated needle caused an average damaged area of 0.579 ± 0.095 mm^2. In Tissue B, the average damaged area caused by the bare needle was 0.201 ± 0.063 mm^2, while the coated needle caused an average damaged area of 0.121 ± 0.067 mm^2. These data satisfy the null hypothesis ($\alpha < 0.05$) of the two-tailed t-test, which shows the statistical significance of the data. According to the study results, the coated needle reduces average tissue damage by 39% compared to the bare needle, indicating that the PDA-PTFE-C coated needle is less destructive during both the insertion and extraction stages. The outcomes of this investigation strongly suggest that the use of coated needles can significantly reduce tissue damage during medical procedures, which could result in faster healing. The application of this coating is not limited to needles; it could also enhance the surfaces of other medical devices. Therefore, the adoption of coated needles represents a fundamental approach to promoting optimal patient outcomes and minimizing potential harm associated with medical interventions.

3.4 Modeled Insertion Force and Experimental Insertion Force

Inserting needles into soft tissues is a common medical practice that is used in many areas of medical interventions, such as brachytherapy, biopsy, and drug delivery. It is important to understand the forces that are exerted between the needle and the tissue during insertion to create safer and more effective medical devices and procedures. This understanding helps to improve patient outcomes and minimize complications during needle insertion.

The findings of the friction force model provide important information about the forces that impact the needle as it passes through tissue. By examining the sinusoidal insertion and extraction force data through the least square regression method the Coulomb friction, elastic, and viscous forces were calculated. Coulomb friction is a force that resists the movement of the needle through the tissue, while elastic and viscous forces arise from the tissue deformation during insertion. This knowledge is critical in creating needles that can penetrate the tissue more effectively and reduce patient discomfort during medical procedures. The combination of the friction force model and the cutting force model in the insertion force model provides a comprehensive understanding of the forces that occur during needle insertion. Comparing the experimental insertion force data with the predictions of the insertion force model can help us assess the model accuracy and improve its predictive capabilities if necessary. In summary, this study results shed light on the forces involved in needle insertion into soft tissues. These insights can be utilized to design and enhance medical devices and procedures to improve patient outcomes and minimize the risk of complications during needle insertion [89].

3.4.1 Coating Effect on Needle Friction Force

The present results display the forces recorded by a force sensor during the insertion-extraction experiments of coated and bare needles in PVC gel tissue with sinusoidal insertion-extractions velocities. The data obtained after the peak force was processed through the least square regression method to estimate the Coulomb friction, viscous, and elastic forces. As evident from Figure 3.10, the static friction force observed for coated and bare needles inside PVC gel tissue at a 3.5 cm insertion length is 2.75 N and 3.28 N, respectively. A t-test was conducted between the bare and coated needles, specifically comparing the forces measured between needle sliding (after the peak force) and before the needle changes its direction. The two-tailed t-test with unequal variance revealed that for the forces measured during insertion, the p-value is 1.36×10^{-5}, while for the forces measured during extraction, the p-value is 9.31×10^{-7}. These p-values, which are less than 0.05, indicate a statistically significant difference between the forces of the bare and coated needles.

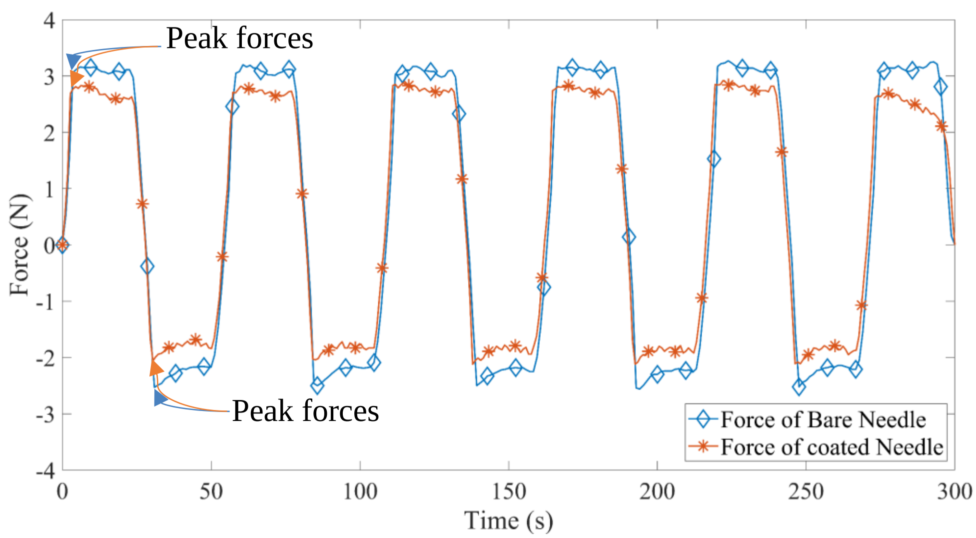

Figure 3.10 Measured friction forces for insertion-extraction for bare needle and coated needles inside PVC gel tissue; the standard deviation of bare needle insertion-extraction force ranges from 0.0057N to 0.018N, and the standard deviation of coated needle insertion-extraction force ranges from 0.0062N to 0.055N.

In Table 3.3, the least square regression method results for the coated and bare needles inside the PVC gel are presented. It is important to note that each force parameter in Table

3.3 is expressed per unit length. Therefore, in order to determine the Coulomb friction for a specific insertion length, the Coulomb friction value must be multiplied by the desired length. Likewise, the viscous coefficient should be multiplied by the insertion length and velocity, and the elastic coefficient should be multiplied by the insertion length and tissue deflection vertical length. The force parameters for the coated needle are lower than those for the bare needle due to the presence of the low-friction coating of PDA-PTDE and C.

Table 3.3 Insertion force parameters for coated and bare needles inside PVC tissue.

Parameters	Coated Needle	Bare Needle
Coulomb friction force (F_{COP})	43.63 N/m	50.34 N/m
Viscous Coefficient (b_P)	363.27 Ns/m^2	423.82 Ns/m^2
Elastic Coefficient (k_p)	5784.00 N/m^2	6748.90 N/m^2

The forces recorded during the insertion-extraction experiments of the coated and bare needle inside the bovine kidney are illustrated in Figure 3.11. The peaks observed in the figure signify the static friction for the respective insertion and extraction cycles, with a needle contact length of 3.5 cm. It can be observed from Figure 3.11 that the static friction force for the coated and bare needle inside the bovine kidney at a 3.5 cm insertion length is 3.1 N and 3.9 N, respectively.

An analysis using a t-test was performed to compare the forces measured between needle sliding (after the peak force) and before the needle changes its direction for both the bare and coated needles. Upon conducting a two-tailed t-test with unequal variance, it was found that the p-value for the forces measured during insertion is 7.04×10^{-6} and for the forces measured during extraction, the p-value is 1.70×10^{-2}. The p-value for extraction is smaller than 0.05, indicating statistical significance. However, compared to the previous value of PVC, it is relatively larger, suggesting that the significant difference in forces measured during extraction between the bare and coated needles is relatively smaller.

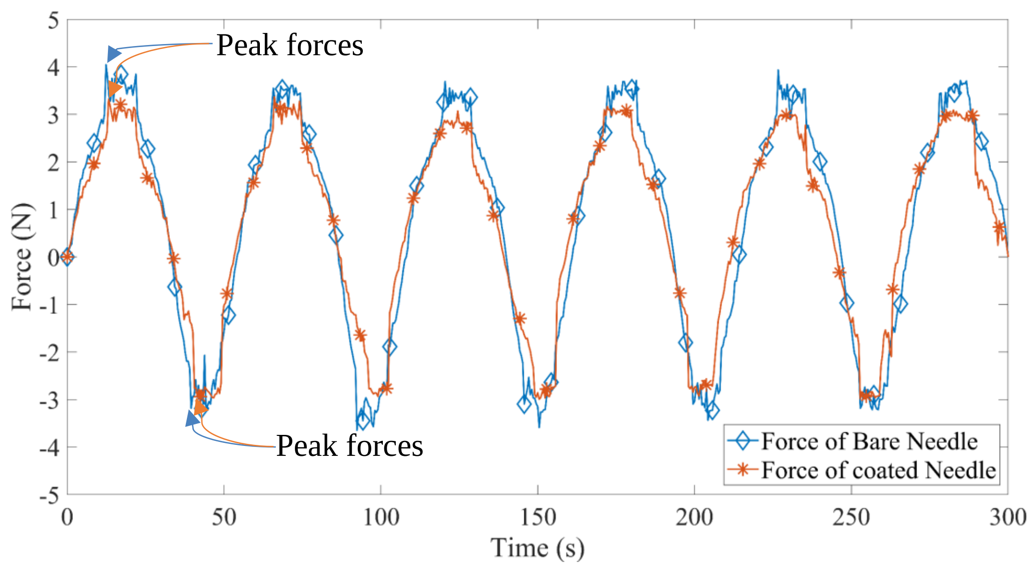

Figure 3.11 Measured friction force for insertion-extraction for bare needle and Coated needles inside bovine kidney; the standard deviation of bare needle insertion-extraction force ranges from 0.0097N to 0.094N, and the standard deviation of coated needle insertion-extraction force ranges from 0.0082N to 0.088N.

The least square regression curve-fitting method was used to calculate the viscous, Coulomb, and elastic forces of the coated and bare needle inside the bovine kidney, with the results summarized in Table 3.4. As with Table 3.3, the force parameters in Table 3.4 are per unit length, which means that the Coulomb friction value must be multiplied by the desired length to obtain the force at a specific insertion length. Similarly, the viscous coefficient must be multiplied by the insertion length and velocity, and the elastic coefficient must be multiplied by the insertion length and tissue deflection vertical length. Comparing the results for the coated and bare needle in Table 3.4, it can be seen that the force parameters for the coated needle are lower than those for the bare needle, which is consistent with the results obtained in PVC gel tissue.

Table 3.4 Insertion force parameters for coated and bare needles inside a bovine kidney.

Parameters	Coated Needle	Bare Needle
Coulomb friction force (F_{COP})	22.86 N/m	27.49 N/m
Viscous Coefficient (b_P)	968.64 Ns/m^2	1105.68 Ns/m^2
Elastic Coefficient (k_p)	8969.36 N/m^2	6416.74 N/m^2

3.4.2 Cutting Force for Various Insertion Speeds.

A cutting force measurement experiment was conducted to determine the cutting coefficient, which, in combination with Equation 2, facilitates the calculation of cutting force at a desired speed for a fixed needle and tissue. The average cutting force data obtained from the experiment, depicted in Figure 3.7, were used to calculate the cutting coefficient for tissue. A simplified form of Equation 2, expressed as Equation 12, was used for the computation of the cutting coefficient.

$$C_c = \frac{F_c}{V} \tag{12}$$

The obtained average cutting force data, shown in Figure 3.12, were used to calculate the tissue constant cutting coefficient using a simplified version of Equation 2, represented in Equation 12. The results of the cutting force experiment inside PVC gel tissue at various velocities are presented in Figure 3.12. The initial data during the tissue deflection phase were excluded from the calculation, and data after 20mm insertion depth were used to find the average cutting forces. The results of the cutting coefficient for PVC gel tissue are summarized in Table 3.5. In addition, the average cutting forces and standard deviations are shown in Figure 3.13.

The cutting coefficient was calculated using the average cutting force, insertion velocities, and Equation 12. The calculated cutting coefficient for PVC gel tissue was found to be 300.36 Ns/m with a standard deviation error of 3.1%.

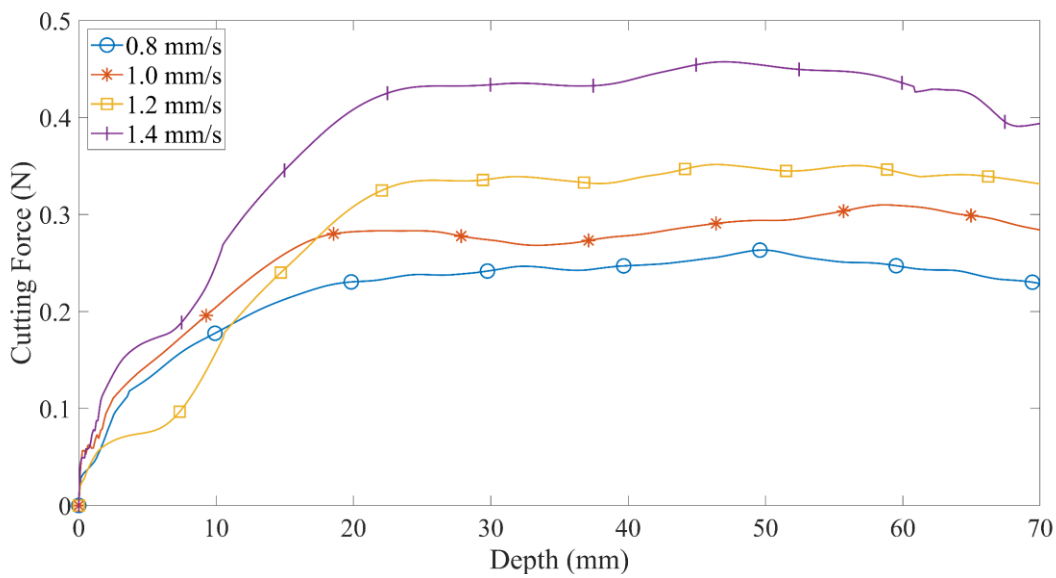

Figure 3.12 Cutting force vs. insertion depth graph inside PVC gel tissue; The standard deviation range of cutting force for 0.8 mm/s velocity 0.0068 mm/s $\leq S0.8 \leq$ 0.0277 mm/s, 1.0 mm/s velocity 0.0051 mm/s $\leq S1.0 \leq$ 0.0210 mm/s, 1.2 mm/s velocity 0.0427 mm/s $\leq S1.2 \leq$ 0.01806 mm/s, and 1.4 mm/s velocity 0.00722 mm/s $\leq S1.4 \leq$ 0.0679 mm/s.

Table 3.5 The average cutting forces and cutting coefficients for PVC tissue.

Velocities (mm/s)	Average Cutting Forces (N)	Cutting Coefficient (Ns/m)
0.8	0.25	312.50
1.0	0.29	290.20
1.2	0.35	291.66
1.4	0.43	307.14

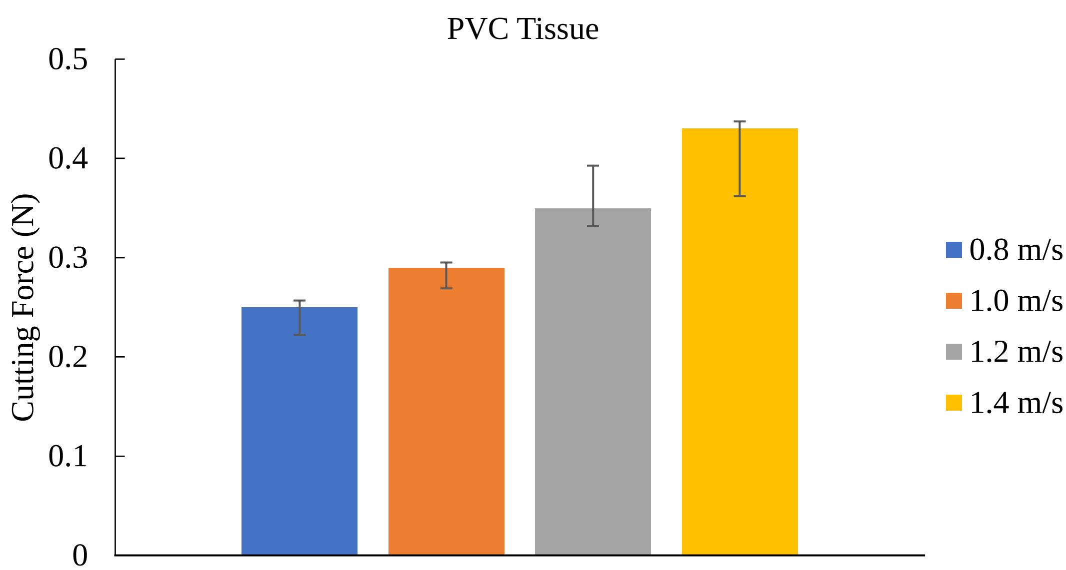

Figure 3.13 The average cutting forces and standard deviations for PVC tissue.

Similarly, four different insertion velocities were used to calculate the cutting coefficient inside the bovine kidney, as depicted in Figure 3.14. The obtained data were used to determine the cutting coefficient using Equation 12. Subsequently, the calculated cutting coefficient was utilized to compute the cutting force for the desired velocities using

Equation 2. The data acquired during the tissue deflection phase, i.e., before 10 mm insertion depth, were excluded from the calculation. Here, the average cutting force and standard deviations for various velocity inside the bovine kidney is shown in figure 3.15.

The cutting force measurement experiment yielded data for calculating the cutting coefficient inside the bovine kidney, which is presented in Table 3.6. From Table 3.6, the first two columns of data, average cutting force and velocities, and Equation 12 were used to calculate the cutting coefficient. The average cutting force and insertion velocities were used along with Equation 12 to calculate the cutting coefficient. Data after 10mm insertion depth were considered for the calculation, as data before 10mm were obtained during the tissue deflection phase. The calculated cutting coefficient, with a standard deviation error of 3.2%, was found to be 208.15 Ns/m, as indicated in column 4 of Table 3.6.

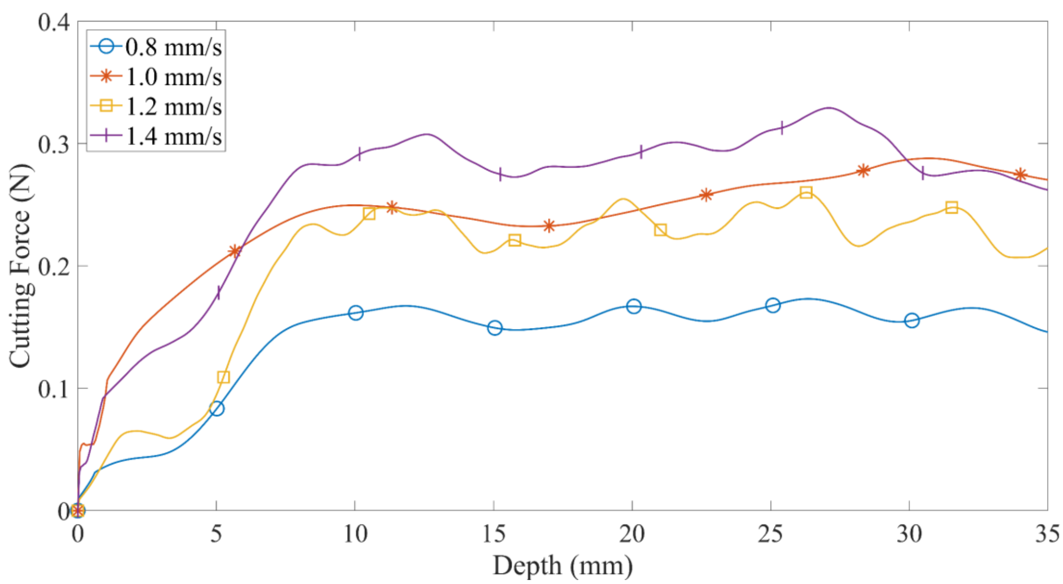

Figure 3.14 Cutting force vs. insertion depth graph inside bovine kidney; The standard deviation range of cutting force for 0.8 mm/s velocity 0.0089 mm/s≤S0.8≤ 0.0653 mm/s, 1.0 mm/s velocity 0.0129 mm/s ≤S1.0≤ 0.0764 mm/s, 1.2 mm/s velocity 0.0271 mm/s ≤S1.2≤ 0.0375 mm/s, and 1.4 mm/s velocity 0.0099 mm/s ≤S1.4≤ 0.0415 mm/s.

From figures 3.12 and 3.14, the cutting force increases without any initial spike at the tissue puncture, and it does not have any force reduction after the puncture. This phenomenon can be understood physically because the needle is very small, with a diameter of 1.27 mm, and has a sharp trocar tip, allowing it to cut through the tissue effortlessly. In addition, the PVC gel tissue and bovine kidney top layer are not covered with the thick skin found in many tissues. So, the stress release at penetration is more noticeable with bigger diameter needles and thicker top layer tissues.

Table 3.6 The average cutting forces and cutting coefficients for a bovine kidney.

Velocities (mm/s)	Average Cutting Forces (N)	Cutting Coefficient (Ns/m)
0.8	0.17	212.25
1.0	0.20	200.00
1.2	0.25	208.33
1.4	0.30	214.28

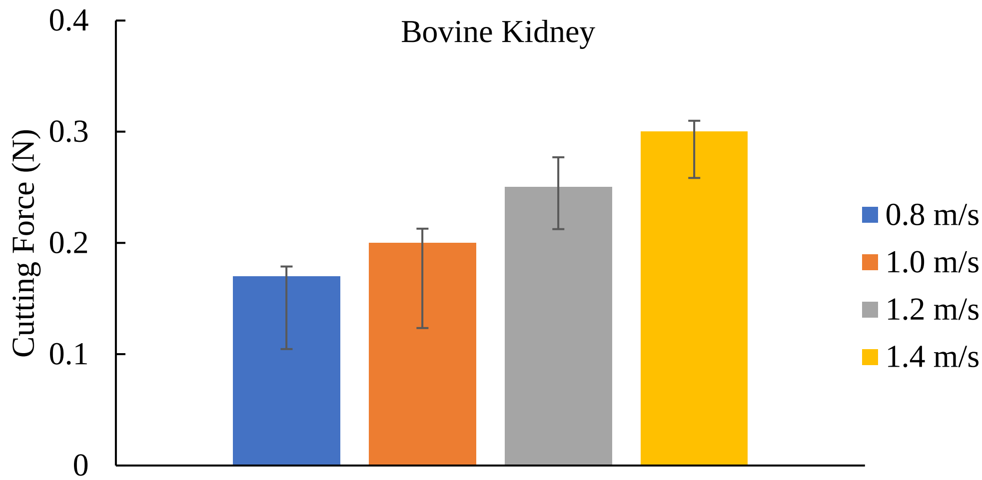

Figure 3.15 The average cutting forces with standard deviations for bovine kidney.

3.4.3 Insertion Force Comparison of Model and Experimental Data

The establishment of the insertion force model involved combining data from previous sections with previous equations. Figure 3.16 displays the force versus insertion depth graph of the insertion force model and experimental insertion force for coated and bare needles inside PVC gel. The coated needle model and experimental insertion force data were very similar. The insertion force model had a linear force trend that changed with insertion depth. It is worth noting that the post-puncture forces only began after the needle effectively punctured the tissue and the entire needle came into contact with the tissue at a 10mm insertion depth. The bare needle model and experimental insertion forces had some errors due to minor needle bending during experiments and test setup vibration. Cutting force remained constant for coated and bare needles because the needle tip area was small, and the small-coated area did not affect cutting forces. At 35 mm insertion depth, there was a 25% difference between the experimental force data for the bare needle and the force model data. However, there was only a 0.33% difference between the experimental force data for the coated needle and the force model data. The model and experimental insertion force were compared at the maximum insertion depth since the experimental data used to obtain force parameters were collected at that depth.

The study findings confirm the accuracy of the insertion force model, which was compared directly to experimental data. The model was developed using force data collected in previous sections and closely resembles the experimental data. However, variations in PVC gel tissue properties and the internal structure of the bovine kidney make it challenging to predict insertion force accurately, leading to some discrepancies between the experimental and model data. It is important to note that the insertion force model is specific to tissue type and can only predict insertion force up to a depth of 35 mm based on the model populated with experimental data at that depth. For deeper insertion depths, the model needs to be populated with data from experiments performed at those depths. Moreover, the model cannot capture the needle interaction with different tissue structures, such as fibers and blood vessels in the bovine kidney, resulting in some small peaks and valleys in the experimental data.

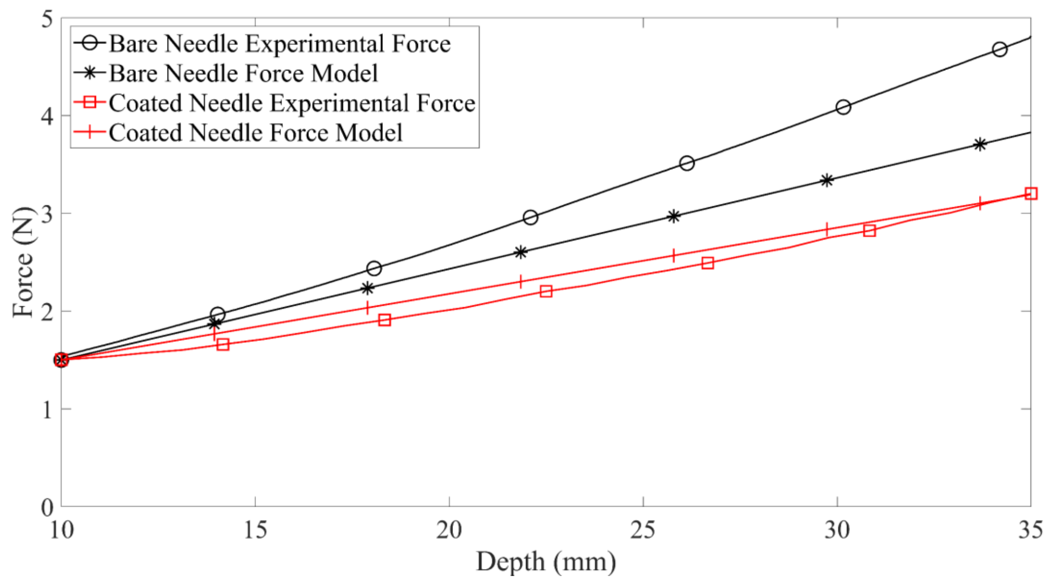

Figure 3.16 Comparison of insertion force model and experimental insertion force of coated needle and bare needle inside the PVC gel. The standard deviation of the coated needle experimental insertion force range 0.028 N ≤ SD ≤ 0.044 N. The standard deviation of the bare needle experimental insertion force range 0.023 N ≤ SD ≤0.12 N.

Figure 3.17 illustrates the force versus insertion depth graph of the insertion force of the model compared to the experimental insertion force of coated and bare needle inside the bovine kidney. Using the average cutting coefficient of 208 Ns/m for the bovine kidney, the cutting force at 5 mm/s is approximately 1N. The experimental insertion force data are nonlinear and irregular due to the heterogeneous structure of bovine kidneys, including blood vessels, fibers, and various layers of tissues. In this case, the coating did not change the cutting force for the coated needle. It is important to note that the Coulomb friction force is the main parameter that reduces the insertion force in the coated needle, and the coating did not significantly influence the viscous and elastic forces. At a 35 mm insertion depth, the error between the bare needle experimental force data and the force model data is 6.5%, while the error between the coated needle experimental force data and the force model data is 17.1%.

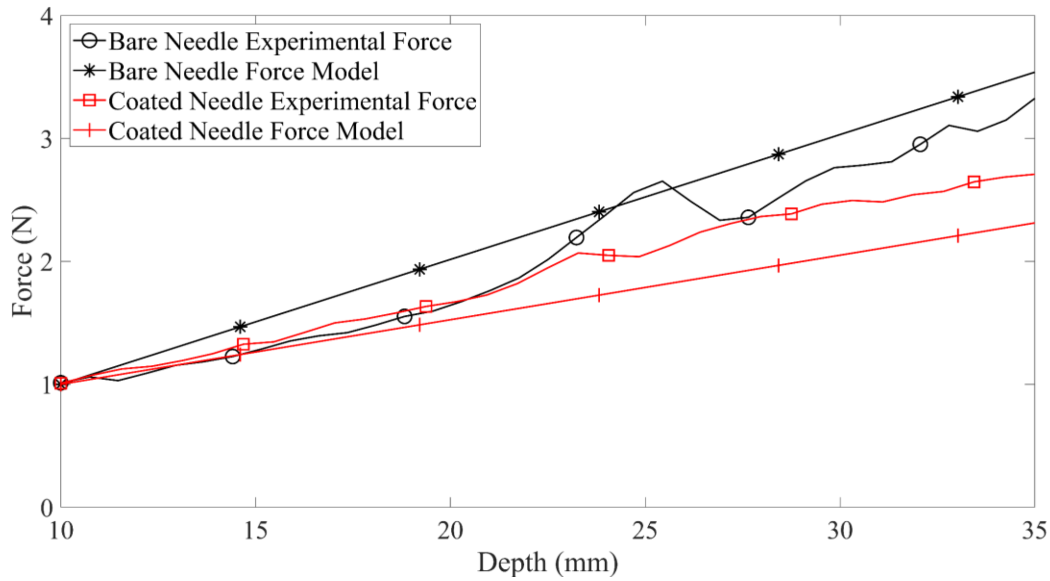

Figure 3.17 Comparison of insertion force of the model and experimental insertion force of coated needle and bare needle inside the bovine kidney. The standard deviation of coated needle experimental insertion force range 0.048 N≤ SD ≤ to 0.080 N. The standard deviation of bare needle experimental insertion force range 0.041 N ≤ SD ≤ to 0.052 N.

Figures 3.16 and 3.17, along with Tables 3.5 and 3.6, demonstrate that the reduction in Coulomb friction force is the primary factor contributing to the decreased insertion force of coated needles. However, the coating has little effect on the viscous and elastic forces compared to friction. This is due to the low deflection of tissue and insertion speed during needle insertion. Therefore, low-lubrication coatings such as PDA, PTFE, and C on the needle can have a significant impact on the Coulomb friction force. Although this model assumes that the needle remains straight throughout insertion and extraction, slight needle deflection can alter the measured insertion force. Despite these limitations, the model is still useful in haptic simulation and event detection. Since this model is tissue-specific, imaging techniques such as fibro scan should be used to study the internal structure of the tissue before surgery planning and simulation. The use of this model during pre-planning and simulation, combined with data collection, can provide valuable information during surgical procedures. If there is a significant deviation in real-time force parameters compared to previously collected data, it may indicate potential inaccuracies in needle insertion, allowing for greater control over the needle insertion process.

CHAPTER 4

CONCLUSION AND FUTURE WORK

4.1 Conclusion

This thesis hypothesized that the coating would decrease the insertion forces due to PDA-PTFE-C coating because of its non-stick, low friction properties. The results of the study showed that the addition of activated Carbon particles in the PDA-PTFE films significantly decreased the average insertion and extraction forces by 62% and 64%, respectively, in PVC tissue phantom and by 49% and 30%, respectively, in bovine kidney tissue. The findings obtained from the Atomic Force Microscope (AFM) analysis unveiled substantial reductions in both the maximum average friction force and root mean square surface roughness when comparing the coated needle surface with the bare needle. Specifically, the AFM analysis revealed a remarkable reduction of 65.7% in the maximum average friction force for the coated needle surface compared to the bare needle. Furthermore, the root means square surface roughness exhibited a significant decrease of 56.9% in the coated needle surface as compared to the bare needle. These outcomes demonstrate the effectiveness of the coating in minimizing friction and insertion forces and improving the overall surface smoothness of the needle, highlighting its potential to enhance insertion performance.

The needle insertion force model section presents the various forces acting on a needle during a surgical procedure, including Coulomb friction, viscous, elastic, and cutting forces. The study found that Coulomb friction significantly reduces insertion forces, indicating that the low friction of PTFE and C helped in reducing the insertion force. Furthermore, the study shows that viscous and elastic forces are minor compared to Coulomb friction and cutting forces which is due to low insertion speed and tissue deformation. The study results are specific to a tissue with a 35mm insertion depth, and for depths greater than 35mm, the model needs to be updated with additional experimental data using thicker tissue. Despite its limitations, the model can still be used in haptic medical devices that require the cutting, Coulomb friction, viscous, and elastic data independently. The model can also aid in developing needle-based surgical instruments, improving the accuracy of needle insertion, and designing haptic-based surgical simulators that improve the proficiency and skill of surgeons.

Finally, this dissertation discusses the impact of PDA-PTFE-C coated needles on tissue damage during insertion and extraction. The study found that PDA-PTFE-C coated needles can reduce tissue damage during insertion and extraction compared to bare needles. The histological analysis supports this conclusion, demonstrating 39% less tissue damage with coated needles. These findings suggest that the needle coating and the ability to predict the forces acting on the needle during surgical procedures can aid in designing surgical needles that minimize the forces acting on the needle, reducing the risk of complications and providing a more comfortable experience for the patient. However, more research is needed to study its biocompatibility, coefficient of friction, and sterilization. Nonetheless, the study concludes that the composite coating of PDA-PTFE-C significantly reduces insertion and extraction forces and tissue damage, which could improve the performance of surgical needles during percutaneous procedures.

4.2 Future Work

The application of PDA-PTFE-C coating on the needle has demonstrated significant enhancements in terms of insertion and extraction forces, friction force, and surface roughness. The insertion force and extraction force play a critical role in needle insertion mechanics, and reducing these forces can help minimize tissue damage, as corroborated by histological studies. Furthermore, the post-puncture insertion force model of the coated needle insertion force provides a better understanding of the mechanics involved by revealing that the Coulomb friction force is the primary contributor to the reduction in insertion force. However, further investigations are required to ensure the biocompatibility of this coating for clinical research. Future studies related to this subject are also outlined below.

i. The coating PDA-PTFE-C exhibited no observable delamination, and repeated insertion and extraction of a coated needle yielded only minor changes in insertion and extraction forces, providing evidence of the coating structural integrity. Nonetheless, it is imperative to conduct additional investigations into the durability of the needle coating, such as employing scratch and abrasion resistance tests, in order to facilitate clinical research.

ii. Although friction coefficient measurement was performed with the sliding tissue experiment (Appendix B), it is essential to note that in that study, the viscoelastic properties of the tissue were neglected. Therefore, a separate study using a friction coefficient measurement instrument is necessary to obtain more comprehensive and accurate results. Friction coefficient testing should be performed using an atomic force microscope to compare the friction coefficient of PDA-PTFE and C coated needle with the bare needles.

iii. Utilize the coating technique on additional medical instruments that require a low-friction surface, while maintaining the devices original geometry.

iv. Conduct a comprehensive investigation of alternative approaches for coating needles with PDA-PTFE and C, with the potential for adaptation to diverse industries beyond medical needles.

v. Since it has been established that needle coating reduces surface roughness, insertion force, and tissue damage, a comprehensive study should be conducted to establish a direct correlation through formulas or equations connecting all these parameters.

vi. The present paper details a post-puncture force model for insertion force modeling that facilitates the distribution of friction force into Coulomb friction, viscous, and elastic forces. However, the model may need to be further investigated, particularly in cases where the tissue is very soft and may be easily deformed. It may be necessary to study both the post-puncture model and the pre-puncture model in these cases to ensure accurate predictions of insertion forces.

vii. The work discussed in this dissertation offers promising potential for the application of the insertion force model in future robotic-assisted surgeries. This model could be utilized to develop a system that enhances the precision and efficacy of needle insertion procedures. One avenue for future research is the integration of a force sensor between the robotic arm and the needle. This sensor would measure the insertion force in real-time during surgery. Subsequently, the recorded insertion force could be decomposed into its primary components - the cutting force and friction forces - by employing the analytical insertion force model detailed in this thesis. By using pre-existing data, which were measured previously, in conjunction with this model, the accuracy of force distribution could be continually refined. This proposed system has the potential to significantly improve control during surgical procedures, possibly reducing surgical risks and improving patient outcomes. Ultimately, the research encapsulated in this thesis paves the way for the future development of more sophisticated and safer robotic-assisted surgical methodologies.

REFERENCES

[1] S. H. Parker, A. T. Stavros, and M. A. Dennis, “Needle biopsy techniques,” *Radiol. Clin. North Am.*, vol. 33, no. 6, pp. 1171–1186, Nov. 1995, doi: 10.1016/S0033-8389(22)00651-0.

[2] C. Chargari *et al.*, “Brachytherapy: An overview for clinicians,” *CA. Cancer J. Clin.*, vol. 69, no. 5, pp. 386–401, Sep. 2019, doi: 10.3322/CAAC.21578.

[3] N. Abolhassani, R. Patel, and M. Moallem, “Needle insertion into soft tissue: A survey,” *Med. Eng. Phys.*, vol. 29, no. 4, pp. 413–431, May 2007, doi: 10.1016/J.MEDENGPHY.2006.07.003.

[4] D. J. van Gerwen, J. Dankelman, and J. J. van den Dobbelsteen, “Needle–tissue interaction forces – A survey of experimental data,” *Med. Eng. Phys.*, vol. 34, no. 6, pp. 665–680, Jul. 2012, doi: 10.1016/J.MEDENGPHY.2012.04.007.

[5] G. Dogangil, B. L. Davies, and F. Rodriguez Y Baena, “A review of medical robotics for minimally invasive soft tissue surgery,” *Proc. Inst. Mech. Eng. H: J. Eng. Med.*, vol. 224, no. 5, pp. 653–679, Jul. 2009, doi: 10.1243/09544119JEIM591.

[6] G. Kronreif, M. Fürst, J. Kettenbach, M. Figl, and R. Hanel, “Robotic guidance for percutaneous interventions,” *Adv. Robot.*, vol. 17, no. 6, pp. 541–560, 2012, doi: 10.1163/156855303360675532.

[7] N. Abolhassani, R. Patel, and F. Ayazi, “Effects of different insertion methods on reducing needle deflection,” *Annu. Int. Conf. IEEE Eng. Med. Biol. - Proc.*, pp. 491–494, 2007, doi: 10.1109/IEMBS.2007.4352330.

[8] M. Mahvash and P. E. Dupont, “Mechanics of dynamic needle insertion into a biological material,” *IEEE Trans. Biomed. Eng.*, vol. 57, no. 4, pp. 934–943, 2010, doi: 10.1109/TBME.2009.2036856.

[9] M. Sahlabadi, S. T. R. Gidde, P. Gehret, K. Pourfarhangi, B. Bayarmagnai, and P. Hutapea, “Histological evaluation of tissue damage caused by bioinspired needle insertion,” *Adv. Biomater. Devices Med.*, vol. 5, no. 1, pp. 1–6, 2018, Accessed: Jun. 02, 2023. [Online]. Available: http://abiodem.com/article.php?id=114.

[10] N. Abolhassani, R. V. Patel, and F. Ayazi, “Minimization of needle deflection in robot-assisted percutaneous therapy,” *Int. J. Med. Robot. Comput. Assist. Surg.*, vol. 3, no. 2, pp. 140–148, Jun. 2007, doi: 10.1002/RCS.136.

[11] M. Sahlabadi and P. Hutapea, “Tissue deformation and insertion force of bee-stinger inspired surgical needles,” *J. Med. Devices, Trans. ASME*, vol. 12, no. 3, Sep. 2018, doi: 10.1115/1.4040637/366204.

[12] M. Giovannini, H. Ren, J. Cao, and K. Ehmann, “Study on design and cutting parameters of rotating needles for core biopsy,” *J. Mech. Behav. Biomed. Mater.*, vol. 86, pp. 43–54, Oct. 2018, doi: 10.1016/J.JMBBM.2018.06.013.

[13] J. T. Hing, A. D. Brooks, and J. P. Desai, “Reality-based needle insertion simulation for haptic feedback in prostate brachytherapy,” *Proc. - IEEE Int. Conf. Robot. Autom.*, vol. 2006, pp. 619–624, 2006, doi: 10.1109/ROBOT.2006.1641779.

[14] K. I. Patel, L. Zhu, S. T. R. Gidde, F. Ren, and P. Hutapea, “Influence of Composite Polymer Coatings on the Insertion Force of Needle-Like Structure in Soft Materials,” *ASME Int. Mech. Eng. Congr. Expo. Proc.*, vol. 5, Feb. 2021, doi: 10.1115/IMECE2020-24341.

[15] N. Abolhassani, R. Patel, and M. Moallem, “Control of soft tissue deformation during robotic needle insertion,” *Minim Invasive Ther Allied Technol*, vol. 15, no. 3, pp. 165–176, Jun. 2009, doi: 10.1080/13645700600771645.

[16] S. T. R. Gidde and P. Hutapea, “Design and Experimental Evaluation of Mosquito-Inspired Needle Structure in Soft Materials,” *ASME Int. Mech. Eng. Congr. Expo. Proc.*, vol. 5, Feb. 2021, doi: 10.1115/IMECE2020-24320.

[17] W. L. McClung, S. C. Daniel, W. McGregor, J. G. Thacker, G. T. Rodeheaver, and R. F. Edlich, “Enhancing needle durability by silicone coating of surgical needles,” *J. Emerg. Med.*, vol. 13, no. 4, pp. 515–518, 1995, doi: 10.1016/0736-4679(95)80010-7.

[18] G. Dearnaley and J. H. Arps, “Biomedical applications of diamond-like carbon (DLC) coatings: A review,” *Surf. Coatings Technol.*, vol. 200, no. 7, pp. 2518–2524, Dec. 2005, doi: 10.1016/J.SURFCOAT.2005.07.077.

[19] J. P. Chu *et al.*, “Thin film metallic glasses: Unique properties and potential applications,” *Thin Solid Films*, vol. 520, no. 16, pp. 5097–5122, Jun. 2012, doi: 10.1016/J.TSF.2012.03.092.

[20] S. Foust, “Ultrathin PTFE Coating for Hypodermic Needles Enabled by Mussel-Inspired PDA Adhesive Layer,” *Mech. Eng. Undergrad. Honor. Theses*, May 2014, Accessed: Jun. 02, 2023. [Online]. Available: https://scholarworks.uark.edu/meeguht/38.

[21] K. I. Patel, L. Zhu, F. Ren, and P. Hutapea, "Effect of composite coating on insertion mechanics of needle structure in soft materials," *Med. Eng. Phys.*, vol. 95, pp. 104–110, Sep. 2021, doi: 10.1016/J.MEDENGPHY.2021.07.008.

[22] M. Sahlabadi and P. Hutapea, "Novel design of honeybee-inspired needles for percutaneous procedure," *Bioinspir. Biomim.*, vol. 13, no. 3, May 2018, doi: 10.1088/1748-3190/AAA348.

[23] S. T. R. Gidde, S. R. Acharya, S. Kandel, N. Pleshko, and P. Hutapea, "Assessment of tissue damage from mosquito-inspired surgical needle," *Minim. Invasive Ther. Allied Technol.*, vol. 31, no. 7, pp. 1112–1121, 2022, doi: 10.1080/13645706.2022.2051718.

[24] M. Scali, T. P. Pusch, P. Breedveld, and D. Dodou, "Ovipositor-inspired steerable needle: design and preliminary experimental evaluation," *Bioinspir. Biomim.*, vol. 13, no. 1, p. 016006, Dec. 2017, doi: 10.1088/1748-3190/AA92B9.

[25] S. B. Adams, G. E. Moore, M. Elrashidy, A. Mohamed, and P. W. Snyder, "Effect of needle size and type, reuse of needles, insertion speed, and removal of hair on contamination of joints with tissue debris and hair after arthrocentesis," *Vet. Surg.*, vol. 39, no. 6, pp. 667–673, 2010, doi: 10.1111/J.1532-950X.2010.00649.X.

[26] M. D. O'Leary, C. Simone, T. Washio, K. Yoshinaka, and A. M. Okamura, "Robotic needle insertion: Effects of friction and needle geometry," *Proc. - IEEE Int. Conf. Robot. Autom.*, vol. 2, pp. 1774–1780, 2003, doi: 10.1109/ROBOT.2003.1241851.

[27] S. T. R. Gidde, S. Islam, A. Kim, and P. Hutapea, "Experimental study of mosquito-inspired needle to minimize insertion force and tissue deformation," *Proc Inst Mech Eng H*, vol. 237, no. 1, pp. 113–123, Nov. 2022, doi: 10.1177/09544119221137133.

[28] J. Stellman, "Development, production, and characterization of plastic hypodermic needles," Georgia Institute of Technology.

[29] A. Chebolu, A. Mallimoggala, and Nagahanumaiah, "Modelling of Cutting Force and Deflection of Medical Needles with Different Tip Geometries," *Procedia Mater. Sci.*, vol. 5, pp. 2023–2031, Jan. 2014, doi: 10.1016/J.MSPRO.2014.07.535.

[30] A. M. Okamura, C. Simone, and M. D. O'Leary, "Force modeling for needle insertion into soft tissue," *IEEE Trans. Biomed. Eng.*, vol. 51, no. 10, pp. 1707–1716, Oct. 2004, doi: 10.1109/TBME.2004.831542.

[31] S. Zhang *et al.*, “Fibrinogen Deposition on Silicone Oil-Infused Silver-Releasing Urinary Catheters Compromises Antibiofilm and Anti-Encrustation Properties,” *Langmuir*, vol. 39, no. 4, pp. 1562–1572, Jan. 2023.

[32] Y. Wang, B. L. Tai, H. Yu, and A. J. Shih, “Silicone-based tissue-mimicking phantom for needle insertion simulation,” *J. Med. Devices, Trans. ASME*, vol. 8, no. 2, Jun. 2014, doi: 10.1115/1.4026508/448103.

[33] E. Caló and V. V. Khutoryanskiy, “Biomedical applications of hydrogels: A review of patents and commercial products,” *Eur. Polym. J.*, vol. 65, pp. 252–267, Apr. 2015, doi: 10.1016/J.EURPOLYMJ.2014.11.024.

[34] L. Oyarte Gálvez, M. Brió Pérez, and D. Fernández Rivas, “High speed imaging of solid needle and liquid micro-jet injections,” *J. Appl. Phys.*, vol. 125, no. 14, Apr. 2019, doi: 10.1063/1.5074176/150437.

[35] I. Saha and V. K. Rai, “Hyaluronic acid based microneedle array: Recent applications in drug delivery and cosmetology,” *Carbohydr. Polym.*, vol. 267, Sep. 2021, doi: 10.1016/J.CARBPOL.2021.118168.

[36] W. L. McClung, S. C. Daniel, W. McGregor, J. G. Thacker, G. T. Rodeheaver, and R. F. Edlich, “Enhancing needle durability by silicone coating of surgical needles,” *J. Emerg. Med.*, vol. 13, no. 4, pp. 515–518, Jul. 1995, doi: 10.1016/0736-4679(95)80010-7.

[37] M. Doerzbacher, A. Barnett, N. Brandmeir, D. Wolfe, S. Zheng, and J. Moore, “Advanced needle coatings for improved lumbar drain procedure,” *J. Med. Devices, Trans. ASME*, vol. 7, no. 3, Mar. 2013, doi: 10.1115/1.4024485/375901.

[38] D. Lehmann *et al.*, “New PTFE-polyamide compounds,” *Des. Monomers Polym.*, vol. 5, no. 2–3, pp. 317–324, 2012, doi: 10.1163/156855502760158006.

[39] M. Chen, Y. Zhang, H. B. Wu, L. Liu, and H. Wang, “A study on fluorinated ethylene propylene/polytetrafluoroethylene foam coating composite as potential flue gas filtration materials,” *J. Ind. Text.*, vol. 51, no. 1, pp. 659S-674S, Jun. 2022.

[40] J. Kim, S. Park, G. Nam, Y. Choi, S. Woo, and S. H. Yoon, “Bioinspired microneedle insertion for deep and precise skin penetration with low force: Why the application of mechanophysical stimuli should be considered,” *J. Mech. Behav. Biomed. Mater.*, vol. 78, pp. 480–490, Feb. 2018, doi: 10.1016/J.JMBBM.2017.12.006.

[41] T. A. Lenau, T. Hesselberg, A. Drakidis, P. Silva, and S. Gomes, "Mosquito inspired medical needles," *Bioinspiration, Biomimetics, Bioreplication 2017*, vol. 10162, pp. 47–59, Apr. 2017, doi: 10.1117/12.2261399.

[42] M. Sahlabadi, S. Khodaei, K. Jezler, and P. Hutapea, "Study of Bioinspired Surgery Needle Advancing in Soft Tissues," *ASME 2017 Conf. Smart Mater. Adapt. Struct. Intell. Syst. SMASIS 2017*, vol. 1, Nov. 2017, doi: 10.1115/SMASIS2017-3915.

[43] A. C. Barnett, Y. S. Lee, and J. Z. Moore, "Fracture Mechanics Model of Needle Cutting Tissue," *J. Manuf. Sci. Eng. Trans. ASME*, vol. 138, no. 1, Feb. 2016, doi: 10.1115/1.4030374/375489.

[44] N. J. Van De Berg, T. L. De Jong, D. J. Van Gerwen, J. Dankelman, and J. J. Van Den Dobbelsteen, "The influence of tip shape on bending force during needle insertion," *Sci. Reports 2017 71*, vol. 7, no. 1, pp. 1–8, Jan. 2017, doi: 10.1038/srep40477.

[45] C. Chargari *et al.*, "Brachytherapy: An overview for clinicians," *CA. Cancer J. Clin.*, vol. 69, no. 5, pp. 386–401, Sep. 2019, doi: 10.3322/CAAC.21578.

[46] V. Egorov, S. Tsyuryupa, S. Kanilo, M. Kogit, and A. Sarvazyan, "Soft tissue elastometer," *Med. Eng. Phys.*, vol. 30, no. 2, pp. 206–212, Mar. 2008, doi: 10.1016/J.MEDENGPHY.2007.02.007.

[47] A. A. Zadpoor, "Mechanics of Biological Tissues and Biomaterials: Current Trends," *Mater. 2015, Vol. 8, Pages 4505-4511*, vol. 8, no. 7, pp. 4505–4511, Jul. 2015, doi: 10.3390/MA8074505.

[48] N. Hungr, J. A. Long, V. Beix, and J. Troccaz, "A realistic deformable prostate phantom for multimodal imaging and needle-insertion procedures," *Med. Phys.*, vol. 39, no. 4, pp. 2031–2041, Apr. 2012, doi: 10.1118/1.3692179.

[49] G. M. Spirou, A. A. Oraevsky, I. Alex Vitkin, and W. M. Whelan, "Optical and acoustic properties at 1064 nm of polyvinyl chloride-plastisol for use as a tissue phantom in biomedical optoacoustics," *Phys. Med. Biol.*, vol. 50, no. 14, p. N141, Jun. 2005, doi: 10.1088/0031-9155/50/14/N01.

[50] M. Scali, D. Kreeft, P. Breedveld, and D. Dodou, "Design and evaluation of a wasp-inspired steerable needle," *Bioinspiration, Biomimetics, Bioreplication 2017*, vol. 10162, pp. 34–46, Apr. 2017, doi: 10.1117/12.2259978.

[51] K. R. Henken, P. R. Seevinck, J. Dankelman, and J. J. van den Dobbelsteen, "Manually controlled steerable needle for MRI-guided percutaneous interventions," *Med. Biol. Eng. Comput.*, vol. 55, no. 2, pp. 235–244, Feb. 2017.

[52] S. Misra, K. B. Reed, A. S. Douglas, K. T. Ramesh, and A. M. Okamura, "Needle-tissue interaction forces for bevel-tip steerable needles," *Proc. 2nd Bienn. IEEE/RAS-EMBS Int. Conf. Biomed. Robot. Biomechatronics, BioRob 2008*, pp. 224–231, 2008, doi: 10.1109/BIOROB.2008.4762872.

[53] M. Mahvash and P. E. Dupont, "Fast needle insertion to minimize tissue deformation and damage," *Proc. - IEEE Int. Conf. Robot. Autom.*, pp. 3097–3102, 2009, doi: 10.1109/ROBOT.2009.5152617.

[54] F. Casanova, P. R. Carney, and M. Sarntinoranont, "Effect of Needle Insertion Speed on Tissue Injury, Stress, and Backflow Distribution for Convection-Enhanced Delivery in the Rat Brain," *PLoS One*, vol. 9, no. 4, p. e94919, Apr. 2014, doi: 10.1371/JOURNAL.PONE.0094919.

[55] A. E. Healey *et al.*, "In vivo force during arterial interventional radiology needle puncture procedures.," *Stud. Health Technol. Inform.*, vol. 111, pp. 178–184, Jan. 2005, Accessed: Jun. 02, 2023. [Online]. Available: https://europepmc.org/article/MED/15718723.

[56] P. Han and K. Ehmann, "Study of the effect of cannula rotation on tissue cutting for needle biopsy," *Med. Eng. Phys.*, vol. 35, no. 11, pp. 1584–1590, Nov. 2013, doi: 10.1016/J.MEDENGPHY.2013.05.001.

[57] S. T. R. Gidde, S. Islam, A. Kim, and P. Hutapea, "Experimental study of mosquito-inspired needle to minimize insertion force and tissue deformation," *Proc. Inst. Mech. Eng. H: J. Eng. Med.*, vol. 237, no. 1, pp. 113–123, Nov. 2022, doi: 10.1177/09544119221137133.

[58] H. A. Alturkistani, F. M. Tashkandi, and Z. M. Mohammedsaleh, "Histological Stains: A Literature Review and Case Study," *Glob. J. Health Sci.*, vol. 8, no. 3, p. p72, Jun. 2015, doi: 10.5539/GJHS.V8N3P72.

[59] S. Foust, "Ultrathin PTFE Coating for Hypodermic Needles Enabled by Mussel-Inspired PDA Adhesive Layer," University Of Arkansas, 2014.

[60] F. Casanova, P. R. Carney, and M. Sarntinoranont, "In vivo evaluation of needle force and friction stress during insertion at varying insertion speed into the brain," *J. Neurosci. Methods*, vol. 237, pp. 79–89, Nov. 2014, doi: 10.1016/J.JNEUMETH.2014.08.012.

[61] R. Barua, S. Das, A. Roy Chowdhury, and P. Datta, "Experimental and simulation investigation of surgical needle insertion into soft tissue mimic biomaterial for minimally invasive surgery (MIS)," *Proc. Inst. Mech. Eng. Part H J. Eng. Med.*, vol. 237, no. 2, pp. 254–264, Feb. 202.

[62] I. Usach, R. Martinez, T. Festini, and J. E. Peris, “Subcutaneous Injection of Drugs: Literature Review of Factors Influencing Pain Sensation at the Injection Site,” *Adv. Ther.*, vol. 36, no. 11, pp. 2986–2996, Nov. 2019, doi: 10.1007/S12325-019-01101-6/TABLES/2.

[63] R. Tsumura, Y. Takishita, and H. Iwata, “Needle Insertion Control Method for Minimizing Both Deflection and Tissue Damage,” *J. Med. Robot. Res.*, vol. 04, no. 01, p. 1842005, Mar. 2019, doi: 10.1142/S2424905X18420059.

[64] R. Tsumura, Y. Takishita, Y. Fukushima, and H. Iwata, “Histological evaluation of tissue damage caused by rotational needle insertion,” *Annu. Int. Conf. IEEE Eng. Med. Biol. Soc. IEEE Eng. Med. Biol. Soc. Annu. Int. Conf.*, vol. 2016, pp. 5120–5123, Oct. 2016, doi: 10.1109/EMBC.2016.7591879.

[65] D. Karnopp, “Computer Simulation of Stick-Slip Friction in Mechanical Dynamic Systems,” *J. Dyn. Syst. Meas. Control*, vol. 107, no. 1, pp. 100–103, Mar. 1985, doi: 10.1115/1.3140698.

[66] S. Jiang, P. Li, Y. Yu, J. Liu, and Z. Yang, “Experimental study of needle–tissue interaction forces: Effect of needle geometries, insertion methods and tissue characteristics,” *J. Biomech.*, vol. 47, no. 13, pp. 3344–3353, Oct. 2014, doi: 10.1016/J.JBIOMECH.2014.08.007.

[67] J. A. Epaarachchi, “The effect of viscoelasticity on fatigue behaviour of polymer matrix composites,” *Creep Fatigue Polym. Matrix Compos.*, pp. 492–513, Jan. 2011, doi: 10.1533/9780857090430.3.492.

[68] S. P. DiMaio and S. E. Salcudean, “Needle Insertion Modeling and Simulation,” *IEEE Trans. Robot. Autom.*, vol. 19, no. 5, pp. 864–875, Oct. 2003, doi: 10.1109/TRA.2003.817044.

[69] M. Sahlabadi, “A novel bioinspired design for surgical needles to reduce tissue damage in interventional procedures,” Temple University. Libraries, 2018.

[70] Y. Fukushima and K. Naemura, “Estimation of the friction force during the needle insertion using the disturbance observer and the recursive least square,” *ROBOMECH J.*, vol. 1, no. 1, pp. 1–8, Dec. 2014, doi: 10.1186/S40648-014-0014-7/FIGURES/10.

[71] C. Richard, M. R. Cutkosky, and K. MacLean, “Friction Identification for Haptic Display,” *ASME Int. Mech. Eng. Congr. Expo. Proc.*, vol. 1999-J, pp. 327–334, Dec. 2021, doi: 10.1115/IMECE1999-0043.

[72] H. A. Ching, D. Choudhury, M. J. Nine, and N. A. Abu Osman, "Effects of surface coating on reducing friction and wear of orthopaedic implants," *Sci. Technol. Adv. Mater.*, vol. 15, no. 1, p. 21, Feb. 2014, doi: 10.1088/1468-6996/15/1/014402.

[73] I. Muro-Fraguas, A. Sainz-García, R. Múgica-Vidal, E. Sainz-García, A. González-Marcos, and F. Alba-Elías, "Low-friction coatings on medical needles through atmospheric-pressure plasma-polymerization technology," *Plasma Process. Polym.*, p. e2200174, 2022, doi: 10.1002/PPAP.202200174.

[74] S. Beckford, L. Mathurin, J. Chen, R. A. Fleming, and M. Zou, "The effects of polydopamine coated Cu nanoparticles on the tribological properties of polydopamine/PTFE coatings," *Tribol. Int.*, vol. 103, pp. 87–94, Nov. 2016, doi: 10.1016/J.TRIBOINT.2016.06.031.

[75] A. Khoddamzadeh, R. Liu, and X. Wu, "Novel polytetrafluoroethylene (PTFE) composites with newly developed Tribaloy alloy additive for sliding bearings," *Wear*, vol. 266, no. 7–8, pp. 646–657, Mar. 2009, doi: 10.1016/J.WEAR. 2008.08.007.

[76] H. Kataoka, T. Washio, K. Chinzei, K. Mizuhara, C. Simone, and A. M. Okamura, "Measurement of the tip and friction force acting on a needle during penetration," *Lect. Notes Comput. Sci. (including Subser. Lect. Notes Artif. Intell. Lect. Notes Bioinformatics)*, vol. 2488, pp. 216–223, 2002, doi: 10.1007/3-540-45786-0_27/COVER.

[77] M. Heverly, P. Dupont, and J. Triedman, "Trajectory optimization for dynamic needle insertion," *Proc. - IEEE Int. Conf. Robot. Autom.*, vol. 2005, pp. 1646–1651, 2005, doi: 10.1109/ROBOT.2005.1570349.

[78] M. Sahlabadi *et al.*, "Polydopamine Coating for Thermal Insulation of Shape Memory Alloy Wires," *ASME 2016 Conf. Smart Mater. Adapt. Struct. Intell. Syst. SMASIS 2016*, vol. 1, Nov. 2016, doi: 10.1115/SMASIS2016-9265.

[79] H. Lee, S. M. Dellatore, W. M. Miller, and P. B. Messersmith, "Mussel-inspired surface chemistry for multifunctional coatings," *Science*, vol. 318, no. 5849, pp. 426–430, Oct. 2007, doi: 10.1126/SCIENCE.1147241.

[80] N. A. Aziz *et al.*, "Influence of activated carbon filler on the mechanical properties of wood composites," *ARPN J. Eng. Appl. Sci.*, vol. 10, pp. 376-386, Jan. 2015.

[81] S. Baik, D. Yoon, H. I. Lee, M. K. Ji, L. Gyu-Sun, and L. Young-Ze, "Frictional Performances of Activated Carbon and Carbon Blacks as Lubricant Additives," *Tribol. Trans.*, vol. 52, no. 1, pp. 133–137, Jan. 2009, doi: 10.1080/10402000802192693.

[82] W. Li, B. Belmont, and A. Shih, “Design and Manufacture of Polyvinyl Chloride (PVC) Tissue Mimicking Material for Needle Insertion,” *Procedia Manuf.*, vol. 1, pp. 866–878, Jan. 2015, doi: 10.1016/J.PROMFG.2015.09.078.

[83] W. Sun, “Principles of Atomic Force Microscopy,” *At. Force Microsc. Mol. Cell Biol.*, pp. 1–28, 2018, doi: 10.1007/978-981-13-1510-7_1.

[84] C. W. Yang *et al.*, “Lateral Force Microscopy of Interfacial Nanobubbles: Friction Reduction and Novel Frictional Behavior,” *Sci. Reports 2018 81*, vol. 8, no. 1, pp. 1–10, Feb. 2018, doi: 10.1038/s41598-018-21264-6.

[85] Á. G. Nagy, J. Kámán, R. Horváth, and A. Bonyár, “Spring constant and sensitivity calibration of FluidFM micropipette cantilevers for force spectroscopy measurements,” *Sci. Reports 2019 91*, vol. 9, no. 1, pp. 1–11, Jul. 2019, doi: 10.1038/s41598-019-46691-x.

[86] H. A. Alturkistani, F. M. Tashkandi, and Z. M. Mohammedsaleh, “Histological Stains: A Literature Review and Case Study,” *Glob. J. Health Sci.*, vol. 8, no. 3, pp. 72–79, Jun. 2015, doi: 10.5539/GJHS.V8N3P72.

[87] M. Slaoui and L. Fiette, “Histopathology procedures: from tissue sampling to histopathological evaluation,” *Methods Mol. Biol.*, vol. 691, pp. 69–82, 2011, doi: 10.1007/978-1-60761-849-2_4.

[88] O. Zhanmu, X. Yang, H. Gong, and X. Li, “Paraffin-embedding for large volume bio-tissue,” *Sci. Reports 2020 101*, vol. 10, no. 1, pp. 1–8, Jul. 2020, doi: 10.1038/s41598-020-68876-5.

[89] K. Patel and P. Hutapea, “Experimental and analytical study on insertion force of composite-coated needle in soft tissue material,” *Proc. Inst. Mech. Eng. H: J. Eng. Med.*, Aug. 2023, doi: 10.1177/09544119231191910.

[90] P. J. Blau, “The significance and use of the friction coefficient,” *Tribol. Int.*, vol. 34, no. 9, pp. 585–591, Sep. 2001, doi: 10.1016/S0301-679X(01)00050-0.

[91] J. Gao, W. D. Luedtke, D. Gourdon, M. Ruths, J. N. Israelachvili, and U. Landman, “Frictional forces and Amontons’ law: From the molecular to the macroscopic scale,” *J. Phys. Chem. B*, vol. 108, no. 11, pp. 3410–3425, Mar. 2004.

[92] J. P. Chu, C. C. Yu, Y. Tanatsugu, M. Yasuzawa, and Y. L. Shen, “Non-stick syringe needles: Beneficial effects of thin film metallic glass coating,” *Sci. Reports 2016 61*, vol. 6, no. 1, pp. 1–7, Aug. 2016, doi: 10.1038/srep31847.

[93] D. R. Dreyer, D. J. Miller, B. D. Freeman, D. R. Paul, and C. W. Bielawski, "Elucidating the structure of poly(dopamine)," *Langmuir*, vol. 28, no. 15, pp. 6428–6435, Apr. 2012.

[94] S. Li, C. Guo, X. Wang, C. Guan, and G. Chen, "Corrosion Inhibition Coating Based on the Self-Assembled Polydopamine Films and Its Anti-Corrosion Properties," *Polymers (Basel).*, vol. 14, no. 4, p. 794, Feb. 2022, doi: 10.3390/POLYM14040794/S1.

[95] F. A. Urrea, F. Casanova, G. A. Orozco, and J. J. García, "Evaluation of the friction coefficient, the radial stress, and the damage work during needle insertions into agarose gels," *J. Mech. Behav. Biomed. Mater.*, vol. 56, pp. 98–105, Mar. 2016, doi: 10.1016/J.JMBBM.2015.11.024.

APPENDIX A

CHEMICAL FORMULATIONS

- Polydopamine (PDA) Synthesis Procedure with Skeleton formulas [92,93]:

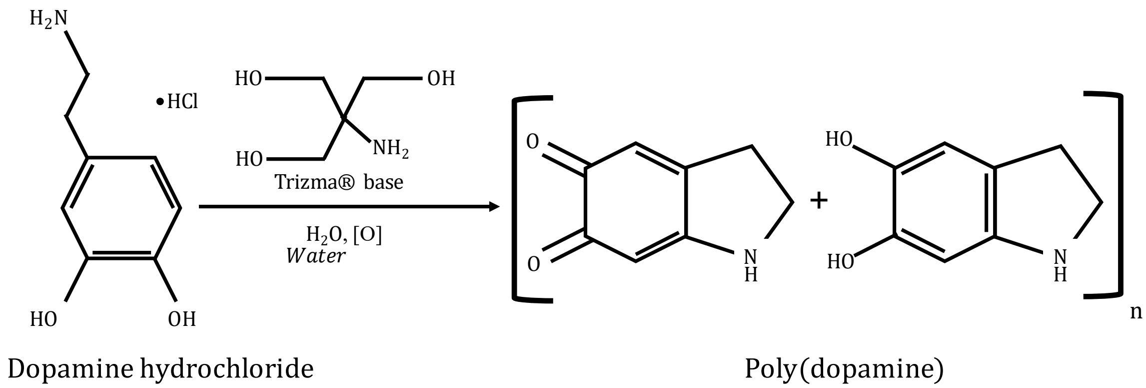

Figure A.1 Skeleton formula of Polydopamine polymerization procedure.

- Although the complexities of Polydopamine (PDA) adhesion are not entirely understood, prevalent theories highlight the crucial role of certain functional groups. The catechol groups inherent in Dopamine hydrochloride (DOPA) and the amine groups present in lysine, both constituents of Polydopamine (PDA), are considered significant contributors to this process. Due to the intricacy of the polymer bond, the skeleton formula of Polydopamine (PDA) combined with Polytetrafluoroethylene (PTFE) and activated carbon is not available. However, the graphical representation illustrating how PDA combines with PTFE and Carbon (C) filler at the molecular level is provided below in Figure A.2.

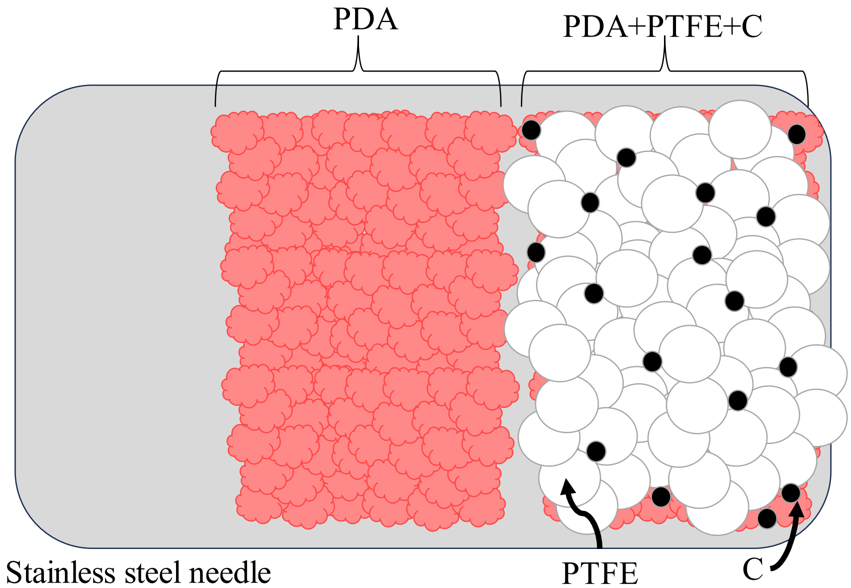

Figure A.2 Schematic of PDA, PTFE, and C on the needle surface.

APPENDIX B

MEASUREMENT OF FRICTION COEFFICIENT

Determining the coefficient of friction between a needle and tissue is challenging without the addition of bulky haptic sensors on the needle surface. Adding sensors to the needle surface could potentially alter the natural forces during insertion. Therefore, the sliding friction test method was utilized to calculate the friction coefficient between the tissue and a stainless steel A304 plate (Polished Multipurpose 304 Stainless Steel plates, McMASTER-CARR, Elmhurst, IL, USA). This technique was selected to precisely replicate the friction coefficient between the stainless-steel biopsy needle and tissue accurately. It is important to note that the roughness of the surface solely determines the friction coefficient and remains unaffected by the size. The plates (Polished Multipurpose 304 Stainless Steel plates, McMASTER-CARR, Elmhurst, IL, USA) used in the experiment were carefully chosen to match the surface properties and roughness of a typical biopsy needle, thereby validating the accuracy of our results. The plates had a mirror-like finish #8, a surface area of 6 x 6 in.^{2}, and were 0.0600 in. thick.

This experiment was inspired by Urrea et al. [95] research article. In this experiment, two different types of plates were utilized. The first type had a PDA-PTFE-C coating, while the second type had a bare plate. The test setup (Figure B.1) for this sliding friction measurement included several components: linear actuators with a force sensor mount stage, a force sensor, a lightweight tissue holder carrying a tissue sample, a thin rod, and a stainless-steel plate. One end of the force sensor was attached to the upper part of the actuator via the mount, and the other end was connected to the tissue holder using a lightweight rod. This setup facilitated an effective and direct measurement of the sliding friction force between the tissue and the stainless-steel plate.

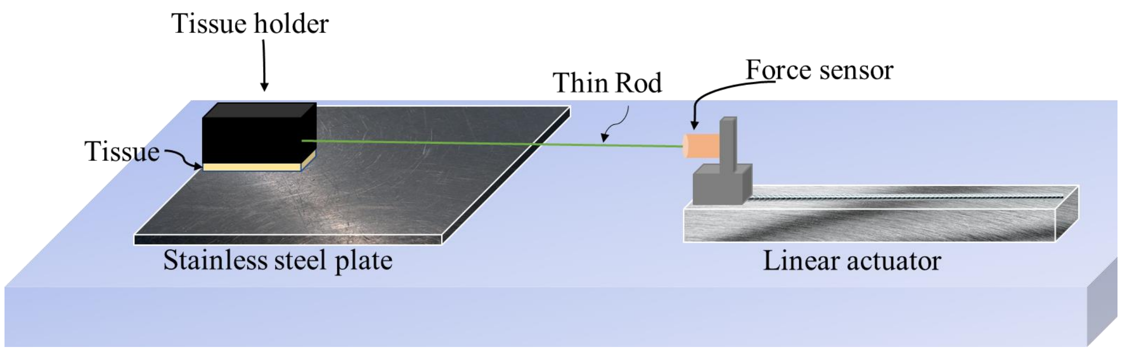

Figure B.1 Sliding friction experimental test setup.

To ensure accuracy and efficiency in our data analysis, the LabVIEW software on a dedicated computer was used to record the force sensor data systematically. This data is a crucial aspect of this experiment and was used in subsequent stages. The friction is conceptually divided into two key categories: Coulomb and viscoelastic. Coulomb friction is the force needed to overcome static friction and is largely determined by the surface roughness of both the plate and the tissue. Viscoelastic friction, on the other hand, is dependent on the relative velocity of the tissue to the plate and the extent of tissue deflection.

In this experiment, the tissue sliding velocity was maintained at a constant rate of 5 mm/s. Urrea et al. [95] assumed that the viscoelastic forces are very small because of low speed and minimal tissue deflection during the sliding phase. The forces acting on the tissue are shown in the free-body diagram (Figure B.2). In addition, keeping a constant velocity ensured zero acceleration. In this situation, the normal force can be understood as the weight of the tissue sample itself. The total friction force was determined by using friction values obtained from an experiment and a specific equation that combined Newton's second law and Coulomb friction model equations (Equation B1-B6). These equations effectively estimate the friction forces exerted on the needle during the insertion process.

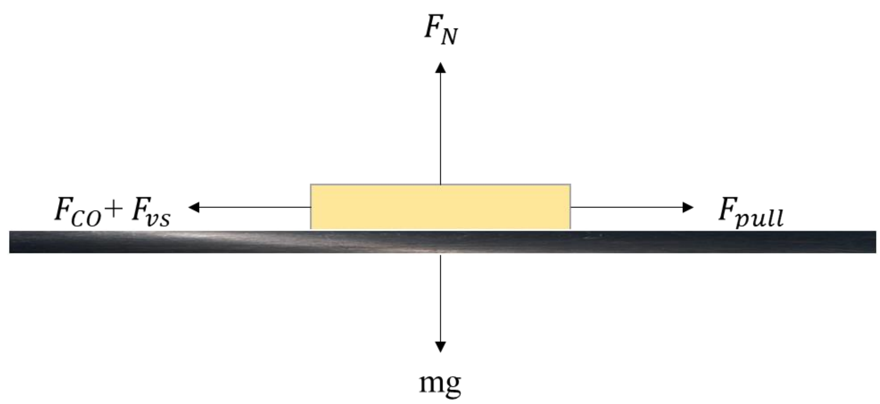

Figure B.2 Free body diagram of the tissue during sliding.

Newton's second law of motion provides insights into how an object's velocity changes when it experiences an external force. The law elaborates that the force exerted (F) on an object is equivalent to the object mass (m) times its acceleration (a). Mathematically, this relationship can be expressed as:

$$F = m\,a \tag{B1}$$

The Coulomb friction coefficient (μ_c) for the sliding tissue alongside the normal force (F_N) and the Coulomb friction force (F_{CO}) exerted on the tissue, can be represented as:

$$F_{CO} = \mu_c \, F_N \tag{B2}$$

From the free body diagram Figure B.2, forces acting in the vertical direction can be described as:

$$\sum Y: F_N - m \, g = 0 \tag{B3}$$

From the same diagram Figure B.2, the forces acting in the horizontal direction can be formulated as:

$$\sum X: F_{CO} + m \, a = F_{Pull} \tag{B4}$$

By integrating the above equations and considering the acceleration (a) to be zero, the resultant equation can be formulated as follows:

$$F_{CO} = F_{Pull} = \mu_c \, F_N = \mu_c \, m \, g \tag{B5}$$

The equation mentioned earlier was used to determine the Coulomb friction coefficients for the coated and the bare plates by using the data gathered by the force sensor. Similarly, the static friction coefficient can also be expressed in the form of the equation.

$$F_S = \mu_s \, m \, g \tag{B6}$$

This experiment was conducted with PVC tissue only because when using biological bovine kidney tissue, the small block created from the biological tissue was uneven and fragile, leading to self-rupturing while sliding. As mentioned in the introduction section, the friction of a surface is primarily influenced by its surface roughness. Therefore, it is essential to examine and study the surface roughness of both the bare and coated needles. In this regard, the surface roughness was measured utilizing an atomic force microscope (AFM). The subsequent section provides a comprehensive explanation of the detailed procedure employed to measure the surface roughness.

The sliding friction test was performed to assess the coefficient of Coulomb friction. The test involved both bare and coated plate samples in evaluating the friction interaction with the sliding tissue. The measurements of the force exerted by the sliding tissue on the two types of plates, bare and coated, are detailed in the following sections. To gain a clearer understanding of the findings, refer to Figure B.3 below, which visually presents the data from the experiment.

The preceding equations (Equations B5 and B6) served as the computational basis for determining the values of both Coulomb and static friction forces that are exhibited when sliding tissue interacts with the bare and coated needle. The outcomes derived from this process have been tabulated below (Table B.1). The average friction coefficients and the standard deviations are shown in Figure B.4.

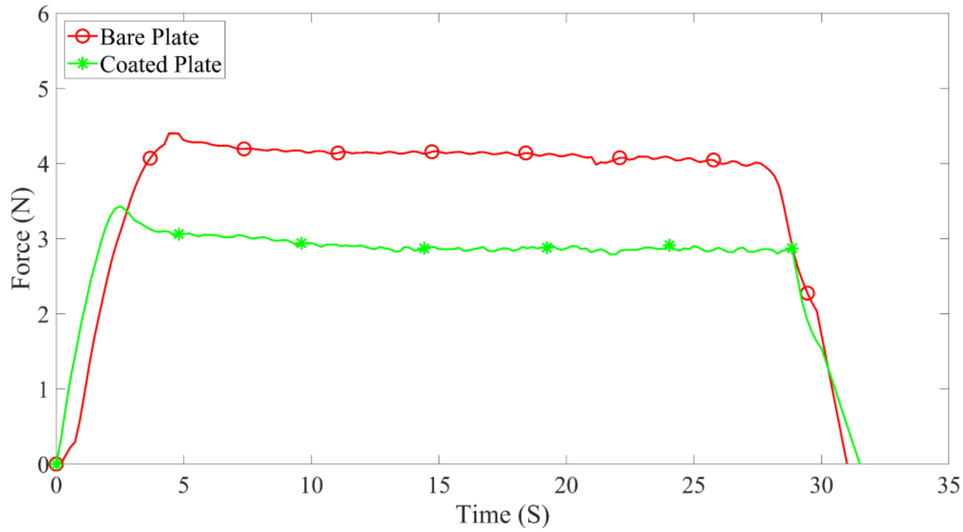

Figure B.3 Force vs. Time graph of forces acting on the sliding tissue on a bare plate and coated. Bare plate standard deviation range 0.29N to 0.45N, and PDA-PTFE-C coated plate standard deviation 0.061N to 0.14 N.

The total mass of the PVC tissue ($5\times5\times2$ cm^3), along with the holder, was 0.7 kg, and it was used to calculate the coefficients of both static and Coulomb friction for the bare and coated plates. The maximum friction force, or static friction, was 4.41 N for the bare plate and 3.4 N for the coated plates. In addition, the Coulomb friction force, which is the average friction after the onset of relative motion between the tissue and the plates, was also measured. The average Coulomb friction force for the bare plate was 4.09 N, and for the coated plate, it was 2.87 N. Using equation B6, the static friction coefficient for the bare plate was found to be 0.79, while for the coated plate, it was 0.50. Additionally, the Coulomb friction coefficient for the bare plate was determined to be 0.60, whereas, for the coated plate, it was 0.42. Therefore, it can be inferred that applying a coating reduced the static friction coefficient by 36%, and the Coulomb friction coefficient was reduced by 30% in PVC gel.

Table B.1 Insertion force parameters for coated and bare plates inside PVC gel tissue

	Bare Plate	**Coated Plate**
Average Static Friction Force	4.3 N	3.4 N
Average Coulomb Friction Force	4.09 N	2.87 N
Static Friction Coefficient	0.79	0.50
Coulomb Friction Coefficient	0.60	0.42

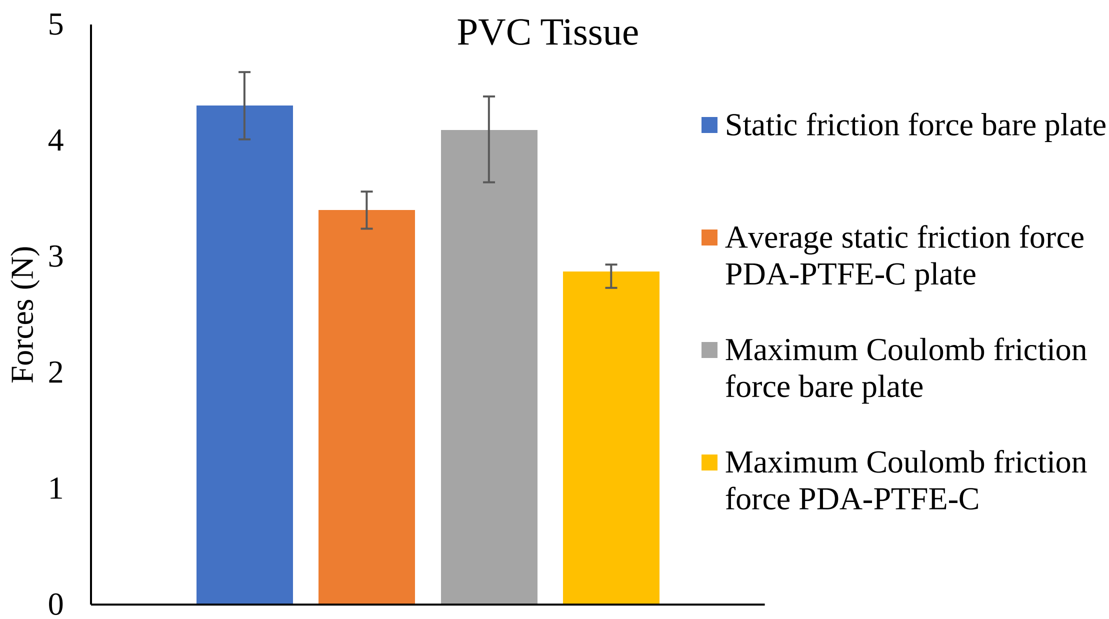

Figure B.4 Average forces and standard deviation for bare and coated plate PVC tissue sliding experiment.

APPENDIX C

MATLAB CODE FOR ANALYTICAL FORCE MODEL

1. Insertion Force Model

```
% F_COP Coefficient of Coulomb friction force

% C_C   Coefficient of Cutting force

% b_vP Coefficient of Viscous force

% k_p   Coefficient of elastic force

% V     Needle insertion velocity

% h     Insertion depth

for i=1:size(h,2)

   F_F=(F_COP + b_vP*V + k_p*V)*h(i) ;

   C_F=C_C*V;

    FF_F(i)=F_F;

    CC_F(i)=C_F;

    II_F (i)= F_F+C_F;

end

hh=linspace(0.010,0.035,100);

figure (1)

plot(hh,FF_F,hh,CC_F,hh,II_F)
```

2. Friction Force Model

```
% Vp         Positive velocity (Insertion)
% Vn         Negative velocity (Extraction)
%  d         Tissue thickness or needle contact length
%  Xp         Positive tissue displacement (Insertion)
%  Xn         Negative tissue displacement (Insertion)
%  Friction  Measured friction forces
%  Variable  Final answer of LSQR
for i=1:253
   if Vel(i)==0
      Vp=0;Vn=0;
   end
    if Vel(i)>0
      Vp=Vel(i);
     Vn=0;
     d=D;
   end
   if Vel(i)<0
      Vp=0;
      Vn=Vel(i);
      d=-D;
   end
```

```
    if Dist(i)==0
        Xp=0;Xn=0;
    end
    if Dist(i)>0
        Xp=Dist(i);
        Xn=0;
    end
    if Dist(i)<0
        Xn=Dist(i);
        Xp=0;
    end
mat=d*[(sign(V)+1)/2  Vp  (sign(V)-1)/2  Vn  Xp  Xn];
Mat(i,:)=mat;
end
for j=1:1000
xx=lsqr (Mat,Friction,10^-10,j);
Variable(j,:)=xx;
End
```

3. Cutting Force Model

```
% F_C Measured cutting force

% C_C Measured cutting coefficient

% V      Needle Insertion Velocity

% Measuring the cutting coefficient

C_C = F_C / V;

% Measuring the cutting force

F_C = C_C * V;
```